A Study Of Semiconductor Quantum Dots In The Application To Terahertz Sensors

RAYMOND DAVIS

M.Sci, AMInstP

Supervisor: Dr Vladimir Antonov

Department of Physics,
Royal Holloway, University of London

May 2011

Declaration of Originality

The work described, undertaken and presented in this thesis as part of the Nanophysics and Nanotechnology group at Royal Holloway, University of London, Physics Department, under the supervision of Dr Vladimir Antonov is entirely my own work, unless otherwise stated and referenced as part of background information used in this project.

Raymond Davis

October 1, 2011

Abstract

This thesis describes the investigation into the fabrication technology and operation of quantum dots (QD) formed in single and double quantum wells in the application to spectral sensitive terahertz sensors. For detection of terahertz radiation we probe charge excitations of QDs caused by the absorption of the terahertz photons by sensitive electrometers, the Point Contact (PC) or the metallic Single Electron Transistor (SET). Single photon sensitivity is achieved using a device with the QD formed in a single quantum well. Devices based on double quantum wells would have advantages in tuning of the resonance spectral line. I report the progress in the development of this sensor. A simplified model of the operation of the QD sensor is discussed.

Acknowledgements

During the course of my PhD, I have been lucky enough to have received invaluable help and support from many people, many of which I need to thank here.

Firstly I must thank my Supervisor Dr Vladimir Antonov for the masses amount of time, support and advice he has given me over the course of my PhD. Vladimir's help, assistance and expertise, were invaluable and essential to the completion of this project.

I would like to thank the number of other researchers I have worked with over the course of my PhD, whose guidance and help has been of great importance to me. In no particular order, these include Dr Rais Shaikhaidarov, Dr Spas Spasov, Dr Michael Exarchos and Dr Mariana Ungureanu. I also appreciate the time and guidance given to me by Dr Phil Meeson and Dr Stewart Boogert who acted as my Advisor and Moderator respectively. I must also acknowledge the great support and help I received from our support technicians, in particular Mass Venti, Ian Murray, Howard Moore, Andy Alway, Leon Ellison and Francis Greenough.

I want to thank my colleagues and friends in the Physics department for there help and support and occasional discussion. In no particular order: David Pavitt, Connor Shelly, Jim Wells, Dr Chris Checkley, Chris Harrison, George Nichols, Kris Kent, Simon Schmidlin, Paco Cordobes and Dan Porter. A special thank you to Richard Marsh for many "interesting and informative" discussions over the years. I also appreciate the funding provided by the EPSRC that enabled me to carry out my research.

Finally I would like to thank my friends and family for invaluable support, especially Dan Cooper, Mark Crouch, James Parry, Andrie Piki, Harry Rowe, Ann Butcher, Lisa Thomas, and Linda Hauptmannova among many others.

An extra special thank you to Tom Dean and Ellie Overthrow-Jones for also giving much of their time to proof read my final thesis on top of their continued support.

Contents

List of Figures

Sample Nanofabrication   **59**

Experimental Techniques   **75**

Appendix   **125**

List of Tables

1 Inception

The detection of terahertz radiation has been used for space observations for many years, such as being used for detecting the composition of stars during their formation.[1] However, the exploitation of terahertz radiation imaging in a more commercial environment has long been overlooked. Terahertz radiation itself is an ideal candidate for security detection and imaging due to its ability to penetrate most common materials, with the notable exceptions of sheet metal and water. The terahertz range from 0.1-10 THz can incorporate detection of many materials including explosive materials and illegal substances. Indeed short wavelength terahertz radiation, towards infrared, has been utilised in imaging equipment using heterodyne systems,[2] however these are not systems that can detect specific chemical signatures, i.e. perform spectroscopy.

Due to the intrinsic property of most common materials to emit terahertz radiation due to molecular vibration and similar processes, it is not unfeasible to recognise the possibility of the passive detection of substances and even imaging.

Currently the majority of passive terahertz detectors are in the form of broad bandwidth superconducting bolometers which, if specific frequency detection is needed, require a series of filters, making it inconvenient for chemical signature detection and also requiring cryogenic cooling to achieve T_c for superconductivity. Bolometers are wide bandwidth detectors as they measure an increase in temperature.[3] Currently superconducting hot electron bolometers have the highest reported sensitivity with a gain bandwidth of 6 GHz,[4] however this is far from single photon detection.[5]

The TeraEye[6] project takes a different route in terahertz detection, namely through the use of a quantum dot (QD) as a sensor for the detection of specific frequencies of terahertz photons. The use of a QD as a terahertz photon detector was first suggested practically in 1998.[7] As many chemical compounds, such as explosive compounds, have specific frequency signatures in the terahertz region, as can be seen in table 1.1 and figure 1.1, a tuneable terahertz detector in the form of a QD would have many applications in security, such as for airport passenger and baggage screening, with the added benefit of being passive. Unlike similar previous detectors, the sensor

being developed here requires no magnetic field.
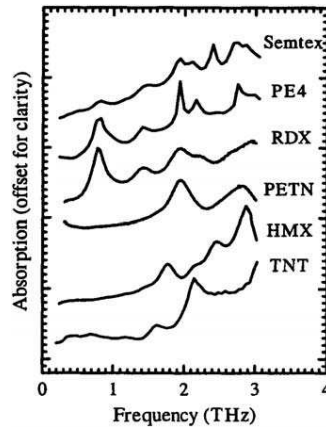
Figure 1.1: Graph illustrating THz signatures of some common explosive materials. [8]

Table 1.1: Absorption peak positions of several common explosives and drugs. Wavenumber conversion: 33.3 cm$^{-1} \approx 1$ THz. [9]

Material	Feature band centre position frequency (THz)
Explosive	
Semtex-H	0.72, 1.29, 1.73, 1.88, 2.15, 2.45, 2.57
PE4	0.72, 1.29, 1.73, 1.94, 2.21, 2.48, 2.69
RDX/C4	0.72, 1.26, 1.73
PETN^a	1.73, 2.51
PETN^b	2.01
HMX^a	1.58, 1.91, 2.21, 2.57
HMX^b	1.84
TNT^a	1.44, 1.91
TNT^b	1.7
TNT	5.6, 8.2, 9.1, 9.9
NH_4NO_3	4, 7
Drugs	
Methamphetamine	1.2, 1.7-1.8
MDMA	1.4, 1.8
Lactose α-monohydrate	0.54, 1.20, 1.38, 1.82, 2.54, 2.87, 3.29
Icing sugar	1.44, 1.61, 1.82, 2.24, 2.57, 2.84, 3.44
Co-codamol	1.85, 2.09, 2.93
Aspirin, soluble	1.38, 3.26
Aspirin, tablets	1.4, 2.24
Acetaminophen	6.5
Terfenadine	3.2
Naproxen sodium	5.2, 6.5

^{a}Samples formed as pellets using spectrographic-grade polyethylene.
^{b}Samples in the form of compressed pellets. All materials are water free.

This project utilises QDs as terahertz detectors at a temperature range of 0.3 K to 4.2 K depending on which read-out method is being used. As the QD absorbs a photon it causes an electron to be excited out of the QD. This change in charge is then detected by one of two possible read-out methods: Point Contact (PC) readout and Single Electron Transistor (SET) readout. With the development of cryogen-free

coolers,[10] the commercial possibility of QD tuneable terahertz detector is more than viable. As part of the TeraEye project this thesis will discuss the fabrication, testing and analysis of such terahertz detectors and further potential developments.

The first part of the project consists of fabricating QDs coupled to PCs and SETs. PCs have relatively lax fabrication demands compared to the demands of SET fabrication. Such fabrication utilises shadow evaporation techniques and highly precise alignment. The QD is formed on a mesa, which is defined in the focal point of a planar metallic antenna with a 1.5 mm span, designed to operate at a frequency range of 0.2-2 THz. The mesa itself is formed from an acid-etched two dimensional electron gas (2DEG) hetrostructure. A discussion regarding fabrication can be found in section three.

The second part involves the low temperature measurements and analysis of the QD-SET and QD-PC sensors. Different hetrostructures, with different 2DEGs composed of GaAs/AlGaAs, have different electron mobilities and effective electron/hole masses depending on the material and lattice structure, as defined by the growth of the material. It was shown that the sensors with PCs are potentially the more realistic option for commercial use than those with SETs. Further discussion regarding testing and analysis can be found in sections five and six.

The final part is to build upon the above two sections by developing similar sensor systems, but using stacked coupled QDs, formed from a bilayer 2DEG hetrostructure. It is from this that more sensitive and potentially more "tuneable" sensors can be formed.

2 Literature Review

2.1 Existing Methods of Terahertz Radiation Detection

As previously described there are currently many different methods of THz radiation detection. The low temperature detectors which are particularly exploited in the space research community are semiconductor bolometers, superconducting bolometers and heterodyne mixers. One should mention also thermopile[11] and the pyroelectric detector,[12] which have since been superseded due to their low sensitivity. For spectral analysis a THz time domain spectroscopy systems are used. Recently the QD detectors emerged, which allows a spectral detection of THz radiation with single photon sensitivity.[13]

2.1.1 Bolometers

The main forerunner of terahertz detection technology, which currently are widely used are the bolometers. Bolometers measure the energy of incident electromagnetic radiation. They operate as thermal detectors, where part of the bolometer, the absorber, changes in temperature due to the incident radiation. This temperature change is then detected by a sensor, such as an electrical resistance thermometer.[14] Current bolometers can be divided into two groups of superconducting bolometer and semiconductor bolometer. Recently there have been developments in cold and hot electron micro-bolometers.[15, 16, 17]

In superconducting bolometers a thin film of superconductor material is deposited on a substrate such as sapphire. The operation is based on the principle of the superconducting transition edge,[18] where the device operates due to the resistance of the superconductor being a sensitive function of the temperature. This is achieved by biasing the device close to the point of the superconducting transition. The low impedance of such a device makes the device operation complicated, requiring the device to be operated in an AC bridge with lock-in detection. The device also requires a feedback setup connected to a heating device connected to the sample/sample holder. This setup can achieve a noise equivalent power (NEP) of $\backsim 10^{-15} \frac{W}{\sqrt{Hz}}$ at $1.27K$. The device has applications mainly in space research, but due

to its complexity is rarely used in widespread application. Further improvements on such a device have been done. Adding an antenna to the microbolometer[19] causes the coupling between the incident radiation and the sensor to increase and therefore extend the operational frequency range. With these differences an NEP$\backsim 10^{-14} \frac{W}{\sqrt{Hz}}$ has been achieved but at an increased operational temperature of 4.2K, however it was noted that with an improvement in the read out noise, the NEP could be further brought down to NEP$\backsim 10^{-15} \frac{W}{\sqrt{Hz}}$ at 4.2K.[19]

Current transition edge bolometers stay at the transition point using electrothermal feedback and also are voltage biased to improve performance. These two modifications have shown, along with the use of a SQUID amplifier, that it is possible to achieve an NEP$\backsim 3.3 \times 10^{-17} \frac{W}{\sqrt{Hz}}$.[20]

Kinetic inductance variance of a device can also be used as a transition edge bolometer, where the kinetic inductance variance is a function of temperature. In superconductors a higher temperature results in more quasiparticle excitations, meaning an acceleration of the Cooper pairs. This leads to a relation of the inductance being proportional to the square of the temperature dependent penetration depth. Theoretically NEP$\backsim 4 \times 10^{-17} \frac{W}{\sqrt{Hz}}$ can be achieved,[21] however, only an NEP$\backsim 10^{-11} \frac{W}{\sqrt{Hz}}$ was reported.[22]

Conventional bolometers use superconducting material where the electrons and phonons are in equilibrium. However, in a system where this is not true, a Hot-electron photodetector/bolometer (HEP/HEB) can be formed.[23] This is achieved by making the phonon-electron energy relaxation time large due to the design of the detector. As electronic excitations have very short relaxation times this makes HEPs very fast and sensitive detectors compared to standard bolometers.

Transition edge HEPs based on a thin film of niobium can achieve a response time of 4.5 ns and an NEP of $\backsim 3 \times 10^{-13} \frac{W}{\sqrt{Hz}}$, making them less sensitive compared to semiconductor bolometers but with a much lower response time and display a constant sensitivity from the microwave range to the ultraviolet range.[24] In more recent developments a decreased resonance time of 30ps with an NEP of $\backsim 10^{-12} \frac{W}{\sqrt{Hz}}$ was achieved when using ultra thin NbN films.[25]

Photon induced hot spot detectors have displayed detection of 0.8μm photons

at rates of 10 GHz with a quantum efficiency of approximately 0.2 and dark count (intrinsic) of $0.001s^{-1}$, leading to an infrared region NEP of $\backsim 5.5 \times 10^{-20} \frac{W}{\sqrt{Hz}}$. In these detectors the absorption of single photons causes a hot spot in a superconducting bridge which is kept below the critical temperature. With the device biased, the hot spot caused by the single electron causes the critical current to be exceeded in lateral regions to the hot spot, causing a non superconducting barrier to be formed. This causes a voltage spike or pulse across the device, which can then be detected. The hot spot then cools due to electrons diffusing out of the hot spot and then scattering with phonons, so the device is ready to detect a photon again. The switching time between a detected state and a non detected state is of the order of 30ps.[26] It does seem however that the range of sensitivity can not be expanded out of the infrared region. This is due to the operating conditions of such a device, which is $v \gg \frac{2\Delta}{h} \backsim 1THz$ where v is the operating frequency and Δ is the superconducting band gap.

Superconducting-insulator-normal (SIN) junctions can also be utilised as bolometers by utilising the normal metal part as an absorber. NEPs of $\backsim 3 \times 10^{-18} \frac{W}{\sqrt{Hz}}$ have been shown.[27] Andreev reflections of electrons at the normal-superconducting barrier traps energy in the normal metal, and with the weak phonon-electron coupling at operational temperatures of approximately 100mK, a large temperature change is detectable in the absorber. This temperature change manifests itself as a changed I-V characteristic of the junction.

As the SIN junction could also cool the electrons in the normal metal it has led to the development of cold electron bolometers with potential NEPs of $10^{-19} \frac{W}{\sqrt{Hz}}$.[17]

One of the highest sensitivity detectors are semiconductor bolometers, used for processes such as Fourier transform spectroscopy, as well as astronomy techniques.[28] Heavily doped germanium and silicon are widely used to form semiconductor bolometers. Conduction is found to be propagated by variable range hopping.[29] This is due to the materials being doped close to the metal-insulator transition point. This then gives a resistance to temperature relation of $Log(R) \backsim \frac{1}{\sqrt{T}}$. Semiconductor materials are used for both the thermometry part and the absorption part in microchip bolometers, but due to this the absorption of wavelengths towards the microwave region begins to reduce, forcing the use of the larger microchips to in-

crease the desirable detectable bandwidth. One way around this is to use different compounds for the substrate, absorber and thermometer parts, such as using a germanium thermometer, sapphire substrate and a bismuth film absorber, or a diamond substrate with a nichrome thin film absorber. The best bolometers achieve NEPs of $\backsim 2.5 \times 10^{-17} \frac{W}{\sqrt{Hz}}$ at 0.1K compared to a room temperature NEP $\backsim 3 \times 10^{-10} \frac{W}{\sqrt{Hz}}$.

2.1.2 Time-Domain Spectroscopy

Terahertz Time-Domain spectroscopy (TDS) is a broadband spectroscopic technique with a typical frequency bandwidth of 500Ghz centred on 1-2 THz. It is an active technique, meaning THz radiation is radiated onto the sample. It is non contacting method. Information from reflected or transmitted radiation is be collected for analysis. Unlike regular Fourier transform spectroscopy, which is sensitive to only amplitude, time-domain spectroscopy is sensitive to both amplitude and phase.

TDS has several advantages including non contact spectroscopy as already mentioned, large spectral bandwidth in the THz region and coherent measurements which allows both real and optical components of a signal to be measured, such as the index of refraction and the dielectric constant. The large spectral bandwidth allows many frequency signatures to be detected, where other system, such as bolometers which require a series of filters to isolate a frequency, may be limited to a much smaller range. Due to the large bandwidth of the TDS technique, this results in a small coherence length, giving a large spatial resolution.

However, TDS is limited by a few factors, such as the pulse laser required is still a specialist and costly piece of equipment and are often low powered. Samples also need to be in situ and require active THz radiation to be incident on the sample, unlike the passive QD terahertz detector.

An example of a TDS system is shown in figure 2.1. The emitter consists of a single semiconductor crystal which has had a two part antenna fabricated onto it. The antenna then has a large electric field put across it by applying a potential to opposing sides of the antenna. Infrared laser pulses of approximately 10-200fs are directed into the centre of the antenna onto the crystal causing electron hole pairs to be formed, which are then accelerated due to the applied electric field. The changing in dipole moment causes a spread of THz frequencies to be produced, which can then be focused and scanned along the sample.[30] Many different types of semiconductor and crystals can be used to produce the THz pulse, the most used being ZnTe.[31] Using different setups one can produce different THz pulses, covering a range of 0.05-4 THz.[32]

8

The principle piece of equipment in the TDS system is the laser. For TDS to be of significant sensitivity, at least a femtosecond pulse laser needs to be used. The laser produces the required pulse train, with the pulses repeating in the order of 100MHz and the pulse lengths being 100fs or less. The emitted pulse train is then split into two separate beams, with one used to gate the detector and the other used to generate the THz signal. Using this approach, the radiation is coherent so $E(t)$ can be measured directly, so both amplitude and phase information are measured.
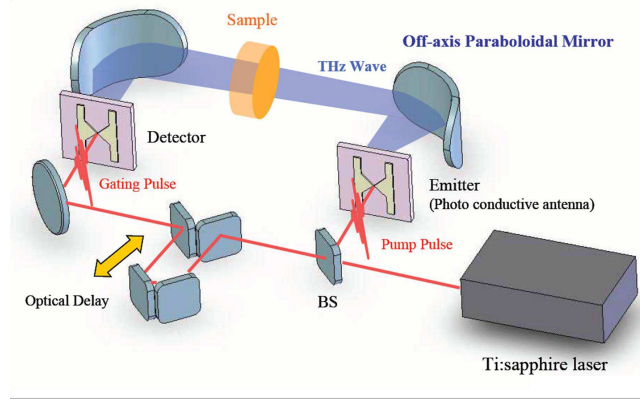
Figure 2.1: Schematic illustration of the equipment setup for a TDS system.[33]

A delay line on the transmitter side is used to vary the time at which the THz signal reaches the sample to be probed. It is assumed that the pulses are identical, this allows several measurements to be taken at different delay times, so a picture can be built up of the electric field interacting with and without the sample as a function of time, allowing a time dependent electric field trace to be built up, as shown in figure 2.2. This is further improved by taking multiple measurements at each given delay time as to improve the signal-to-noise ratio.[34]

On the right in figure 2.2, we can see the Fourier transform spectrum of the initial time domain measurement. This technique will only be valid however if the pulse train is not generated on a time scale similar to that of the measurement. This leads to TDS measurements requiring a large number of data points. The minimum acquisition time, t_{min} for such measurements can be calculated using

$$t_{min} = N \times \Delta t \qquad (2.1)$$

where Δt is the time spacing between pulses and N is the total number of electric

field measurements performed on the sample.
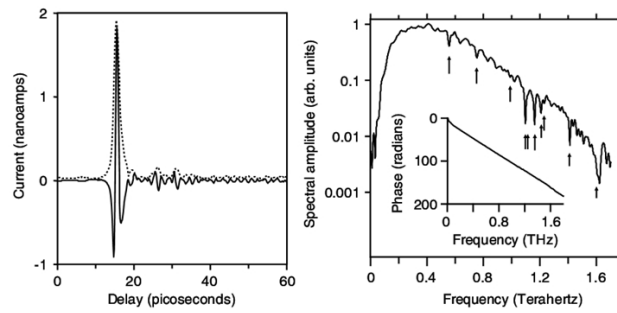
Figure 2.2: The left figure shows a THz time-domain measurement of air. The dotted line indicates the intensity envelope. Right image shows the subsequent FT spectrum, with arrows indicating the absorption lines found in water. The relative phase of the signal can be seen in the inset as a function of frequency. [34]

2.1.3 Heterodyning

Heterodyning is the technique of mixing two closely spaced frequencies to produce two further signals which are the sum and difference of the original signals. It is a well established technique having been used for over 80 years. The concept of its use, is to down shift the frequency of interest to a frequency that is much easier to detect, which why it is an appropriate technique for THz detection. If one of the first signals is known then the second may be identified. The basic principle of heterodyning is based on the following trigonometric identity

$$\sin\theta\sin\varphi = \frac{1}{2}\cos(\theta-\varphi) - \frac{1}{2}\cos(\theta+\varphi) \tag{2.2}$$

This identify can then be used to mix two sine wave signals $\sin(2\pi f_1 t)$ and $\sin(2\pi f_2 t)$ to produce the following

$$\sin(2\pi f_1 t)\sin(2\pi f_2 t) = \frac{1}{2}\cos[2\pi(f_1-f_2)t] - \frac{1}{2}\cos[2\pi(f_1+f_2)t] \tag{2.3}$$

Heterodyning has the advantage of being able to detect very weak narrow band signals, where direct detection and amplification or pre amplification followed by detection would add too much electronic noise. This would cause the signal to become lost unless unacceptably long integration times are used. As the integration time required to isolate a given frequency increases as the square of the equivalent system noise, it would require that all sources of electronic noise are minimised. Currently direct electronic amplification of signals above 150GHz is difficult to im-possible,[35] so currently heterodyning is favoured for this regime. The mixing is accomplished by using a non-linear rectifying element, such as a diode, fast bolome-ter, tunnel junction or even a superconducting tunnel junction.

Signals of interest are typically mixed with a local signal produced by an oscillator at a closely spaced frequency. By down shifting the signal with a heterodyning mixer, the signal can be easily amplified and detected with minimal additional noise. This allows the signal to be easily filtered if required or even down shifted a second or possibly a third time, ready for easy detection. The bandwidth and quality of the

down mixed signal is highly dependent on reference signal provided for mixing. High quality sources, such as a quantum cascade laser often phase locked via a harmonic mixer are usually used. Assuming a narrow bandwidth reference signal and the output signal is filtered, then thermal noise and undesired signals can be avoided in the detection part of the system. Signal bandwidth filtering is regularly used so that the total RF bandwidth is only a few hundred kHz, which when working in the THz spectrum means the bandwidth becomes one part in 10^7. This can give very high signal to noise ratios of 100dB or more, making heterodyning systems very favoured for detection of low power astronomical signals. However for broader bandwidth detection, continuous spectroscopy or imaging, direct detection, such as with semiconductor sensors, is preferred, although these often need cryogenic cooling to reduce noise. Heterodyning imaging systems have now been developed. However these systems often require active illumination of the target object.[36,37,38] Room temperature heterodyning systems based on mixing components such as Schottky diodes have the further advantage having a very wide range of signal power detection sensitivity, ranging from picowatts to tens milliwatts, a dynamic range of 10^{10}, with the detected current/voltage remaining linear throughout the detector.

As THz radiation is so heavily absorbed by the surrounding environment, a large range makes calibration simpler. Particularly in imaging applications, the large range proves advantageous when imaging objects that have a very large differential contrast. Utilising the heterodyning technique, magnitude and phase information is also preserved and it lends itself nicely to spectroscopy due to the system being immune from other signals outside of the designated bandwidth.

Heterodyning techniques, utilising silicon field effect transistors have been reported to achieve an NEP of $300\frac{pW}{\sqrt{Hz}}$[36] at 0.65THz for imaging. NEPs as low as $4\frac{pW}{\sqrt{Hz}}$ at 639GHz have also been reported for Schottky diodes.[39] Terahertz radar has recently come to commercial fruition with the instillation and use of Terahertz radar body scanners at airports for security, such as systems developed by ThruVision and spectroscopy and imaging systems for science, as developed by companies such as TeraView.

2.2 A Quantum Dot Terahertz Detector

The sensors being developed as part of this project operate by forming a QD from a 2DEG formed within a GaAs/AlGaAs heterostructure. The QD is charge excited by absorption of THz photons. The excitation is then read out either by Point Contact (PC) or Single Electron Transistor (SET). The description of how they are made can be found in section 3 and their operation in section 5. These sensors draw on many aspects of nanophysics, including quantum well formation in heterostructures, SET theory and single electronics in OD systems as well as THz optics.

2.2.1 Single Electron Transistors (SET)

This section will introduce the fundamentals of single electronics and the associated theory and will briefly touch on second-order effects. These will lead specifically to the single electronics as is used in the electron transport in PCs, SETs and will eventually lead onto to electron transport in QDs. The specifics of electron transport in QDs are outlined in section 2.2.3.

2.2.1.1 Orthodox Single Electron Theory

The following section will describe Orthodox Electron Theory from the thermo-dynamical, Gibbs free energy treatment per tunnel event. A electrostatic energy treatment, producing the same conclusions, but specific to QDs will be presented in section 2.2.3.

We may consider a closed system consisting of only capacitors, tunnel junctions and voltage sources, where the total amount of internal energy, $E_{internal}$, is conserved. When a tunnelling event occurs, any decrease in electrostatic energy, U, must therefore be due to thermal energy, $Q_{thermal}$ such that

$$E_{internal} = U + Q_{thermal} \tag{2.4}$$

Within this closed system the extensive variables, which scale with the size of the system are the entropy, S, and node the charges of the capacitors and tunnel junctions, such that the total differential of the internal energy can be considered

$$dE_{internal} = \sum_{i=1}^{N} \frac{\partial E_{internal}}{\partial q_i} dq_i + \frac{\partial E_{internal}}{\partial S} dS \tag{2.5}$$

Using standard thermodynamic considerations, the temperature can then be defined as the partial derivative of $E_{internal}$

$$T = \frac{\partial E_{internal}}{\partial S} \tag{2.6}$$

Similarly the node voltage at a given node may be defined as

$$v_i = \frac{\partial E_{internal}}{\partial q_i} = \frac{\partial U}{\partial q_i} \tag{2.7}$$

We may now construct the differential total internal energy as

$$\begin{aligned} dE_{internal} &= \sum_{i=1}^{N} v_i dq_i + TdS \\ &= \mathbf{v}^T d\mathbf{q} + TdS \end{aligned} \tag{2.8}$$

We may also construct the Helmholtz free energy as we have already stated that during a tunnel event the internal energy is conserved, therefore making $dE_{internal} = 0$ and we may assume the event to be carried out at a constant temperature so $dT = 0$ also. Therefore we can state

$$F_H = E_{internal} - TS \tag{2.9}$$

and

$$\begin{aligned} dF_H &= dE_{internal} - TdS - SdT \\ &= 0 + \mathbf{v}^T d\mathbf{q} - SdT \end{aligned} \tag{2.10}$$

We can see that as long as the temperature remains constant, any changes in the Helmholtz free energy will be equal to the changes in the electrostatic energy of the system

$$\Delta F_H = \Delta U = \int \mathbf{v}^T d\mathbf{q} \tag{2.11}$$

This has taken into account the charge sources. When taking into account the voltage sources also, we may use the Gibbs free energy, such that

$$
\begin{aligned}
F &= F_H - \mathbf{v_v}^T q_\mathbf{v} \\
&= U + Q_{thermal} - TS - W
\end{aligned}
\tag{2.12}
$$

We define W as the work done by all voltage sources, and can be expressed as the total power integrated over time, where $V(t) and I(t)$ are the voltage and current of each respective source

$$
W = \sum_{sources} \int V(t)I(t)dt
\tag{2.13}
$$

We may also conclude that the total differential Gibbs free energy is

$$
dF = dU - SdT - dW
\tag{2.14}
$$

and at constant temperature, this becomes

$$
dF = dU - dW
\tag{2.15}
$$

So we can see that at constant temperature, the change in energy due to an electron tunnelling across a junction is only dependent on the voltages of the sources that the electron is tunnelling to and from, which can be said to be the energy required to tunnel from state i to the final state f. This idea is replicated in the electrostatic consideration of such a system.

As we have now calculated the energy required to tunnel from state i to state f and that it is proportional to the voltage difference between the states, we may now calculate the transmission rate or tunnel rate between said states. First we define the change in free energy as the difference between the free energy before the electron tunnels and after it has tunnelled. So it can be seen that a transition from one state to another state with lower energy will give a negative free energy change

$$
\Delta F = F_f - F_i
\tag{2.16}
$$

Using Fermi's golden rule and knowing the change in free energy, the tunnel rate may be expressed as

$$\Gamma(\Delta F) = \frac{2\pi}{\hbar}|T_{if}|^2\delta(E_i - E_f - \Delta F) \tag{2.17}$$

where $|T_{if}|$ is the transmission coefficient from state i with momentum k_i to state f with momentum k_f for a given tunnel event. We may now sum over all k states to calculate the total rate from occupied to non occupied states. To do this we must know the probability of unoccupied/empty states which an electron may tunnel too. We do this using the Fermi-Dirac distribution $f(E)$, which describes the probability of finding an occupied state at a given energy level. Therefore the probability of an empty state is $1 - f(E)$.

$$f(E) = \frac{1}{1 + e^{(E-Ef)/(k_bT)}} \tag{2.18}$$

So we may use

$$\begin{aligned} 1 - f(E) &= f(-E) \\ &= \frac{1}{1 + e^{(-E+Ef)/(k_bT)}} \end{aligned} \tag{2.19}$$

We may also approximate that the variation in the tunnel transmission coefficients are negligeable, and consider it instead to be a constant. With these considerations we may now rewrite equation 2.17 as

$$\Gamma(\Delta F) = \frac{2\pi}{\hbar}|T|^2 \sum_i \sum_f f(E_i)(1 - f(E_f))\delta(E_i - E_f - \Delta F) \tag{2.20}$$

We can replace the sums over momentum to integrals over energy by knowing the number of electron states in a small energy interval of dE and using the density of states $D(E)$, integrating between conduction band and infinity of the initial state side, $E_{c,i}$ and between the conduction band and infinity of the final state side $E_{c,f}$

$$\Gamma(\Delta F) = \frac{2\pi}{\hbar}|T|^2 \int_{E_{c,i}}^{\infty} dE_i \int_{E_{c,f}}^{\infty} dE_f D_i(E_i)D_f(E_f)f(E_i)(1 - f(E_f))\delta(E_i - E_f - \Delta F) \quad (2.21)$$

It can be seen that the product of the two fermi distributions at lower temperatures will form a rectangular window containing the states centered around -0.5eV with a width of approximately $-1eV = E_{F_f} - E_{F_i} = \Delta F$. As this window is where the main contribution of the rate comes from, we can approximate that the density of states to be constant and using the delta function, we may remove one of the integrals, leaving us

$$\Gamma(\Delta F) = \frac{2\pi}{\hbar}|T|^2 D_i D_f \int_{E_c}^{\infty} f(E)(1 - f(E - \Delta F))dE \quad (2.22)$$

where E_C is the higher of the two conduction bands. We may now use the concept of tunnel resistance, because tunnel junctions are essentially ohmic conductors still. Tunnel resistance is defined as

$$R_T = \frac{\hbar}{2\pi|T|^2 D_i D_f} \quad (2.23)$$

This now allows us to simplify further to give

$$\Gamma(\Delta F) = \frac{1}{R_t e^2} \int_{E_c}^{\infty} f(E)(1 - f(E - \Delta F))dE \quad (2.24)$$

We can make the further assumption that the Fermi level will be within the conduction band, this allows us to change the limits of integration to E_c to $-\infty$. This allows us to solve the above rate equation, giving

$$\Gamma(\Delta F) = \frac{\Delta F}{e^2 R_T(e^{\Delta F/(k_B T)}T - 1)} \quad (2.25)$$

which can be seen to have the following solutions at zero temperature

$$\Gamma(\Delta F) = \begin{cases} 0 & \Delta F \geq 0 \\ \frac{-\Delta F}{e^2 R_T} & \Delta F < 0 \end{cases} \quad (2.26)$$

17

So as can be seen and would be expected, transport only occurs when the change in free energy is negative, or as was earlier stated, the starting energy state is higher than that of the finishing state. This will be shown for the electrostatic case also. The model has made a number of assumptions however. These include the energy spacing between levels is smaller than that of the thermal energy, therefore making the energy spectrum essentially continuous. It also assumes that the time for an electron to tunnel is essentially instantaneous, or at least much smaller than the time between each tunnel event.

It is also assumed that the electron states on the island are localised and well defined, i.e. an electron is either on the island or it is not. This is only achieved by the resistance of the tunnel junction being sufficiently high enough as to isolate the electrons from the surrounding environment. Taking into account qualitative quantum mechanical arguments we can calculate this minimum resistance required. If we describe the number of electrons, N, in the system as being an average number, $\langle N \rangle$, then coulomb blockade will require the following condition to be satisfied.

$$|N - \langle N \rangle|^2 \ll 1 \tag{2.27}$$

To therefore calculate the minimum value of resistance which the barriers would need to be we first consider the energy uncertainty of an electron and the characteristic charge time fluctuation of a capacitor

$$\Delta E \Delta t > h \tag{2.28}$$

$$\Delta t \simeq R_T C \tag{2.29}$$

where C is the capacitance and R_T the resistance of the tunnel junction. Taking the energy gap associated with a single electron as

$$\Delta E = \frac{e^2}{C} \tag{2.30}$$

and combining this with equation 2.28 and 2.29, we may write

$$R_T > \frac{h}{e^2} = 25813\Omega \tag{2.31}$$

This therefore defines the minimum resistance that tunnel junctions need to be to follow the principles of single electron charging.

2.2.1.2 Coulomb Blockade

As is discussed in section 2.2.3, coulomb blockade occurs when the energy level of the tunnel barrier is greater than that of starting and finishing energy levels.

The free energy change of a junction with charge Q, only taking into account electrostatic energy, when a tunnelling event occurs where the charge will change by $\pm e$

$$\Delta F = \frac{(Q \pm e)^2}{2C} - \frac{Q^2}{2C} = \frac{e^2}{2C}\left(1 \pm \frac{2Q}{e}\right) \tag{2.32}$$

We can see therefore that as the charge reaches $\frac{e}{2}$ the change in free energy becomes less than zero, and therefore it becomes energetically favourable for the electron to tunnel as can be seen in figure 2.3.
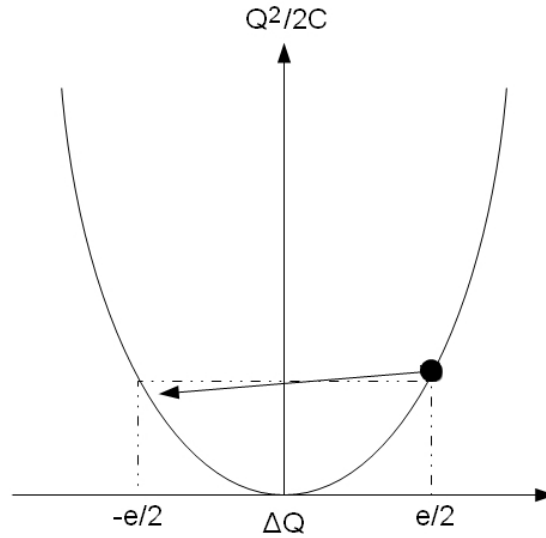
Figure 2.3: Change in free energy due to energetically favourable tunnelling of an electron once the island charge, Q, exceeds $e/2$.

We can therefore see that the system continually charges the system at a constant rate of $Idt = dQ$ until the junction charge reaches $\frac{e}{2}$, at which point the electron will tunnel and the junction charge will return to $\frac{-e}{2}$ and the charging will continue again. This must mean there is a periodic rate, as can be seen in figure 2.4, at which the electrons tunnel, which will be equal to

$$f_{SET} = \frac{I}{e} \tag{2.33}$$
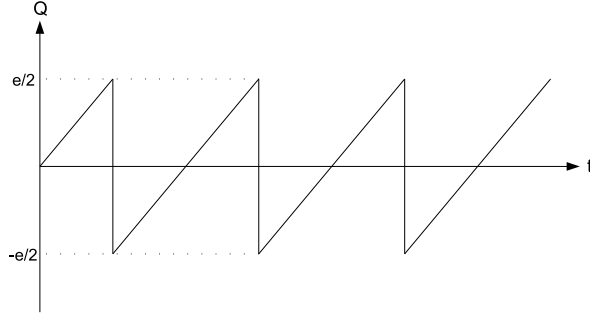
Figure 2.4: Periodic charge oscillations due to energetically favourable tunnelling events.

When two junctions are in series, a tunnel event in the first one may affect the outcome of a tunnel event in the second. The potential of an uncharged island where the first junction has a capacitance of C_1 and at potential V_b and the second junction has a capacitance of C_2 and is grounded is V_b, so the potential of the island is

$$V_{island} = \frac{V_b C_1}{C_1 + C_2} \tag{2.34}$$

As V_b is increased, the Coulomb blockade will be overcome to allow a tunnelling event causing the potential off the island to increase by $e/(C_1 + C_2)$. This increase may then be enough to overcome the potential of the second junction allowing a second tunnelling event to occur, and as the second tunnel event will decrease the potential on the island, it may allow a tunnel even in the first junction to occur. This is a demonstration of space corelated tunnelling.

2.2.1.3   Superconducting Tunnel Junctions

One of the fundamental differences between the superconducting and non supercon-
ducting tunnel junctions is the difference in the formulation of the density of states.
Unlike the density of states in a normal material as discussed in sections 2.2.2 and
2.2.3. As the density of states is part of the tunnel rate equation, it therefore directly
effects the system. Unlike normal materials, the density of sates cannot be consid-
ered constant, as for materials such as semiconductors and superconductors, as seen
in figure 2.5 where the density of states can be zero, the correct energy dependence
of density of states needs to be accounted for.
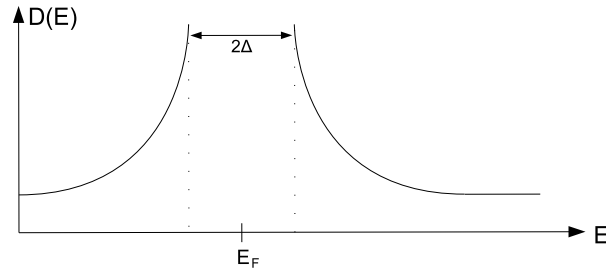
Figure 2.5: Density of states for superconductors illustrating the band gap which is of the
order 1 meV.

This density of states for the superconductor, where D_0 is the DOS a the Fermi level,
can be described as

$$D_{super}(E) = \begin{cases} D_0 \dfrac{|E-E_F|}{((E-E_F)^2 - \Delta^2)^{\frac{1}{2}}} & |E - E_F| > \Delta \\ 0 & |E - E_F| \leq \Delta \end{cases} \tag{2.35}$$

Quasiparticle tunnelling may also occur in superconducting junctions. This is where
individual electrons tunnel across the barrier opposed to the standard cooper pair
in a superconductor, due to it being favourable in terms of energy states. Although
quasiparticles are individual electrons, they still follow the density of states of cooper
paris, as given in equation 2.35. Orthodox theory still applies, however this density
of states must be substituted instead.

2.2.1.3.1   Coherent and Incoherent Cooper Pair Tunnelling

Coherent tunnel is free of dissipation and the electrode coupling can be described using the Josephson energy, $\frac{-E_J}{2}$. We may define the Josephson energy using the critical current I_c, as

$$E_J = \frac{h}{R_T \Delta 2e^2} = \frac{\hbar I_c}{2e} \tag{2.36}$$

As the process is coherent, we must take into account that there may be many different possible tunnel events that could lead to a given charge configuration amongst the electrodes and islands. Given a reference state, we therefore need to uniquely identify how much charge has been transferred for any given possible transition, which we denote as $\bar{Q}$. A Hamiltonian for such a system can then be devised [40], denoting a unique charge state as $|\bar{Q}\rangle$

$$H_0 = \sum_{|\bar{Q}\rangle} \left(F_{\bar{Q}} |\bar{Q}\rangle\langle\bar{Q}| - \frac{E_J}{2} \sum_{\pm 2e} |\bar{Q} \pm 2e\rangle\langle\bar{Q}| \right) \tag{2.37}$$

where $|\bar{Q}\rangle$ denotes all relevant charge states and where $|\bar{Q} \pm 2e\rangle$ denotes all of such states that can be reached by Cooper pairs. If there are more states than there are states that Cooper pairs may reach, i.e. states that differ by $\pm e$ rather than $\pm 2e$, then the remaining states may only be reached by quasiparticles.

As to include quasiparticle transport in the system described in the Hamiltonian 2.37, we use first order perturbation theory to perturb the Hamiltonian, $H = H_0 + H_T$. Using this perturbation and by diagonalising the Hamiltonian, it can be shown that without current dissipation, a DC voltage will produce an AC supercurrent. However, if there is some form of current dissipation, such as quasi particle tunnelling, then a DC current may flow, therefore causing transitions between different eigenstates. By combing the perturbed and non perturbed systems of quasiparticle tunnelling. It can be shown that the rate at which tunnelling between states due to quasiparticles is [41]

$$\Gamma_{i \to f} = \frac{1}{e} \frac{I(\Delta F_{if})}{e^{\Delta F_{if}/k_B T} - 1} \left| \sum_{\bar{Q}} \langle\Psi_f|\bar{Q} \pm e\rangle\langle\bar{Q}|\Psi_i\rangle \right|^2 \tag{2.38}$$

where ΔF_{if} is the change in free energy due to a quasiparticle tunnel event from states $i \rightarrow f$.

Alternatively, if the phase coherence between the two electrons that make up a Cooper pair becomes destroyed, due to an external EM field for example, then it can be shown that the tunnel rate is [42]

$$\Gamma_{incoherent} = \frac{\pi}{2\hbar} E_J^2 P_{2e}(\Delta F_{2e}) \tag{2.39}$$

where P_{2e} is the probability that an electron will exchange energy with its environment and ΔF_{2e} is the change ion free energy for transferring two electrons.

2.2.1.3.2 Superconducting Single Electron Transistors (SETs)

The most utilised outcome of single electron theory is the Single Electron Transistor (SET), first fabricated and investigated in 1987.[43,44] There are three types of SET, defined by how the gate is coupled to the central island. These are the Resistive-SET (R-SET), Resistive and Capacitive-SET (RC-SET) and the Capacitive-SET (C-SET). This project utilises exclusively the C-SET and as such will provide information on the C-SET and not the other two. The C-SET configuration can be seen in figure 2.6. The bias across the junctions between the central island, V_0 can be defined as
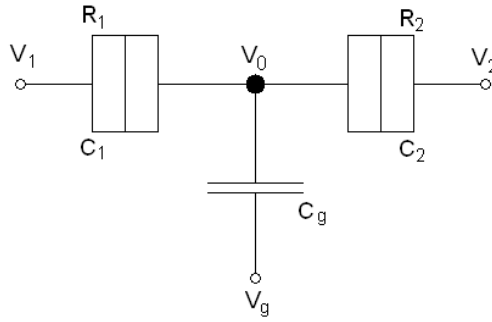
Figure 2.6: Circuit illustration of a C-SET.

$$V_1 - V_0 = \frac{V_1(C_2 + C_g) - V_2 C_2 - V_g C_g + ne - q_0}{C_1 + C_2 + C_g} \tag{2.40}$$

$$V_0 - V_2 = \frac{V_1 C_1 - V_2(C_1 + C_g) + V_g C_g - ne + q_0}{C_1 + C_2 + C_g} \tag{2.41}$$

where q_0 is the existing (if any) noninteger offset charge and n the number of excess electrons on the island. This allows to calculate the change in free energy when tunnelling events occur left to right (+) and right to left (-) in each junction. For the first junction the change in free energy can be

$$\Delta F^+ = e\left(\frac{e}{2(C_1 + C_2 + C_g)} + (V_1 - V_0)\right) \tag{2.42}$$

$$\Delta F^- = e\left(\frac{e}{2(C_1 + C_2 + C_g)} - (V_1 - V_0)\right) \tag{2.43}$$

and similarly for the second junction, the change in free energy can be

$$\Delta F^+ = e \left(\frac{e}{2(C_1 + C_2 + C_g)} + (V_0 - V_2) \right) \qquad (2.44)$$

$$\Delta F^- = e \left(\frac{e}{2(C_1 + C_2 + C_g)} - (V_0 - V_2) \right) \qquad (2.45)$$

By assuming operation at 0K, where a free energy change can only be negative, we can set the above equations to zero and device 4 linear conditions. These conditions when plotted give the stability domains for where an SET may operate. As can be seen from the equations, the structure of these boundaries are dependent on many things including biasing, capacitances and existing charges, are variables that can be dependable on the fabrication of the SET. The equations we obtain by carrying this out for each junction (1 and 2) are

$$1^+ \qquad -e(n + \tfrac{1}{2}) + q_0 = (V_1 - V_g)C_g + (V_1 - V_2)C_2 \qquad (2.46)$$

$$1^- \qquad e(n - \tfrac{1}{2}) - q_0 = (V_g - V_1)C_g + (V_2 - V_1)C_2 \qquad (2.47)$$

$$2^+ \qquad e(n - \tfrac{1}{2}) - q_0 = (V_g - V_2)C_g + (V_1 - V_2)C_1 \qquad (2.48)$$

$$2^- \qquad -e(n + \tfrac{1}{2}) + q_0 = (V_2 - V_g)C_g + (V_2 - V_1)C_1 \qquad (2.49)$$

These are well established equations in their general form. When plotted we can obtain the recognisable diamond shaped stability domains of an SET, as can be seen in figure 2.7.

By slicing along the axis of the stability plot, we can obtain $I - V_b$ and $I - V_g$ curves detailing the characteristics of the SET.

The $I - V_b$ characteristic for an SET slices through only one stable domain and is well established, as can be seen in figure 2.8. This is the well established IV characteristic of an SET. As can be been, for large bias linear behaviour is displayed. However the slope just after the coulomb blockade threshold, $e/2(C_1 + C_2 + C_g)$, is different. At small bias, but still slightly larger than the threshold, two possible and equally likely tunnel events can occur, where an electron can either enter the island through the first junction or leave the island through the second junction, therefore allowing two simultaneous conduction channels (assuming the capacitances of each
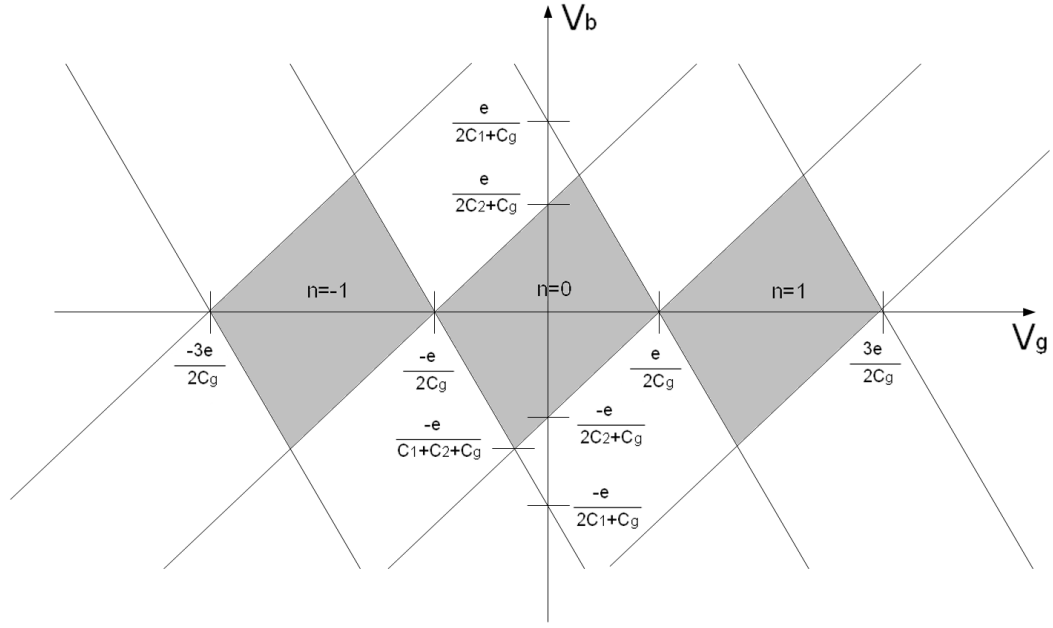
Figure 2.7: SET Stability domains, represented by shaded areas.

junction are equal). This has the effect of two resistors in parallel. As half the bias decreases across the first junction and similar across the second, this gives effective junction resistances of $2R_1$ and $2R_2$. The total resistance being the parallel combination of both of these. This demonstrates the space correlated tunnelling across the junctions, as once an electron enters the island it will quickly leave as it charges the island and therefore will increase its tunnel rate, therefore showing that one junction will quickly compensate for the other.

From figure 2.8, we may also calculate the charging energy of the superconducting SET directly using

$$V_{SP} = \frac{4\Delta + 2E_g}{e} \tag{2.50}$$

where V_{SP} the change in voltage along the Coulomb blockade region, 2Δ is the superconducting band gap of the material and E_g is the charging energy of the SET. The superconducting band gap and charging energy are doubled as we take into account two tunnel junctions. In the case of aluminium, the superconducting band gap at 0K is approximately $3.4 \times 10^{-4} eV$.

When we take a slice across the remaining axis in figure 2.7, we slice through

27
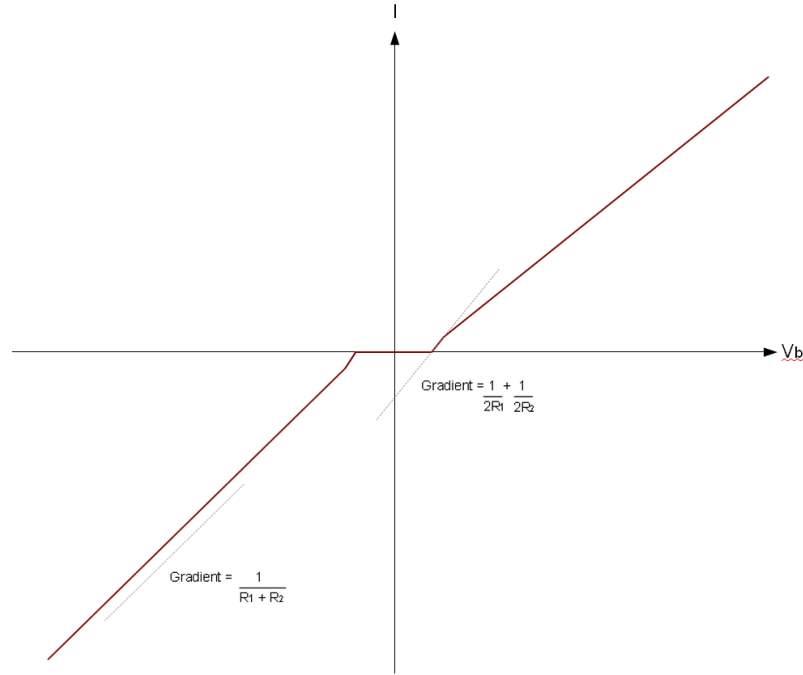
Figure 2.8: Idealised I-V curve for an C-SET. This assumes that the junctions are identical, thus $R_1 = R_2$ and $C_1 = C_2$.

many stable regions at different junction bias. This slice clearly displays the coulomb blockade oscillations with period e/C_g as already discussed. This can be seen in figure 2.9.
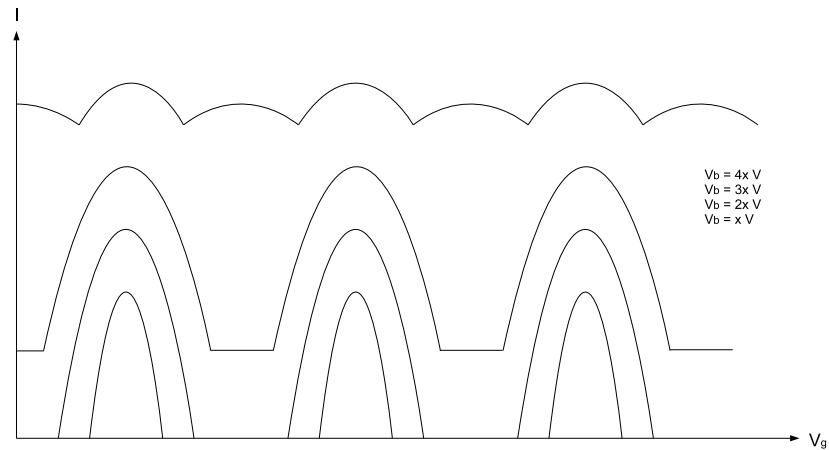
Figure 2.9: Idealised Coulomb blockade oscillations of a SET at different bias. This assumes that the junctions are identical, thus $R_1 = R_2$ and $C_1 = C_2$.

Experimentally, a current response map can be taken which will include all these regions, as can be seen in figure 2.10.
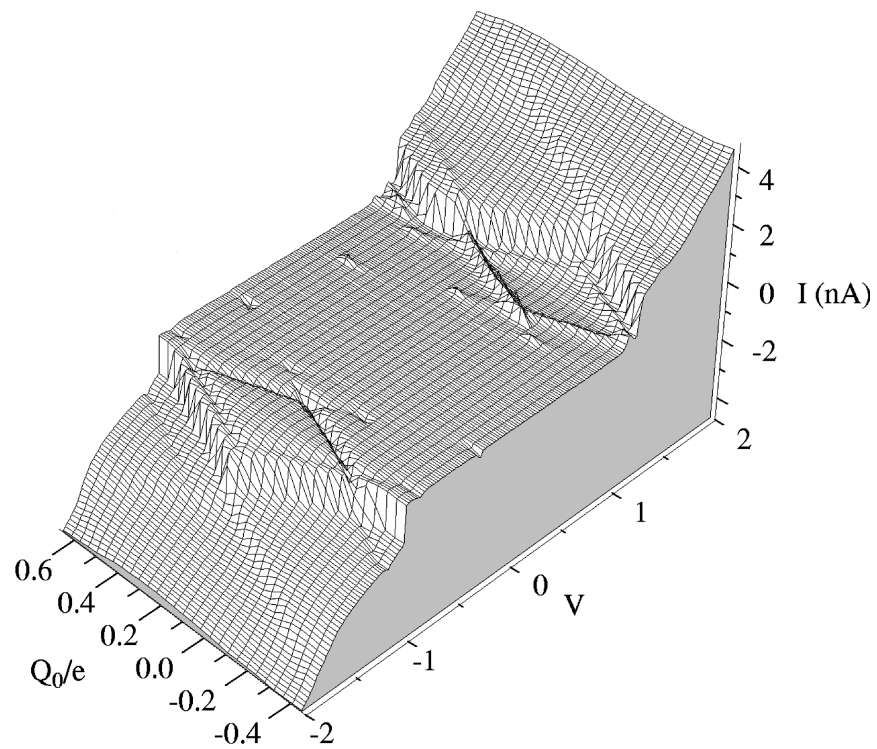
Figure 2.10: SET Current response map as a function of bias voltage and gate charge. The diamond stability regions can be clearly seen as well as the characteristic SET I-V curve. The small pits/rises that can be seen on the plane are quasi particle points.[45]

2.2.2 Two Dimensional Electron Gases (2DEG)

This section will outline and explain the fundamentals of a two dimension electron gas (2DEG) formed in single and double quantum wells. High mobility 2DEGs are used in many electronic devices today. Typically high electron mobility transistor have a triangle quantum well with the metallic gate on top of the semiconductor as can been seen in figure 2.11. One can control concentration of electrons in 2DEG, and thus affecting conductance of the channel, by changing the gate voltage.
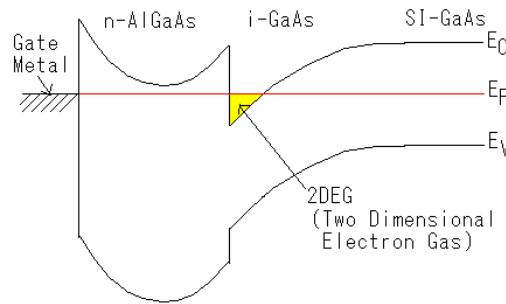
Figure 2.11: Figure illustrating the energy bands of a basic high electron mobility transistor, and how a 2DEG forms in the triangular quantum well.

2.2.2.1 Structure and Formation

The 2DEG in a semiconductor is created by band gap engineering. Precise layers of different composition materials (and therefore different conduction and valence band energies) with similar lattice constants are grown on top of each other. A popular material to grow heterostructures with is GaAs/AlGaAs, which, by varying concentrations of AlGaAs in the form of $Al_xGa_{1-x}As$, atomic layers can be engineered from AlAs to GaAs. Both materials of which have similar lattice constants, allowing layers of different parameters to be grown on top of another without the problem of stressing. Heterostructures are usually grown with chemical vapour deposition (CVD) or molecular beam epitaxy (MBE).

As can be seen from figure 2.12 the energy band gap of the structure varies with depth. Thus quantum wells of particular depth and width can be formed and are called compositional quantum wells. With the addition of doping, these wells can then be filled with excess electrons thus forming a 2DEG. An example of such a structure, which was used for fabrication in this project, can be seen in figure 2.12.
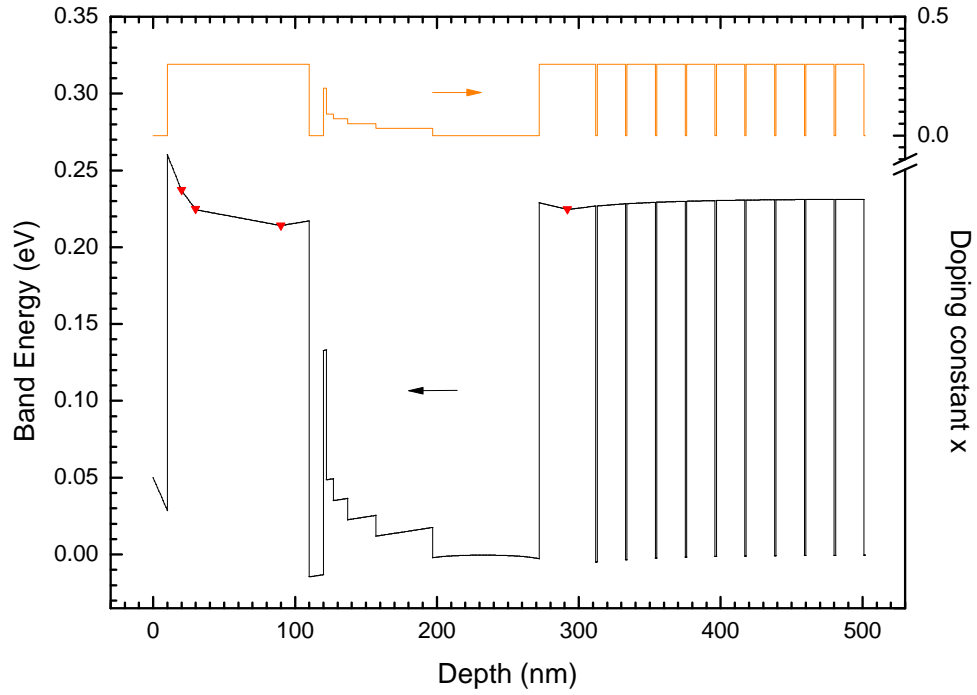
Figure 2.12: Bottom graph illustrates the conduction band energy at 0K of the stacked GaAs/AlGaAs 2DEG heterostructure used for fabrication. The red arrows indicate the locations of delta doping. The repeating periods between 300nm and 500nm are used as buffering to restrict current in the z-direction. Energy bands are shifted to *GaAs = 0eV*. Top graph illustrates the corresponding Al fraction as a function of depth.

2.2.2.2 Ideal Two Dimensional Electron Gas

Unlike free electrons, which can move in all directions, the electrons in 2DEGs are confined in the z direction and free in the x and y directions, thus the energy of an electron in a 2DEG is

$$E = \frac{\hbar^2}{2m^*}(k_x^2 + k_y^2) \tag{2.51}$$

where k_x^2 and k_y^2 are the wave vectors in the x and y direction of a given electron and m^* the effective mass. Therefore the number of states in **k**-space of dimensions $d\mathbf{k} = dk_x dk_y$, taking into account a factor of 2 for electron spin degeneracy is

$$g(\mathbf{k}) = \frac{2}{(2\pi)^2} \tag{2.52}$$

By substituting for polar coordinates, where $k = (k_x^2 + k_y^2)^{1/2}$, we can show

$$g(\mathbf{k})d\mathbf{k} = \frac{2}{(2\pi)^2}d\mathbf{k} = \frac{1}{\pi}kdk \tag{2.53}$$

The density of states can now be expressed in terms of energy using equation (2.51);

$$\frac{1}{\pi}kdk = \frac{1}{\pi}k\frac{dk}{dE}dE = \frac{m}{\pi\hbar^2}dE \tag{2.54}$$

Thus giving us the density of states as below, showing that it is a constant.

$$g(E) = \frac{m}{\pi\hbar^2} \tag{2.55}$$

2.2.2.3   Real Quantum Wells

Electrons in a quantum well may be treated using the effective-mass approximation. The wavefunction as described by the Bloch theorem can be written as

$$\phi_{\mathbf{k}}(\mathbf{r}) \approx \phi(\mathbf{r})u_{\mathbf{k}}(\mathbf{r}) \tag{2.56}$$

where $u_{\mathbf{k}}(\mathbf{r})$ is the Bloch function, which describes the rapidly varying crystal part of the wavefunction due to a periodic potential and $\phi(\mathbf{r})$ is the envelope (plane) wave function, which describes the part of the wavefunction that varies slowly on the atomic scale. The envelope function follows an equation similar to the Schrödinger equation and for GaAs quantum well has the form

$$\left[-\frac{\hbar^2}{2m^*}\nabla^2 + V(\mathbf{r})\right]\phi(\mathbf{r}) = E\phi(\mathbf{r}) \tag{2.57}$$

where V does not include the crystal potential, but does include the effect of all external potentials and potential changes due to conduction band edge, and E is measured from the conduction band edge. The crystal potential is instead included using an effective mass, which as such, changes the mass of the electron in the equation from m_e to m^*. In the case of GaAs the effective mass approximately equals to $m^* = 0.067m_e$.

When one represents the compositional wells as the infinite ideal square wells, it can be shown that there are plane wave solutions for the Schrödinger equation in

the x and y direction. The z direction is separated out, as it is assumed motion in this direction is restricted. Therefore $\phi(z)$ can obey the one-dimensional Schrödinger equation for a particle in an infinite square well. This has the well know solution

$$E_n = \frac{\hbar^2 \pi^2 n^2}{2m^* d^2} \tag{2.58}$$

where d is the width of the well and $n = 1, 2, 3....$ Therefore the total energy of the electron in the well consists of the sum of the kinetic energy in the x-y plane, equation (2.51). This leads to

$$E = E_n + \frac{\hbar^2}{2m^*}(k_x^2 + k_y^2) \tag{2.59}$$

It can be seen already that there are a few differences between the electron gas in the quantum well and that of an ideal 2DEG. There can be several different quantised energies E_n, meaning several possible states in the z-direction and the electron wavefunctions have a finite spread in the z-direction. The E-k dispersion relation is therefore a generalisation, with the parabolic dispersion relation as defined by equation 2.51 being a specific case. Instead the dispersion relation as defined by equation 2.59, where E_0 is defined using equation 2.58 with $n = 1$, can be see in figure 2.13.
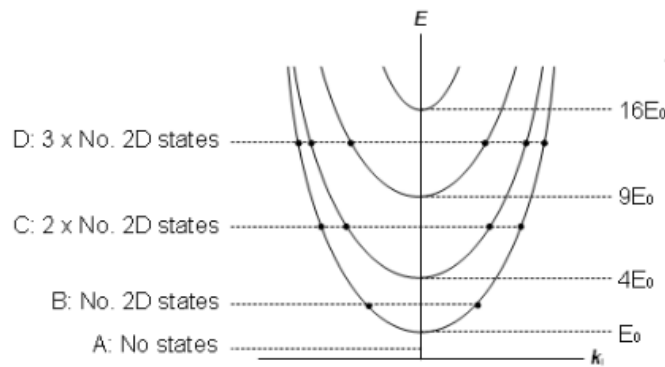
Figure 2.13: E-K dispersion relation for an infinite square well.

It can be seen that at position A, where $E < E_0$ there are no states present. When the energy falls in the range $E_0 < E < 4E_0$ as is shown at position B, the density of states (DOS) is the same as a perfect 2DEG, as described by equation 2.55. For the

range $4E_0 < E < 9E_0$, position C, the DOS is $2 \times g_0$ and for energies $9E_0 < E < 16E_0$, position D, the DOS is $3 \times g_0$, and so on.

The DOS per unit volume can be found by dividing $g(E)$, which is the DOS per unit area, by d, the width of the well. This gives us a 3D DOS for the infinite square well, as can be seen in figure 2.14.
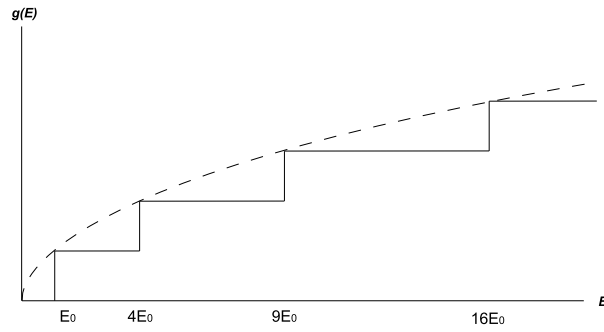
Figure 2.14: Showing the DOS for the infinite square well. Dotted line is the DOS for the 3D system for comparison.

2.2.2.4 Carrier Concentration and Mobility

Two predominant properties of 2DEGs, as with regular semiconductors, are the carrier concentration and carrier mobility. When taking into account minority and majority characters, i.e. the electrons and holes in the material, it can be shown that in an intrinsic n-type material, where the majority carrier is the electron, that the carrier concentration is:

$$n = Ce^{-(E_g - E_f)/k_b T} \tag{2.60}$$

Where n is the carrier concentration, E_g is the energy gap, E_f the Fermi energy, k_b the Boltzmann constant, T the temperature and C is a constant.

However, this relation does not hold true for dopped semiconductors. The carrier concentration can be found using the Hall Effect.[46] The hall field, ε_H is proportional to the strength of the magnetic field B_z and the current density in the x direction, J_x and R_H which is the Hall Coefficient:

$$\varepsilon_H = R_H J_x B_z \tag{2.61}$$

It can also be shown when taking into equilibrium forces acting particles in the semiconductor that:

$$\varepsilon_H = B_z v \tag{2.62}$$

where v is the velocity of the electron. Given equation 2.62 and $J_x = Nve$ that the Hall Coefficient is equal to:

$$R_H = \frac{\varepsilon_H}{J_x B_z} = \frac{B_z v}{N e v B_z} = \frac{1}{Ne} \tag{2.63}$$

where N is the bulk carrier concentration.

The carrier concentration can also be found using the Shubnikov-de Haas effect[47]

$$n_s = \frac{e/ch}{\Delta(\frac{1}{H})} \tag{2.64}$$

where n_s is the sheet carrier concentration (the concentration of the two dimensional cross section of the device), c the speed of light, h planks constant and $\Delta(\frac{1}{H})$ is the change in the inverse applied magnetic field. In this equation, the units are in CGS.

The mobility of the semiconductor is defined as a quantity relating the drift velocity of charge carriers to the applied electric field. The mobility of a charge carrier can be defined as

$$v_d = \mu E \tag{2.65}$$

where v_d is the drift velocity of the charge carrier, μ the mobility of the charge carrier and E is the applied electric field. It is related to the conductivity of semiconductors by

$$\sigma = \mid e \mid (n\mu_e + p\mu_h) \tag{2.66}$$

where n and p are the concentration of electrons and holes respectively, and μ_e and μ_h are the mobility's of electrons and holes respectively. In the case of a 2DEG, where only electrons are present, this can be re written as

$$\sigma = \mid e \mid n\mu_e \tag{2.67}$$

Given that

$$\rho = \frac{1}{\sigma} = \frac{RWD}{L} \tag{2.68}$$

where R is the resistance, and W, D and L are the width, depth and length of the sample respectively, and the sheet resistance is

$$R_{sh} = \frac{RW}{L} \tag{2.69}$$

we can obtain the following expression for the mobility

$$\mu = \frac{1}{R_{sh}dne} \tag{2.70}$$

When taken that $n_s = nd$, we can obtain this final equation for the mobility

$$\mu = \frac{1}{R_{sh} n_s e} \tag{2.71}$$

2.2.2.5 Plasma Oscillations

2DEGs, similar to metals, have free electrons that move within the semiconductor structure. It can sustain a plasma oscillations (also known as Langmuir waves), where the electron density can rapidly change and oscillate. The quantization of this process leads to the quasiparticle known as the plasmon.[48] If a plasma of electrons, about a periodic lattice of positive ions, is shifted slightly with respect to the positive ions, then a Coulomb force will be produced to restore the electron plasma to the original position. At low temperatures it can be shown that the frequency at which the plasma charge density oscillates is equal to:

$$\omega_{pe} = \sqrt{\frac{n_e e^2}{m \epsilon_o}} \tag{2.72}$$

where n_e is the electron density, e is the electric charge, m is the effective mass of the electron, and ϵ_o is the permittivity of free space.[49] The energy of individual plasmons in the free electron model, which is used to describe infinite homogenous 2D electron system, can be estimated using equation (2.72) and the relation $E = hf$ to give

$$E_p = \hbar \sqrt{\frac{n_e e^2}{m \epsilon_o}} \tag{2.73}$$

The dispersion relation however is the more commonly used term to describe the plasma system, in the case of a 2DEG layer it is well known to be[50]

$$\omega_p^2 = \frac{e^2 N}{m^* \varepsilon_0 \bar{\varepsilon}} k \tag{2.74}$$

where k is the wave vector of the plasma wave, ω_p is the frequency of the plasma wave, N is the areal electron density and $\bar{\varepsilon}$ is the effective dielectric function.

This function can take a few forms depending on the geometry of the sample in question. For example, when a 2DEG layer separates two semi-infinite layers with a dielectric constant of ε_1 and ε_2, the effective dielectric function can be taken to be

$$\bar{\varepsilon} = \frac{\varepsilon_1 + \varepsilon_2}{2} \tag{2.75}$$

In the case where we may imagine an insulator, with dielectric ε_2 and thickness d, is

superimposed onto the 2DEG layer, which inturn is on the surface of a semi-infinite substrate with dielectric constant ε_1, the dielectric function would take the form of

$$\bar{\varepsilon} = \frac{1}{2}\left(\varepsilon_1 + \varepsilon_2 \frac{1 + \varepsilon_2 \tanh(kd)}{\varepsilon_2 + \tanh(kd)}\right) \tag{2.76}$$

However when the 2DEG layer has a conductive gated region located at a distance, d, away from it, this will effect the frequency dispersion of the plasma waves within the 2DEG. Assuming the gate is infinite and perfectly conductive at a distance, d away from the infinite plane of 2DEG, then the dispersion relation becomes[51]

$$\omega_p^2 = \frac{e^2 N}{m^* \varepsilon_0 [\varepsilon_1 + \varepsilon_2 \coth(kd)]} k \tag{2.77}$$

where ε_2 is the dielectric constant of the insulator between the conductive gate and the 2DEG. If the conductive gate is close enough to the 2DEG, so that $kd \ll 1$, then equations 2.77 becomes

$$\omega_p = \sqrt{\frac{e^2 N d}{m^* \varepsilon_0 \varepsilon_2}} k \tag{2.78}$$

Assuming we define the phase velocity as $s = \frac{\omega}{k}$, we can see that the phase velocity of the plasma waves are independent of the frequency. Using the gradual cannel approximations, the areal electron density within a gated region of the channel can be found using a version of the parallel plate capacitance

$$N = \frac{\varepsilon_0 \varepsilon_2}{ed}(U_g - U_{th}) \tag{2.79}$$

where U_g is the gate voltage and U_{th} is the voltage required to deplete the channel. By substituting equation 2.79 into equation 2.78, the plasma frequency takes a simplified form

$$\omega_p = sk \tag{2.80}$$

where $s = \sqrt{\frac{e(U_g - U_{th})}{m^*}}$. Using the gated FET approximation, which assumes identical boundaries due to the gate, the frequency of plasma oscillations can be approximated to the simple formula[52]

$$\omega_n = \frac{\pi s}{L_{eff}} n \quad (n = 1, 2, 3, ...) \tag{2.81}$$

where $L_{eff} = L + 2d$ and d is the distance between the 2DEG layer and the gate. The above equation with the standard parameters of a semiconductor heterostructures results in plasmon frequencies in the terahertz range.

It has been found that resonant absorption of terahertz radiation within a 2DEG is caused due to the excitations of plasma oscillations under a gated region. The gated region causes fields from the incoming radiation to become scattered into the 2DEG, causing the excitation of plasma oscillations. The incoming radiation, assuming a plane wave, does not tend to directly excite oscillations in the 2DEG due to the momentum conservation law, where the photon and plasmon wave vectors would need to match. It was also noted that if the gate is to far away from the 2DEG layer, the resultant scattered fields that reach the 2DEG are to weak to excite any plasma oscillations, there the plasmon-photon interaction is weak. Similarly if the gate is too close, the gate will screen the plasma oscillations, again resulting in weak plasmon interaction. Once a resonant plasma oscillation has been established in the 2DEG, the resultant plasmons have strong leakage into non-gated regions of the 2DEG, allowing non gated regions to be excited by a neighboring gated region.[51] These excitation can then either be absorbed by a metal, eventually disperse, or decay by a process of handing over the excess energy in the form of an electron.

2.2.2.6 Tunnelling Conductance and Extensions to Double 2DEGs

As with single 2DEGs, double 2DEGs are grown using precise band gap engineering in heterostructures to form super latices and quantum wells, using the same types of growing techniques as described above. They exhibit many of the same properties as individual 2DEGs, however their interaction with each other may also be modelled.

It was originally predicted that the conduction in the z direction in single 2DEGs would produce unusual properties, such as negative differential resistance[53], meaning the greater the applied voltage in the z direction, the lower the current would become. This was then later proved in a GaAs/AlGaAs heterostructure super lattice.[54]
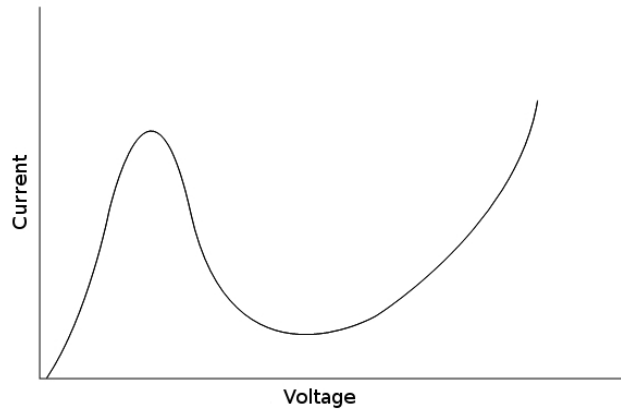
Figure 2.15: 2DEG I-V characteristic showing negative differential resistance.

Due to the negative differential resistance, oscillations in tunnelling can be observed, with the phenomena of resonant tunnelling also be observed. This resonant tunnelling gives rise to many interesting applications, such as Gunn Diodes, logic and memory circuits[55] and applications to SETs.[56] It can be shown that structures with negative differential resistance can present charge oscillations if we consider the following

$$I = G(V)V \tag{2.82}$$

where G is conductance and V, voltage. From this we may define

$$\frac{dI}{dt} = v_d \left(V \frac{dG}{dV} + G \right) \frac{dV}{dz} \tag{2.83}$$

where v_d is the drift velocity of the electrons. Using Poisson's equation we then define how the electronic charge behaves. Using

$$E(z) = -\frac{dV}{dz} = \frac{q}{\epsilon}N_s(z) \tag{2.84}$$

where $N_s(z)$ is a bounded area of electron density at positon z, q the charge and ϵ the permittivity of the material. If we define the following

$$\omega(z) \equiv \sqrt{v_d\left(V\frac{dG}{dV} + G\right)\frac{N_s(z)}{\epsilon}} \tag{2.85}$$

we can then see that the charge follows a similar law to that of a harmonic oscillator

$$\frac{d^2q}{dt^2} + \omega(z)^2 q = 0 \tag{2.86}$$

It can be seen that in this format, that equation 2.85 is a frequency dispersion relation. It can be seen that when in the negative differential resistance regime that it would become an imaginary number for $\frac{dG}{dV} < -\frac{G}{V}$. It can therefore be interpreted that charge builds at a specific rate when in the negative differential regime, where the charge spike travels along the sample and decays.

In a double 2DEG system, we can consider two coupled quantum wells or a triple barrier system, the centre barrier being the separation between the two quantum wells. The overlap of the two quantum wells wavefunctions and associated eigenstates is therefore dependent on the thickness of the middle barrier, energy splittings such as this has been observed using resonant tunnelling spectroscopy.[57] The two wells can also be capacitively coupled, as governed by coulombs law, or have direct coulomb interactions between the neighbouring electrons via the Coulomb gap.[57]

The wavefunction coupling and interactions between the two quantum wells can be understood by understanding how the individual wavefunctions overlap. The wavefunctions can be shifted by applying a bias to one of the QWs, causing the quantum well potential to be deformed and causing the wavefunction to shift. This is particularly enhanced in non-symmetric quantum wells, where the wavefunctions become distorted as they overlap neighbouring wavefunctions via the intermediate

barrier. In the case of non-symmetric wells the biasing of one or both quantum wells can allow possible separate wavefunctions of different orders of both wells to become more strongly coupled.

Predominately the modeling of the resonant tunnelling across a triple barrier or between two quantum wells, is done using the Wigner and Landauer models. These models only consider the direction of electrons in the z direction, i.e. the tunnelling current between the potential barriers. The Wigner approach is used to find the current density and starts with using a variable effective mass Hamiltonian and includes a double well potential.[58,59] It is a favoured approach as it is very similar to that of the Boltzmann distribution function.[60] The full derivation to the final expression is not included here, as it is not within the scope of this project, however for completeness it can be found in appendix A. The final expression for current density using the Wigner approach is found to be

$$J(Z) = e \int_{-\infty}^{\infty} \frac{dk}{2\pi} \frac{\hbar k}{m(Z)} f(Z, k) \tag{2.87}$$

The Landauer function can be used to obtain the current between the external electrodes attached to a triple barrier system. It is formed by defining the standard definition of average current. The full derivation can be found in appendix B. The resulting current can be found, where I_{STT} is known as the standard tunnelling theory current, to be

$$I_{STT} = \frac{emAKT}{2\pi^2\hbar3} \int d\varepsilon T(\varepsilon) F(\varepsilon) \tag{2.88}$$

where $T(\varepsilon)$ is the tunnelling probability and $F(\varepsilon)$ is the electron equilibrium distribution.

2.2.2.7 Plasma Excitation Interaction in Double Quantum Well Systems

As well as plasmon interaction in a SQW, there are considerable manifestations of plasmon interactions between layers in a DQW system, where the tunnelling coupling is special modulated, i.e. the construction of the QWs affects the strength of coupling. In such system, there are two extreme regimes of either purely coulomb coupling[61] and purely tunnel coupling,[62, 63] with the majority of systems being a mix of both.

In coulomb coupling, as well as the standard interactions between charged particles, producing coulomb interaction, there are two types of plasma excitations, optical and acoustical.[61] The optical plasmon excitation presents itself as an in-phase density oscillation in the two layers, with a non-linear dispersion relation of the form of $\omega \sim k^{1/2}$. The acoustical plasmon presents itself as an out of phase density fluctuation with a linear dispersion relation of the form $\omega \sim k$.

For the acoustic mode, similarly charged carriers oscillate out of phase, or oppositely charged carriers oscillate in phase, resulting in the characteristic linear dispersion. When similarly charged carriers oscillate in phase, or oppositely charged carriers oscillate out of phase, the so-called optic plasmon mode results. A representation of the two plasmons can be seen in figure2.16.[61]
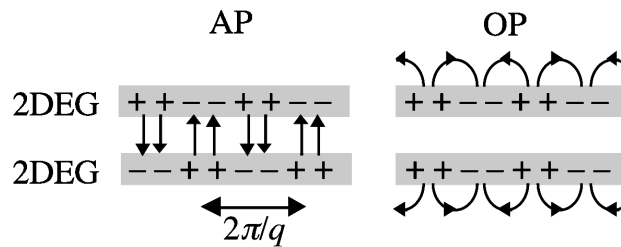
Figure 2.16: Representation of an acoustical and optical plasmon with wave vector q. The arrows represent the contribution to the electric field, causing either accumulation or depletion of electrons.[61]

When considering the interaction between layers, as well as the coulomb interaction and intralayer kinetic energies, we must also consider a gap in between the common quantum subbands in the two layers, adding to the energy landscape. It has been shown that a symmetrical system, where both QW have the same dimensions and carriers concentrations, there are two plasma modes and in non-symmetrical

system, there are three. The general solution[64] to finding the number of modes with in a system, assumes there are always three modes, with the acoustical plasmon, which is the out of phase density fluctuation in the two lowest quantum subbands, being Landau damped in the symmetrical state unless the following condition is met

$$\left(1 - \frac{n_2}{n_1}\right)\left[1 + \frac{a}{2D'(0)}\right]^2 < 1 \tag{2.89}$$

where a is the effective Bohr radius, n_1 and n_2 are the electron densities in the symmetrical/antisymmetrical quantum subbands and

$$D'(0) = \frac{dD}{dk}\bigg|_{k=0} \tag{2.90}$$

where

$$D(k) = I_{1111}I_{2222} - I_{1122}^2 \tag{2.91}$$

and

$$I_{ijkl} = <\psi_i(z)\psi_j(z)|\exp[-k|z - z'|]|\psi_k(z')\psi_l(z') > \tag{2.92}$$

where I_{ijkl} is a fourth rank tensor where $i, j, k, l = 1$ or 2 which indicates the 2DEG layer index and where $\psi_{1,2}(z)$ are the symmetrical/antisymmetrical electron wave function envelopes. I therefore describes the resultant wavefunction envelope due to the interaction between the wavefunctions of the two 2DEG layers. From this, no limitations on the number of plasmon's are imposed due to symmetry of the wavefunctions, and the symmetry only affects the properties/behaviour of the plasmon's.

It has been shown that varying the spatial symmetry changes the nature of the acoustical plasmon and the intersubband plasmon, which is considered to be a density fluctuation relating to the excitation from the lowest subband to the next.[65] In the symmetrical system, the intersubband plasmon, like the acoustical plasmon, demonstrates a positive linear dispersion. It can be seen to be as an out of phase density fluctuation in the opposite layers, that actually dominates over the electron motion in the transverses directions of each layer at $t/v_F k < 1$, where v_F is the Fermi

velocity, t is the symmetric/antisymmetric tunnelling gap energy. $v_F k$ describes the intralayer kinetic energy.

We can define the intersubband plasmon in the symmetrical system as a tunnel plasmon, as the intersubband plasmon in the antisymmetrical state does not have a linear dispersion, but a square dispersion. So by changing the bilayer system symmetry a tunnel plasmon will change to an intersubband plasmon and also, an acoustical plasmon will appear.

In a weakly tunnel coupled system, it has been shown that the dispersion relation of the tunnel plasmon at $v_F k > t$ has a positive dispersion relation with a slope very close to that obtained by classical electrodynamics for an acoustical plamson in two electron sheets, given by[66]

$$\omega^2(q) = \frac{2\pi e^2 k}{\epsilon_\infty m^*}(N_1 + N_2)\left[\frac{1}{2} - \frac{1}{2}\sqrt{1 - \frac{4N_1 N_2}{(N_1 + N_2)}(1 - e^{-2kd})}\right] \qquad (2.93)$$

where N_1 and N_2 are the electron densities in the separate layers and d is the distance between layers. Equation 2.93 can be used to show how the nature of such a system can lead to terahertz detection when a DQW QD sensor is realised. By assuming the wavevector, k, to be approximately equal to the inverse diameter of the QDs, $k = \frac{1}{2r_{QD}}$, and with the radius of the QDs studied here being approximately $0.5 \times 10^{-6} m$, this gives a value of $k = 1 \times 10^6$. Using values of $N_1 = 3.2 \times 10^{15} m^{-2}$ and $N_2 = 4.4 \times 10^{15} m^{-2}$ also, we obtain a dispersion frequency of 0.6THz.

The symmetry of the layers, relating to the confining potential may be defined by

$$\delta = \frac{N_1 - N_2}{N_1 + N_2} \qquad (2.94)$$

where N_1 and N_2 in this case are the are the ionized donor densities. These are not directly measurable however. In the antisymmetric state, where the wavefunctions of the two lowest subbands are confined in separate layers, see figure 2.17, we may assume $N_{1,2} \approx n_{1,2}$. As we can find the electron densities of the layers, we may then extrapolate what δ will be. By depleting individual wells near this limit, we may find δ as function of depletion power and extrapolate to $\delta = 0$, where it has been

experimentally found that at $\delta = 0$, the intersubband energy, (Ω), has a minimal value and is equal to the tunnelling gap as is expected.[66]
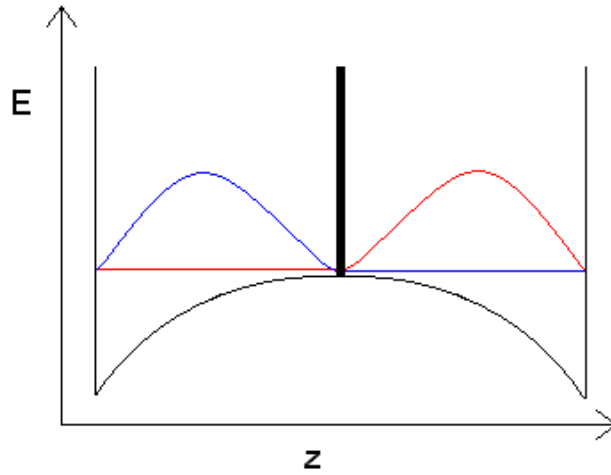
Figure 2.17: Antisymmetric plasma excitation state of a DQW heterostructure. The antisymmetric state is caused by depleting one well more than the other. In this case we may assume that the electron densities are approximately equal to the ionized donor densities. We see here how the two lowest subbands are distorted due to the concentrations in each QW. This will cause a tunnel plasmon to become a intersubband plasmon, with an acoustical plasmon appearing also.

As the layers become more asymmetric and δ increases, the intersubband energy becomes defined by the electric fields within each layer and the dimensions of the layers. By further increasing δ by depleting one well, Ω will increase, and the tunnel plasmon to convert to an intersubband plasmon, with energy defined by Ω.

2.2.3 Quantum Dots (QD)

When electrons are confined in all three dimensions, a Quantum Dot (QD) can be formed, which if the confinement distance is smaller than the mean free path of the electron, is a zero dimensional device. Quantum dots are usually formed with in a semiconductor material, such as an AlGaAs hetrostructure, via a confinement technique which may include physically reducing the dimensions of a given area, or using a potential to confine a given area.[67] This will usual be done within a 2DEG layer, as described in section 2.2.2, as this removes the need for confinement in the z-direction. Quantum dots are typical in the order of 100nm in size.[68]

2.2.3.1 Formation of Quantum Dots

Isolated QDs can be formed in two different types of configuration, these are the lateral QD as can be seen in figure 2.18 and the stacked, or vertical QD, as can be seen in figure 2.19. QD dots originally emerged with the improvement in heterostructure growth technology, as described in section 2.2.2. At first, vertical quantum dots were formed by etching pillars using e-beam technology into semiconductor heterostructures. By analysing the IV characteristic of such devices, it revealed a structure that was attributed to resonant tunnelling through quantum states, due to the lateral confinement.[69]
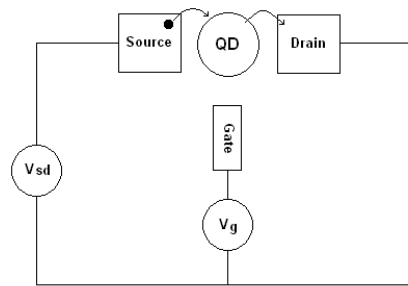
Figure 2.18: Schematic illustration of a lateral QD that has been coupled with tunnel junctions to a source and drain, and capacitively coupled to a gate.

With 2DEGs as the starting point, lateral QDs were fabricated using metallic gates to isolate a region within the 2DEG, as done in this project, forming tunnel barrier or quantum wires using negatively applied voltages.
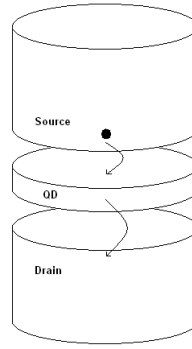
Figure 2.19: Schematic illustration of a vertical QD that has been coupled with tunnel junctions to a source and drain. This may also be constructed to include a gate as in figure 2.18

These systems often show ballistic electron transport, as the mobility of electrons in some of the highest reported cases in a 2DEG can be in the order of $1000m^2V^{-1}s^{-1}$ [67] which equates to a mean free path of the order $100\mu m$.[67] Also the Fermi electron wavelength within 2DEGs, which have typical carrier densities of $n_s = 1-5x10^{15}m^{-2}$, are approximately

$$\lambda_F = \left(\frac{2\pi}{n_d}\right)^{\frac{1}{2}} \sim 80 - 30nm \qquad (2.95)$$

which is approximately 100 times larger than that of metals. Quantum confinement can also be demonstrated in such devices, with the manifestation of quantised conductance steps in wires and dots due to the comparable wavelength of the electron to the device.[70]

Devices can also be fabricated to dimensions where quantum confinement becomes apparent and quantized conductions steps in such structures as quantum wires and point contacts in two dimensions has been shown.[71] Quantum confinement in varying gate geometry's has presented a broad scope of transport phenomena, such as coherent resonant transmission through a quantum dot[72] and quantum dot array[73]. Experiments such as these have been performed with barrier conductances less than e^2/h, where the effects of charge quantisation are significant and at greater barrier conductances, where its effect is less noticeable.

Single electron charging of "accidental quantum dots" was first shown in narrow wires with unintentional impurities along the wire, forming these unplanned

quantum dots.[74] The conductance of the wire was much less than e^2/h. This led to the discovery of a periodic oscillation in the conductance as a function of the voltage of a coupled gate. It had been shown that the quantum dots formed along the wire due to the impurities in it, were charging by single electrons at a time.[75]
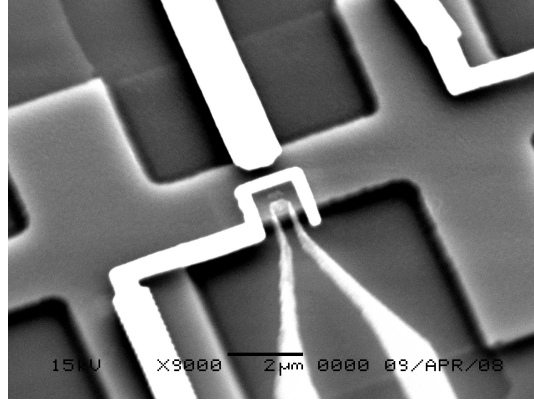
Figure 2.20: SEM image of QD system studied in this project.

The lateral quantum dot has been studied the most out of the possible configurations. This is usually defined using negatively biased metallic gates. An image of such a device studied in this project can be seen in figure2.20. The tunnel barriers between the QD and surrounding 2DEG are defined by applying a negative voltage to the metal gate. This system also has a point contact coupled to the QD. The scheme of the device is shown in figure 2.21. Although the gate dimension is of the order 1.4 μ m, the size of the dot its self is slightly smaller because of depletion region produced by the negatively biased gate.
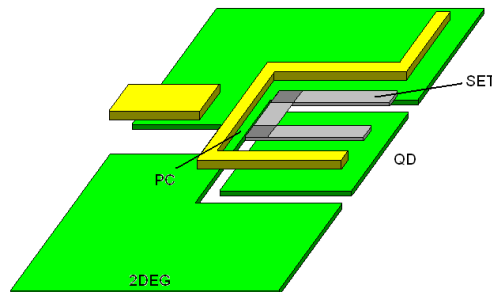
Figure 2.21: Schematic illustration of single QD system used in single QW system that was developed.[13]

2.2.3.2   Properties of Quantum Dots

This section will discuss the principle properties of QDs that are regularly probed; the quantum energy level spacing and the charging energy. It is important that the local thermal energy, $U = k_b T$, be less than the energy level spacing and charging energy, otherwise they will be thermally screened out.

Electrons with in a QD reside in 0D energy states, taking on a delta function like appearances, as shown in figure 2.22. The 2D energy levels are shown for comparison.
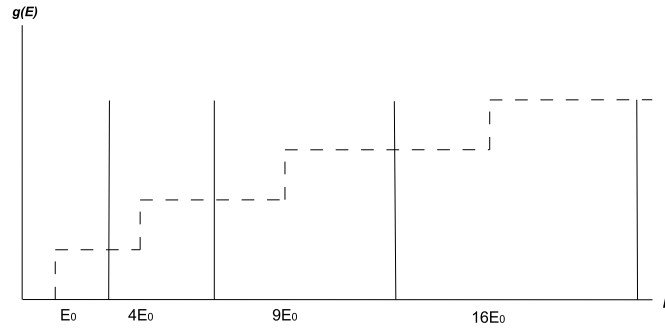
Figure 2.22: Illustration of 0D densities of states versus energy level. Dashed line represents 2D DOS for comparison.

It can be seen that density of states within a QD follow a delta-function like pattern. The energy gap spacing between the levels can be estimated using

$$\Delta E = \frac{\hbar^2}{m^* R^2} \qquad (2.96)$$

where GaAs $m^* \approx 0.067 m_e$. As described in section 3.1, the approximate circular diameter of the gates used to isolate the quantum dots in this project is $1.4 \mu m$. It can be approximated that the QD would be of the order $1 \mu m$ in diameter, or $R \approx 500 nm$. From equation 2.96, it can be estimated that the energy level spacing of such a dot to be $\Delta E = 0.004 meV$. However, as described in section 4, the lowest temperature obtainable for this experiment is of the order $250 mK$, which equates to a thermal energy of $0.022 meV$. This therefore means that any effects from the energy level spacing will be screened out due to thermal noise. The remainder of this section will

focus on the charging energy.

The charging energy can be quickly estimated using the known equation for a capacitor

$$\frac{e^2}{C} = \frac{e^2}{8\epsilon_r\epsilon_0 R} \tag{2.97}$$

where for GaAs $\epsilon_r = 13$. Using our initial estimate of $R = 500nm$ we can see the upper limit for the charging energy is $\frac{e^2}{C} = 0.346meV$, which is well above that of the thermal energy. This however is the upper limit, as it is not taking into account other capacitances, such as the surrounding 2DEG and gates.

The main electron transport regime through is via coulomb blockade, which at low temperatures is the predominant regime. This system may be considered as a single electron transistor with a simplified schematic as shown in figure 2.18.

When you consider the direction of transport through a quantum dot, the process can be broken down into a number of different steps. First we have the higher electrochemical potential of the source, with states filled to this level, the dot with a number of filled/vacant sates that may or may not equal this electro chemical potential and the drain, which will have a lower electrochemical potential than the source and states also filled to that level. The barriers between the the source-QD and QD-drain can be considered tunnel barriers. This arrangement can be seen in figure 2.23. The drain and source electrochemical potentials, μ_{Left} and μ_{Right}, are related to the applied voltage via

$$V_{sd} = \frac{\mu_{Left} - \mu_{Right}}{e} \tag{2.98}$$

showing voltage steps are quanta's of e. The QD has states filled to the highest solid line, or $\mu_{Dot}(N)$. The addition of an electron would raise the highest potential from $\mu_{Dot}(N)$ to $\mu_{Dot}(N+1)$ or the first dashed line. $\mu_{Dot}(N)$ thus by definition is the energy required to add an extra electron to the QD. It is defined as

$$\mu_{Dot}(N) = U(N) - U(N-1) \tag{2.99}$$

where $U(N)$ is the ground state energy of a QD containing N electrons at 0K. As can

be seen in figure 2.23, no states on the QD match μ_{Left}, so no electrons may enter the QD and coulomb blockade is observed.
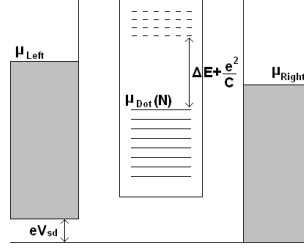
Figure 2.23: Illustration of the potential energy setup in a standard lateral QD.

Transport occurs (ignoring other non related tunnelling events) when an available energy level on the QD is equal to or less than that of μ_{Left} and where μ_{Right} is less than both. This allows an electron to enter the QD and increase $\mu_{Dot}(N)$ to $\mu_{Dot}(N+1)$. The electron will then leave the QD and the energy level will return to $\mu_{Dot}(N)$. The energy levels of the QD can be adjusted by applying a potential to the QD gate, represented as φ_N. This can be seen in figure 2.24
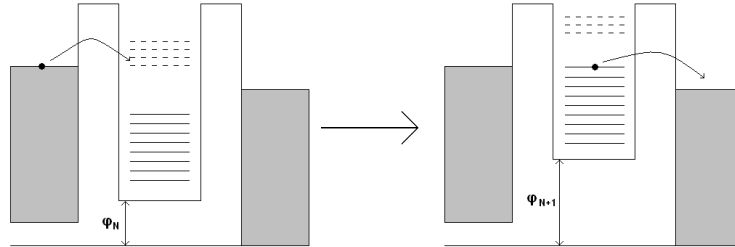
Figure 2.24: Representation of how electron transport may occur through a QD, resulting in the number of electrons on the QD switching from N → N+1 → N → N+1...

To define the value of $U(N)$, first several assumptions must be made. These are that the quantum levels of the dot are independent of the umber of electrons present in the QD. We assume there is a capacitance between the dot and surrounding environment and that this is independent of the number of electrons on the present on the QD, as the the dot is much larger than the screening length, so no electric fields can exist in the QD it self. This allows us to simplify the QD electronically to something equivalent of figure 2.25, where tunnel barriers are presented as a resistor and capacitor in parallel. We can see that the total capacitance is simply

$C = C_L + C_R + \Sigma C_g$, with a charging energy of

$$\frac{e^2}{C} = \frac{e^2}{C_L + C_R + \Sigma C_g} \qquad (2.100)$$
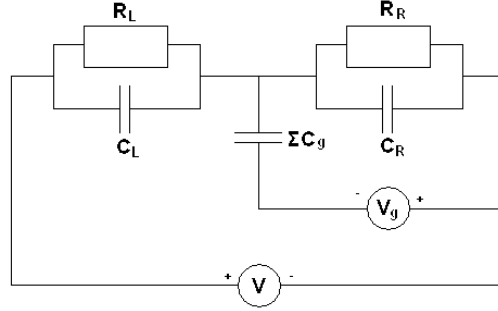
Figure 2.25: Electronic representation of a simple lateral QD design.

This linear model where $eV_{sd} << \Delta E$ and $\frac{e^2}{C}$ has been shown to lead to a electrochemical potential for N electrons on a QD as[76]

$$\mu_{Dot}(N) = E_N + \frac{(N - N_0 - \frac{1}{2})e^2}{C} - e\frac{C_g}{C}V_g \qquad (2.101)$$

where N_0 is the number of electrons present on QD at $V_g = 0$ and the single particle state energy level E_N, which is the energy level for the Nth electron, is measured from the bottom of the conduction band. It can be seen that equation 2.101 can take the following form

$$\mu_{Dot}(N) = \mu_{ch}(N) + e\varphi_N \qquad (2.102)$$

where we can see that the total electrochemical energy is the sum of the chemical energy (E_N) and the electrostatic energy. The electrostatic potential can be seen to made of two parts, these being the last two terms of equation 2.101. The middle can be seen to be discrete and the last term is continuous with V_g, so at fixed or zero gate voltage, the number of electrons on the QD, i.e. N, is the largest integer value that will satisfy the condition

$$\mu_{Right} \cong \mu_{Left} > \mu_{Dot}(N) \qquad (2.103)$$

The change in the electrochemical potential at zero gate voltage, when the number of electrons on the QD changes by one, can also be calculated. Using equation 2.101 the addition energy can be defined. It can be shown that a large energy is needed for both large energy splittings and small capacitances

$$
\begin{aligned}
\mu_{Dot}(N+1) - \mu_{Dot}(N) &= (E_{N+1} + \frac{((N+1)-N_0-\frac{1}{2})e^2}{C}) - (E_N + \frac{(N-N_0-\frac{1}{2})e^2}{C}) \\
&= (E_{N+1} - E_N) + ((N+1)-N)\frac{e^2}{C} \\
&= \Delta E + \frac{e^2}{C} \tag{2.104}
\end{aligned}
$$

At low energy, i.e. below $\mu_{Dot}(N)$, the energy levels spacings, ΔE, are only single particle energy levels and the excitation energies of the QD with a constant number of electrons, N.

Coulomb blockade occurs with a non-zero addition energy where the $(N+1)$ electron cannot enter the dot as the resulting $\mu_{Dot}(N+1)$ is larger than the reservoir potentials μ_{Left} and μ_{Right}, i.e. $\mu_{Dot}(N) < \mu_{Left}, \mu_{Right} < \mu_{Dot}(N+1)$. This can be seen in figure 2.23. As illustrated in figure 2.24 the coulomb blockade can be removed by applying a potential to the QD gate, effectively shifting the available charging energy level, $\mu_{Dot}(N+1)$, into a spacing between μ_{Left} and μ_{Right}, where $\mu_{Left} > \mu_{Dot}(N+1)$ allowing an electron to enter the QD. The increase in gate voltage causes the electro static energy to increase, which can be described as

$$
e\varphi(N+1) - e\varphi(N) = \frac{e^2}{C} \tag{2.105}
$$

and can be seen in figure 2.24. However, as can be seen now, $\mu_{Dot}(N+1) > \mu_{Right}$, so the electron now leaves the QD, causing the electrochemical potential to return to the initial value of $\mu_{Dot}(N)$. This allows the cycle of an electron to enter and leave the QD as depicted in figure 2.24 which leads to conduction oscillations from zero during Coulomb blockade and non zero, as the gate voltage is swept.

From figure 2.26, we can notice several important observations. We can see that as a conductance maximum is reached, N increases to $N+1$, while the electrochemical
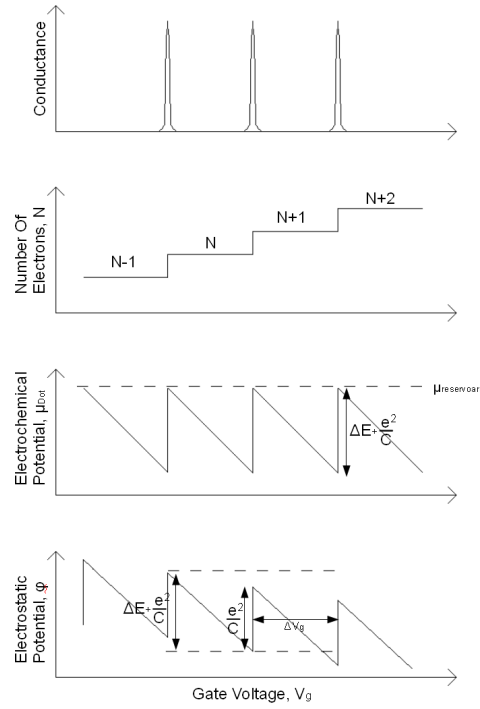
Figure 2.26: Comparison of conduction, number of electrons, electrochemical potential and electrostatic potential compared to gate voltage.[67]

potential moves by a value of $\Delta E + \frac{e^2}{C}$ and the electrostatic potential moves by a corresponding value of $\frac{e^2}{C}$. As can be seen from the graphs, we can therefore write

$$\mu_{Dot}(N, V_g) = \mu_{Dot}(N + 1, V_g + \Delta V) \qquad (2.106)$$

coupled with equation 2.101, an expression relating the change in gate voltage to the conduction oscillations may be written as[76]

$$\Delta V_G = \frac{C}{eC_g}\left(\Delta E + \frac{e^2}{C}\right) \qquad (2.107)$$

As can be seen, when ΔE is not applicable, for example due to high thermal energy, the relation becomes the standard periodic relation for single electron charging

$$\Delta V_g = \frac{e}{C_g} \qquad (2.108)$$

When ΔE is applicable, the oscillations are not completely periodic. This can be explained due to spin degenerate states, where N and $N + 1$ can be considered

56

different spin of up and down electrons within the same state.

Having established the transport theory we are now able to define three main temperature regimes, at which different forms of transport may occur. Where the thermal energy is greater than the charging energy, no charge discreetness can be observed. In this regime the conductance of the system is independent of the number of electrons on the QD and is simply the sum of the ohmic resistances of the two barriers between the QD and the reservoirs, i.e. $\Omega_\infty = \Omega_{Left} + \Omega_{Right}$, where $G_\infty = \frac{1}{\Omega_{HighTemp}}$.

The next regime is where the charging energy is less than the energy level spacing which inturn is much less than the thermal excitation energy. This is the quantum Coulomb blockade regime.[77] This regime does not exist in the current experimental setup, so will not be discussed further.

The final regime, which is the most applicable here, is where the charging energy is greater than the thermal excitation energy, but the thermal excitation energy is greater than the energy level spacing. This gives the classical or metallic Coulomb blockade which is regularly described with orthodox Coulomb blockade theory[78], which can be used to calculate predicated conduction oscillations. The line shape of individual conductance peaks are given by the following expression[79]

$$\frac{G}{G_\infty} = \frac{\frac{\delta}{k_B T}}{2\sinh\left(\frac{\delta}{k_B T}\right)} \approx \frac{1}{2}\cosh^{-2}\left(\frac{\delta}{2.5 k_B T}\right) \tag{2.109}$$

where

$$\delta = e\frac{C_g}{C}|V_{g,res} - V_g| \tag{2.110}$$

where $V_{g,res}$ is the gate voltage at resonance. With equation 2.108, this allows the capacitance of the whole system to be found. The width of the peaks will remain linear as long as the thermal excitation energy is much less than that of the charging energy

Other techniques to probe the properties of QDs also exists, such as far infrared spectrscopy on QD arrays, which produces particular information, other than that produced by transport measurements, on plasma modes of the system.[80] Capaci-

tance measurements and spectroscopy however produce nearly identical informa-
tion as transport measurements, in both arrays[81] and single dots.[82]

3   Sample Nanofabrication

Fabrication of each chip, which contains up to 25 samples depending on chip size, was carried out at Royal Holloway's Center for Nanophysics and Nanofabrication. Given other users also require the use of the facilities on a day to day basis, each chip would take between one and two weeks to fabricate.

There are a total of ten stages of fabrication depending on substrate type, seven of which require lithography and then either acid etching or evaporation. One stage involving annealing. These seven above stages have an inherent success rate of approximately 90% per stage making the total operational success rate per sample at approximately 53%. The remaining two stages are relatively straightforward, these include substrate preparation and insulating layer coating.

The yield per fabrication stage increases by defining certain parameters more and more accurately with each attempt. Many issues were encountered with the annealing and the SET formation stage, but it is believed that these issues have been identified and on the whole, overcome.

The ten stages of fabrication were as follows: Substrate Preparation and cleaning, mesa formation, AuGe ohmic contact pads, Au log-period antenna formation, insulating layer coating, top log-period antenna formation, Au point contacts and gate formation and SET formation.

Stages of fabrication details, inherent problems with each stage and solutions are described in the following sections. It is worth noting at this point that fabrication parameters are heavily dependent on the equipment set up used and may not necessarily work for different equipment in different facilities.

3.1   Design

The design used for both the Single Quantum Well (SQW) and Double Quantum Well (DQW) detectors was the same. The Only difference being the etching depths required and the annealing times. The design was produced in Nanomaker. The Nanomaker software was also used to drive an SEM for any e-beam lithography.

Figure 3.1 shows the design used. The left image shows the whole design, in this
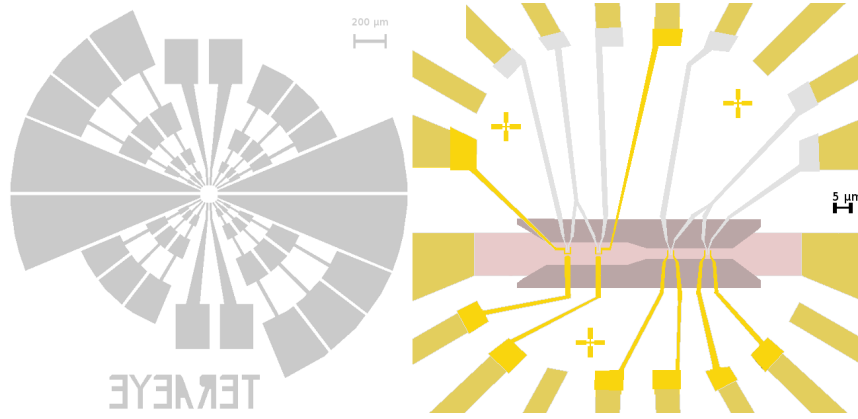
Figure 3.1: Schematic of Log period Antenna and zoomed in center displaying SETs and gates.

case illustrating mainly the antenna. The antenna is a circular log-period antenna design, with diameter 2 mm, this is active in the 0.2-2THz range, which is the region we are interested in. The antenna focuses the incoming radiation towards it center, where the QD are formed. The antenna is fabricated directly onto the surface of the AlGaAs/GaAs semiconductor. The antenna is made of 150nm of gold on top of 10nm of titanium.

The right hand image displays the components of the sensors centred in the antenna in a $85\mu m$ diameter space. The dark gold components correspond to the center parts of the log-period antenna. The pink layer indicates the mesa that is etched into the semiconductor substrate, and the dark purple layer indicated the fine mesa. The bright gold paths indicate the gold gates used to isolate the QDs and used as point contacts where needed. Along with these are three cross structures, used to align the aluminium pathways which are the SETs. These are fabricated directly above the QDs and within the gold QDs.

The mesa is initially defined as $10\mu m$ in width. This is then etched to define two different widths, $6\mu m$ and $2.5\mu m$. The gold gates are approximately $1\mu m$ across and form QDs of a similar size. QD gates and PC gates are separated by approximately 300nm. The overall SET structures are approximately $500nm$ wide when formed and have an overlap/oxide area of $0.1 \times 0.1\mu m^2$. A more detailed representation of the two designs of QD gates and SETs formed in them can be see in figure 3.2.

The samples were fabricated on SQW or DQW AlGaAs/GaAs heterostructures.
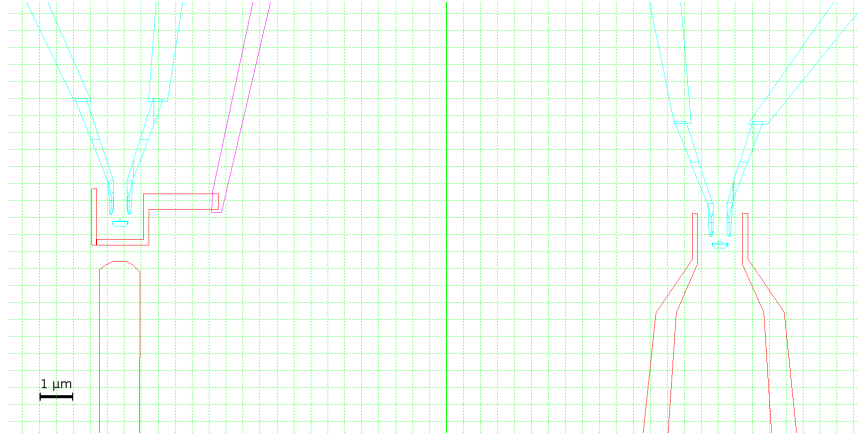
Figure 3.2: Design schematic of the QD gates and SETs used on sample. The red structures indicate the QD gates and PC structures. The blue structures represent the SETs.

The SQW substrates had the 2DEG layer located approximately 100nm below the surface, and the DQW substrate had 2DEGs located approximately at 100nm and 260nm as can be seen in figure 2.12 in section 2.2.2.1. The single quantum well heterostructure, which was supplied by Tokyo University has an electron concentration of $n = 1.6 \times 10^{11} cm^{-2}$ and mobility of $\mu \sim 6 \times 10^5 cm/Vs$ measured at 4.2K.[83] The DQW was supplied by Tokyo University, courtesy of Xpert Semiconductor, had the following values when measured at 4.2K; the top 2DEG has an electron concentration of $n = 3.2 \times 10^{11} cm^{-2}$ and mobility of $\mu \sim 11 \times 10^4 cm/Vs$. The bottom 2DEG has an electron concentration of $n = 4.4 \times 10^{11} cm^{-2}$ and mobility of $\mu \sim 12.8 \times 10^4 cm/Vs$.[84]

3.2   Substrate Preparation and Cleaning

Depending on the size of wafer available the substrate was cut using a diamond tipped etcher to the required size. Samples were usually made in batches with 9, 16 or 25 structures a sample, with samples measuring between 7mm^2 and 15mm^2. Samples were then thoroughly cleaned with acetone in an ultrasonic bath, 1165 Microposit remover in an ultrasonic bath and finally rinsed in isopropanol and dried in nitrogen gas. Cleaning times were dependent on the quality of the surface. Times of approximately five minutes were regularly used however.

Some problems arose at this stage where it could be seen that the sample was particularly hydrophobic making resist spinning near impossible. This was later found to be due to an organic surface layer. In some cases this was removable using

a light oxygen plasma etch, however, this is undesirable with a 2DEG being only 100nm down in the both heterostructures.

3.3   Fabrication of Mesa Pattern with Optical Lithography

Positive photoresist, S1813, was spun to a thickness of approximately 1.1μm on the sample. It was then baked at 90°C for five minutes. Using a UV optical contact aligner (200W, Intensity of 10 mW/cm^2 and wavelength 405nm ±6%), a mask image of the mesa was then exposed onto the resist for 15 seconds. Samples were then developed in MF319 developer for 50 seconds and washed in de-ionised water.

This resist image on the samples acts as a mask for acid etching. Etching times are dependent on the wafer used to start with but take between eight and ten minutes. H_3PO_4:H_2O_2:H_2O (ratio. 4:1:90) was used to etch the material away. First, however, the height gap between substrate and resist was measured using a profiler. Acid etching was done in short bursts of time, with profiling in between, to achieve the correct etch depth. Etch depths of 90-100nm or 285-300nm were achieved. Wet etching was used rather than plasma to avoid damaging the 2DEG layer(s).

Care was needed when developing the samples, prolonged development weakened the resist, which would then allow the acid to etch under the pattern, damaging the mesa. An example of a the patterned reist and a correctly formed final etched mesa can be seen in figure 3.3.
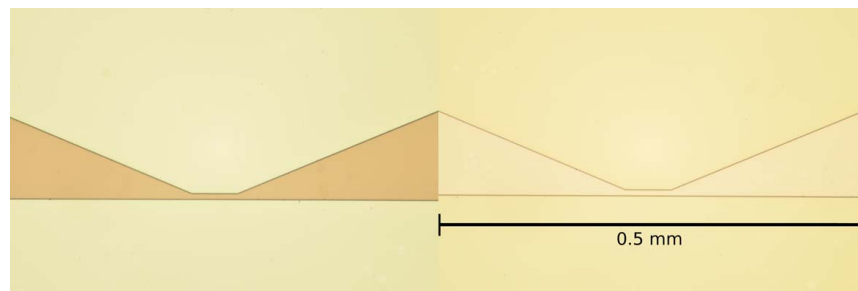

Figure 3.3: Left image showing resist pattern used as a mask for acid etching of substrate. A formed mesa can be seen in the right hand picture. The narrowest part of the mesa that be seen is $10\mu m$ wide.

3.4   Fabrication of Ohmic AuGe Contacts

For good conductivity from the mesa extremities to the structure built on top, an Gold Germanium (AuGe) layer was first deposited, which was later annealed. The layer was formed using photolithography. An undercut layer of LOR-5B was first spun to a thickness of 0.3μm and baked for five minutes at 150°C. A top mask layer of S1813 was then spun on top to a thickness of 1.1μm and baked for five minutes at 90°C.

The resist was then exposed for 15 seconds in UV light (200W, Intensity of 10 mW/cm^2 and wavelength 405nm ±6%) with the desired mask pattern in an aligner. The exposed design was then developed in MF319 developer for 20 seconds. However pattern development was first checked after 15 seconds to ensure correct development. Samples are subsequently washed in de-ionised water. An extra process was then carried out; Samples are submerged in 10% HCl solution for 12 seconds for two reasons: cleaning of the surface and bond breaking of the surface layer of the mesa to allow better adhesion to the evaporated layer. A developed sample can be seen on the left in figure 3.4.

Evaporation is carried out at a pressure of approximately $5 \times 10^{-6} torr$. An adhesion layer of Nickel Chromium (NiCr), 99.9% purity, was first evaporated to a 5nm thickness, followed by a AuGe, 99.95 % purity, layer of 200nm. Both evaporations were carried out with no break in vacuum. This was to avoid bad contact-forming with the NiCr layer after being exposed to atmospheric pressure. Lift-off was then carried out using MR1165 at 60°C for 20 minutes to an hour as needed.

To complete this stage and ensure good electrical contact with the mesa, the sample was annealed to aid diffusion of the Ge into the mesa layer. Annealing was carried out in an argon atmosphere at a pressure of approximately $2 \times 10^{-5} torr$. Samples were placed on a calibrated tungsten boat. A current of 27A corresponding to a temperature of $400 - 450$°C, was passed through the boat for one minute and 45 seconds. A custom built annealing boat was calibrated and used for the process, further information can be found in appendix C. A successfully annealed sample can be seen on the right in figure 3.4. Careful temperature control was found to

be needed, as too low a temperature would not cause the Ge to diffuse into the substrate correctly, and too high a temperature would cause the Ge to become too diffuse, and/or the sample could become "baked".
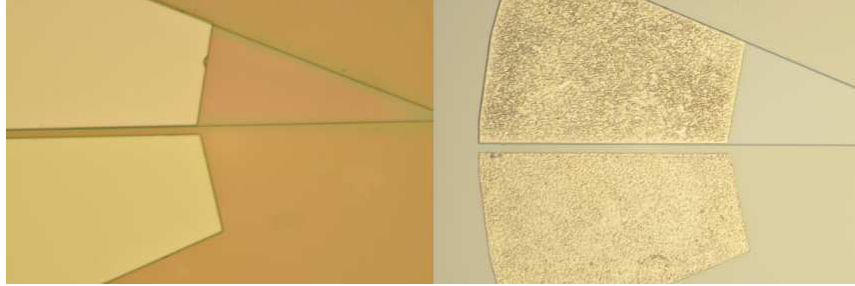
Figure 3.4: Left image is of the AuGe pattern formed by the developed resist. Right pattern is of the pads after the annealing process.

Some difficulties occurred at the annealing and evaporating stages. With the annealing special care had to be taken to ensure the whole sample was in contact with the boat and not hanging over the edge, as to ensure isotropic annealing. Slightly extra current, over 29A, also caused the boat to become too hot causing excessive annealing in the samples. The amount of AuGe was varied until the correct amount needed to reach the 2DEG layers was found. NiCr was also found to be an aider in the ohmic contact formation.

Errors in evaporation were purely mechanical in error, such as the NiCr source running out of material. If this occurred and the sample needed to be exposed to the atmosphere before the entire process was finished another smaller layer of NiCr (10nm) would need to be evaporated before AuGe (or further AuGe) could be evaporated onto the sample. This correction technique did not work every time however.

Further issues occurred during the processing of the DQW. As the bottom layer was much deeper than the with the SQW case, it was originally thought that a longer annealing time may be required. This however turned out to be detrimental to the sample, as the Ge appeared to become to dispersed within the semiconductor substrate. It was later found that a thicker layer of AuGe aided ohmic contact formation. Occasionally thickness in the order of 250nm were used successfully.

In future development, the use of a dedicated annealing oven would be of a great advantage.

After annealing, the resistance across the mesa was measured using a probe station to ensure proper ohmic connection. For the SQW heterostructures, mesa resistance in the order of $500 - 5000\Omega$ was expected. For the DQW heterostructures mesa resistance in the order of $5000 - 50000\Omega$ was expected. If unsure further test was carried out. The Sample would have its mesa resistance taken while in liquid nitrogen at 77K. In some cases it was found that the above resistances were found, but when cooled to below 4K the conduction channel became frozen out and zero conduction across the mesa occurred. This was due to insufficient/failed annealing causing improper ohmic contacts to be formed. Testing at 77K became a good indication of whether a sample would work at below 4K.

A possible improvement in the ohmic contact formation for the DQW substrate is illustrated in figure 3.5. Here we can see the pad at each end of the mesa is divided into two areas. One area would then be etched down to below the first 2DEG, but still above the second. Individual channels would then be etched into the pads to a depth below the 2DEGs. Material would then be evaporated onto the whole pad to a thickness that would avoid shorting between the separate areas, as indicated in the figure. After annealing, material would have a direct ohmic contact with the 2DEGs, while also maintaining individual control of each 2DEG. The annealing process may also require less time and heat, therefore avoiding damage to the 2DEGs. This would however add extra fabrication steps to the overall process, and require the fabrication of a new photolithography mask.

One other anomaly that presented it self while developing the ohmic contacts, was leakage on non mesa annealed pads. The photomask used required that some non-mesa pads had to have AuGe deposited, and annealed. This did cause problems later on in testing with leakage between the mesa and pads that were connected to a gate or SET. This can be rectified by changing the photomask to having only the mesa pads annealed.
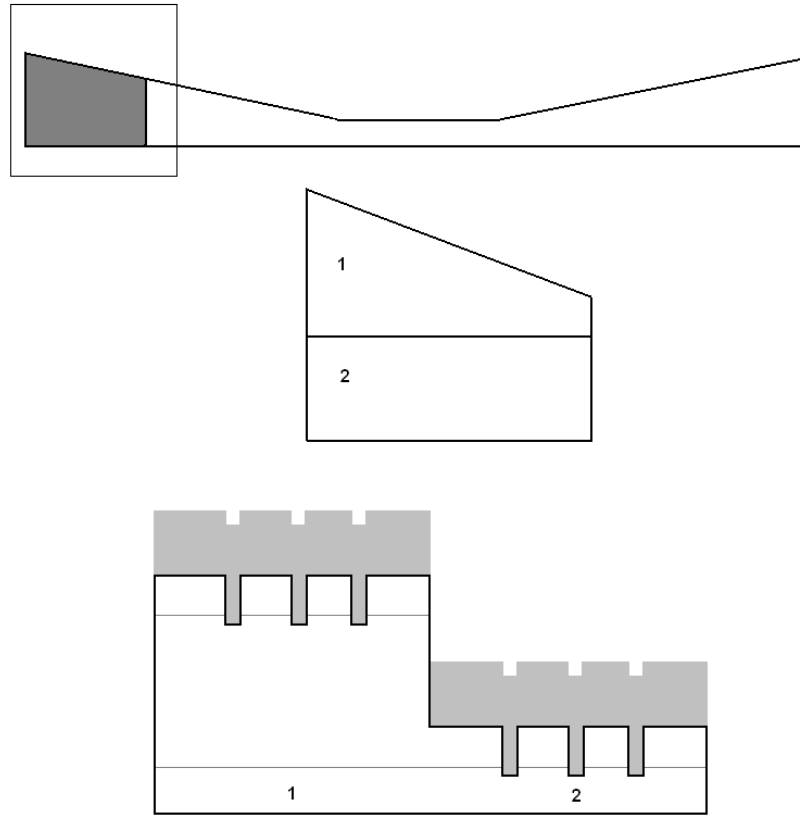
Figure 3.5: Potential AuGe Ohmic pad formation. Top two images indicate which area of the pad will be used for the ohmic contact formation. Middle image indicates how each pad is divided into two separate areas. Bottom images shows a transverse view of a pad. This indicates how the substrate is etched and how the AuGe (grey shading) will be deposited the substrate.

3.5 Metallisation with Planar Log-Periodic Antenna

The next stage of photolithography was carried out to form the final Au antenna structure at the centre of which the QD, gates and SETs will be formed.

A layer of LOR-5B was spun to a thickness of 0.3μm and baked at 150°C for five minutes, followed by a layer of S1813 spun to a thickness of 1.1μm and then baked at 90°C for five minutes. The desired mask structure was exposed onto the resist for 15 seconds in UV light (200W, Intensity of 10 mW/cm^2 and wavelength 405nm ±6%) in an optical aligner. The sample was subsequently developed in MF319 developer for 45 seconds. The sample was first checked at ten seconds to ensure correct development. The sample was then washed in de-ionised water.

Evaporation was carried out at a pressure of $3 \times 10^{-6} torr$. Two evaporations were

carried out in the same process. First an adhesion layer of 15nm Titanium, 99.99% purity, (Ti) was evaporated followed by an Au layer, 99.999% purity, of 110nm. Lift-off was then carried out using MR1165 at 60°C for between 20 minutes to one hour as needed. Titanium was used, as during evaporation it adsorbs surrounding gas, know as a "Titanium Flash", bringing the pressure down allowing better quality films to be formed.
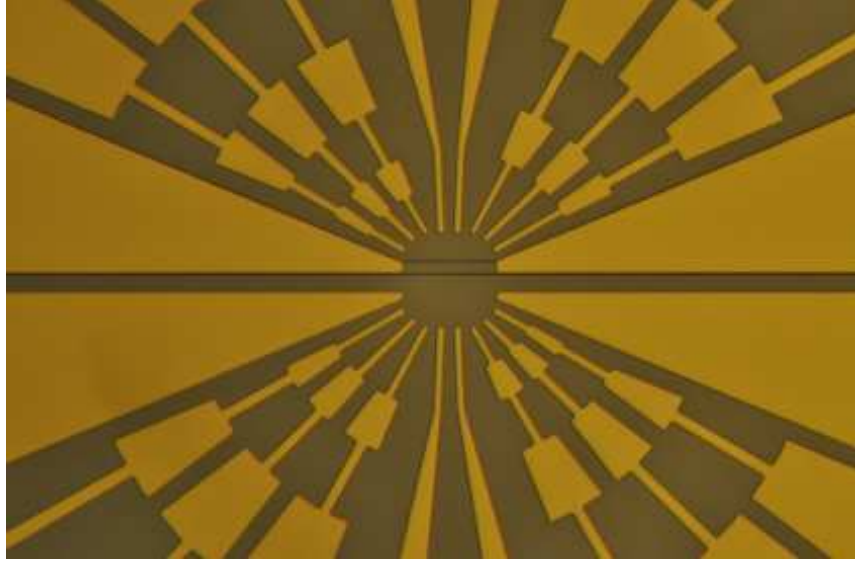
Figure 3.6: Successfully formed Au log period antenna.

A successfully formed log-period antenna can be seen in figure 3.6. No problems were encountered at this stage.

3.6   Fabrication of Mesa Pattern with Electron-beam Lithography

The mesa was wet etched further forming a fine mesa from which the QDs would be formed with the QD gates. This was achieved by forming a mask using resist allowing the acid to only etch the desired sections.

4% PMMA was spun to a thickness of 1.8μm on the sample and then baked at 170°C for ten minutes. Lithography was done using electron beam technology at a dosage of 225$\mu C/cm^2$. The pattern was developed using H$_2$O:IPA (7:93) for 20 seconds and rinsed in IPA.

The mesa was etched through the mask using H$_3$PO$_4$:H$_2$O$_2$:H$_2$O (4:1:90) until a

depth of 80-100nm or 285-300nm was achieved. This was done by first placing a small scratch on the sample in a non desired area. This scratch was then profiled and the depth measured. The scratch should go through the resist to the substrate so when introduced to the acid it can be used as a gauge of how deep the etch has occurred. The sample was etched in the acid for 30 seconds at a time. Once the desired depth was achieved the resist was removed by washing the sample in acetone at 50°C. Etch times of up to nine minutes were used. Figure 3.7 shows the resist pattern before etching and the resulting fine mesa when completed. Note the width of the finished mesa being slightly smaller than that of the resist pattern, this is due to the acid etching horizontally across as well and down.

Figure 3.7: Left image is of the resist pattern formed using e-beam lithography prior to acid etching. The right image is of the mesa etched and resist removed.

Many problems arose at this stage with the etching. On numerous occasions it appeared that the mesa was not etching at all, or at least inconsistently. To try and add consistency, the acid used was stored in a fridge at a fixed temperature, 7^0C, and each time the acid was required, a fresh batch was used. This was thought to be mainly due to either the substrate or remaining resist. As an initial etch would have already been successful from forming the mesa, it was narrowed down to remaining resist. However, coupled to this issue, there was the problem of profiling the scratch. As it was difficult to get a perfectly uniform scratch, the position at which the scratch was profiled was very important, otherwise inconsistent recorded depths occurred. This was overcome by forming the scratch near an alignment mark, such as an alignment cross.

It was also later thought, that the etching times changed each time, due to a layer of oxide forming between etches. This causes the acid to take longer etching the oxide away first, before etching the mesa itself. This was overcome by carefully

adjusting the etching times as needed.

For deeper etches, such as in the DQW case, it was noted that the substrate did not etch straight down normal to the surface. It was found that depending on the crystal orientation on the substrate, the substrate would taper either outwards or inwards as it etched downwards. This issue was overcome by adjusting the pattern spacing of the fine mesa to obtain the desired results. The taper also ended up being an advantage, as it allowed the Au gates and Al SETs to have a slope, rather than a vertical step from the substrate to the top of the mesa. Although the polyimide also helped spline out such contours.

The final difficulty that presented itself at this stage was the non isotropic etching across the chip. The centre of the chip would etch faster than the edges of the chip, this was not something that was easily overcome and a tolerance of etch depth of between 80-100nm or 285-300nm was acceptable.

3.7   Insulated Layer Coating

An insulating layer of T-11 from Sci Brewer Inc. polyimide was used which had a permittivity of $\varepsilon \sim 3$. The sample was first washed in Bond Brewer APX-K1 for one minute. This is used to break surface bonds enabling good adhesion for the polyimide layer. The polyimide was spun onto the sample at 6000rpm achieving a thickness of approximately 200nm. This was baked at a temperature of 170°C for 10 minutes. A 1.1μm layer of photo resist S1813 was then spun on top and backed at 90°C for five minutes. The S1813 was exposed to UV light (200W, Intensity of 10 mW/cm^2 and wavelength 405nm $\pm6\%$) using the same pattern as the Au planar circular log-period antenna with an aligner. MF319 was then used to develop the resist for 40 seconds, followed by a 30 second rinse in water. The polyimide was etched away leaving the desired shape through the photoresist pattern. This was done using a plasma etch of 100% O_2 for five to eight minutes.

As well as adding an insulating layer, the polyimide had the advantage of splining out any large steps on the sample, essentially smoothing the surface of the substrate, ready for the Au gates and Al SETs.

A few concerns occurred at this stage with achieving the correct alignment of the polyimide with the already present structure. This was overcome through practise. Figure 3.8 shows a sample successfully coated in polyimide.
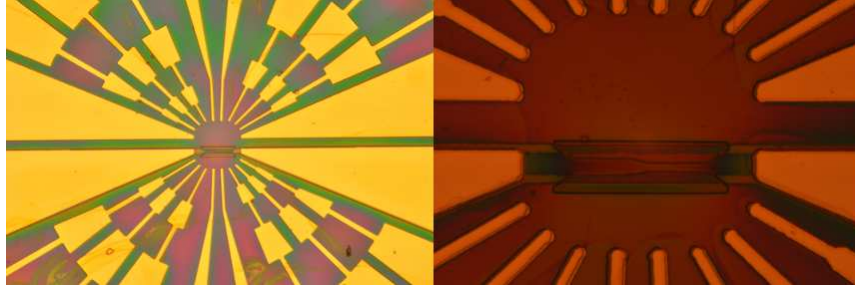
Figure 3.8: Sample successfully coated in polyimide. Note the very small misalignment between the gold paths and polyimide coating. This discretion however does not cause any significant issues.

The sample was then baked for a further ten minutes at 230°C to cure the poly-imide. If this process was not done, problems with the polyimide being dissolved by acetone or 1165 in later steps were encountered.

3.8   Top Layer Metallisation

Some conduction problems were encountered with the gold and aluminium paths connecting to the log period antenna properly. It was thought that this may be caused due to the polyimide not being completely removed, however further plasma etching was wanted to be avoided. To overcome this and ensure a good ohmic connection, another log period antenna was deposited on top of the polyimide.

The same process and parameters as described in section 3.5 was used.

3.9   Fabrication of Metal Gates with Electron-beam Lithography

The QD gates and point contacts were formed using electron beam lithography. Both structures are formed simultaneously in the evaporation stage.

A layer of copolymer 6% was spun to a thickness of 0.5μm and baked at 160°C for ten minutes, followed by a layer of 2% PMMA spun to a thickness of 0.25μm and then baked at 160°C for ten minutes. Lithography was done using electron E-beam

technology at a dosage of $225\mu C/cm^2$. The pattern was developed using Tol:IPA (1:5) for 15 seconds and then ECA:Eth(1:5) for 15 seconds and rinsed in IPA.

A 20nm Ti, 99.99% purity sticking layer was then evaporated and a 130nm of gold, 99.999% purity, was then evaporated onto the developed sample, evaporation pressure used was $5 \times 10^{-7} torr$. Acetone was used for lift-off to dissolve the resist at 60°C. The sample could only be placed in the acetone for three minutes as the acetone would start to attack the polyimide layer after this time. Examples if well formed QD gates and PC gates can be seen in figure 3.9.
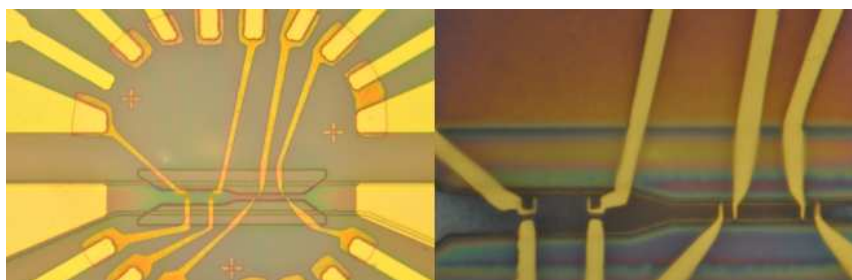
Figure 3.9: Examples of well formed QD and PC gates. Note the slight over development in right hand example. This however does not effect operation of the sensor. Examples shown are from two different samples. A connection between two paths can be seen in the top right of the left image. This was done to ensure conduction from photolithography pathways to the e-beam pathways.

Very few problems occurred at this stage. Only on one or two occasions did lift-off fail. If lift-off was not clean, a full 2 litre, 70 watt, 40KHz ultrasonic bath at room temperature was used as necessary to careful remove any reminding material.

3.10 Fabrication of Al Single Electron Transistors

Single Electron Transistors (SETs) were formed using e-beam lithography and shadow evaporation techniques utilising a self aligning pattern, as is shown in figure 3.2.

A layer of copolymer 14% was spun to a thickness of $0.7\mu m$ and baked at 160°C for ten minutes, followed by a layer of 2% PMMA spun to a thickness of $0.25\mu m$ and then baked at 160°C for ten minutes. Lithography was done using electron e-beam technology at a dosage of $225\mu C/cm^2$. The pattern was developed using Tol:IPA (1:5) for ten seconds and then ECA:Eth (1:5) for 40 seconds and rinsed in IPA. Times were varied is required to obtain the desired development. Reasons for change in time included length of time between the sample being exposed and developed and

slightly varying developer concentrations.

Aluminium, 99.999% purity, evaporation was carried out at pressure of approximately $3x10^{-6}torr$. A collimator and shadow evaporation techniques were used to form the SET structures. The first evaporation angle used was 13° from the normal and 35nm of aluminium was deposited.

The next stage was to oxidise the aluminium in preparation of forming the tunnel junctions. Oxidation occurred in a 100% (excluding trace gasses) oxygen environment at a pressure of 30 mtorr for eight minutes.

The final evaporation was then carried out at −13° from the normal with 35nm of aluminium deposited. Acetone at 60°C was used for lift. As before the sample could only be placed in the acetone for no more than three minutes so as not to dissolve the polyimide. Examples of the developed resist pattern and finished SETs can be seen in figure
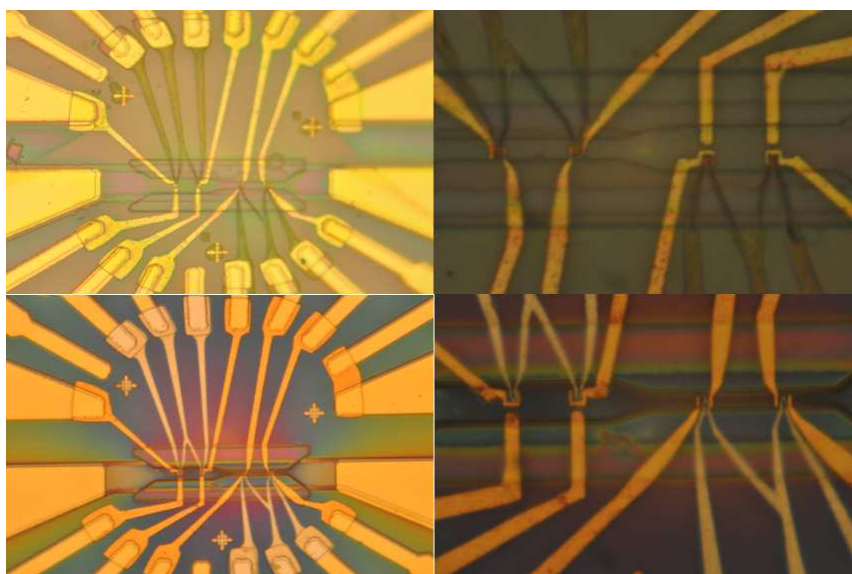
Figure 3.10: Top pictures show developed SET and SET pathways. Bottom pictures show final finished sample with properly formed SETs.

Numerous problems occurred at this stage, mainly to do with the oxidation time and pressures. Although different samples may be treated exactly the same, different resistance tunnel junctions were recorded. The resistances varied dramatically, from basically being short circuited to infinity. It is believed that this variation in pressure occurs due to time taken to stabilise the pressure of incoming oxygen gas, which required manual adjustment.

3.11 Preliminary Testing

Once fabrication was completed, preliminary resistance measurements of the mesa, Au pathways and SETs at room temperature were done on a probe station. Extra care with handling and static discharge now the SETs had been formed. Mesa resistance were confirmed to match those recorded in section 3.4. The resistance across the shorting pad noted in figure 3.9 is measured to ensure ohmic contact between the larger antenna structure and the Au and Al pathways, and a value in the order of $100 - 1000\Omega$ is expected.

The normal resistance of the SETs at room temperature was also recorded. High resistance SETs were considered to have a vale in the order of hundreds of kilohms and low resistance SETs were considered to have a normal resistance in the order of tens of kilohms. Many SETs were found to be short circuited or have infinite resistance however, indicating the oxidating process in section 3.10 had failed. It was found that the lower the resistance (while still being properly formed) gave a lower charging energy of the SET as was expected.

3.12 Sample Package Mounting

When it was believed that a working sample had been produced, it was then attached to a 16 pin chip package using silver conducting adhesive. The sample was then connected to the legs of the chip package by bonding the sample to the package pads. $25\mu m$ aluminium wire was used with a wedge bonder to complete this task. The wedge bonder uses both heat and ultrasonic pulse to attach the wire to the pads. Careful selection of the power and duration of the ultrasonic pulse was required, as if it was too strong, it may rip the Au antenna pads off the sample. A finished sample can be seen in figure 3.11.
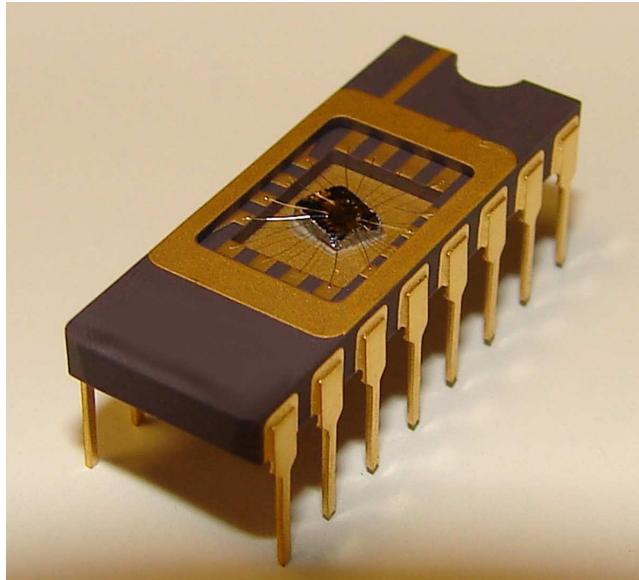
Figure 3.11: Completed and mounted sample. The silver conducting adhesive can be seen under the chip in the centre of the package. The aluminium bonding wires are also visible.

4 Experimental Techniques

This section will outline the techniques used for refrigeration and measurement of the fabricated devices. Devices fabricated were measured in a 0.3K Heliox ^4He/^3He system and measurements were taken using a custom built amplifier coupled with a LabView controlled computer measurement system incorporating a lock-in amplifier. For operation with the point contacts, temperatures as high as 1.5K can be used. For accurate and successful SET operation, temperatures bellow the superconducting transition temperature of aluminium of 1.175K needed to have been used. To improve operation though, lower temperatures in the area of 0.3K were used.

4.1   Low Temperature Techniques at 0.3-4.2K.

Temperatures around 4K can easily be achieved with liquid ^4He as a direct refrigerant, which can then be pumped as to achieve evaporative cooling. Achieving temperatures below 1K however requires ^3He cooling.

This is accomplished by first liquifying the ^3He in the sample space with ^4He cooling methods via a 1K pot. The ^3He is then pumped using a zeolite sorb. The sorb is first heated to 40K to remove any absorbed gas and allow it to become liquified. Upon cooling, the ^3He is adsorbed to the surface of the sorb, causing evaporative cooling to occur, which allows temperatures of 0.3K to be achieved. A schematic of the full system can be seen in figure 4.1.
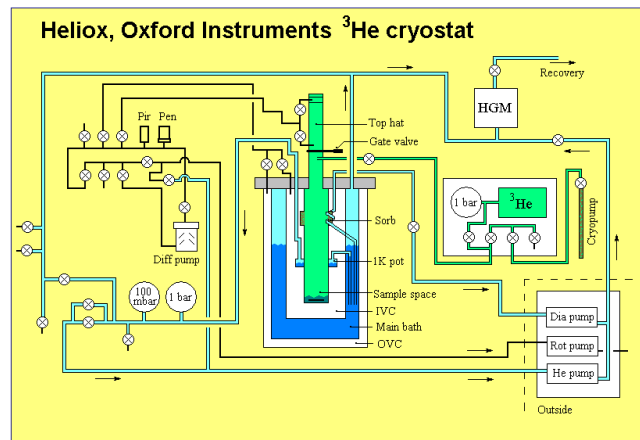

Figure 4.1: ^3He/^4He Heliox cryostat schematic. [85]

The sub 1K cooling techniques utilising ^3He used here can be described using the

Clausius-Clapeyron[86, 87] equation

$$\frac{dp}{dT} = \frac{L}{T\Delta V} \tag{4.1}$$

where p is the pressure, T the temperature, ΔV the change in volume during the phases transition and L the latent heat of evaporation per mole. V can be substituted however using the ideal gas equation, equation 4.2, leading to equation 4.3.

$$Pv = nRT \tag{4.2}$$

Where P is the pressure, v the volume, n the amount of substance in moles, R the gas constant and T is the temperature, to give

$$\frac{dp}{dT} = \frac{L}{RT^2}p \tag{4.3}$$

Assuming that the heat leak L is constant, we can integrate the equation to obtain the following solution

$$p(T) = p_0 e^{\frac{-L}{RT}} \tag{4.4}$$

Where we can see that the temperature achievable by reducing the pressure, or pumping the system, is dependent on the heat leak as one would expect. As such the lowest possible temperature that can be achieved occurs when the cooling power equals the heat leak. As the latent heat values of ^3He and ^4He differ, the difference in vapour pressure also is different, with ^3He having a vapour pressure approximately 1000 times larger at 0.5K. This means that through pumping alone, using ^4He can achieve temperature of approximately 1K and using ^3He can achieve temperatures of approximately 0.25-0.30K. Hence the use of a two stage system, using the ^4He to condense the ^3He first.

The system outlined in figure 4.1 can achieve temperatures of approximately 0.25K in approximately one to two hours from loading using the loading chamber and probe. The probe enters the sample space where ^3He is condensed by ^4He from the surrounding bath and 1K pot. The ^3He is then pumped using the sorb, which

can continue pumping the ^3He before becoming saturated and requiring heating for approximately 45 minutes. This gives a hold time of approximately 50 hours. The cryostat is also fitted with a four tesla magnet, which was used for Hall resistance measurements of the 2DEGs. The probe is also fitted with a black body emitter (a 2.5KΩ surface mount resistor) and a light pipe, for either transmitting or emitting terahertz radiation onto the sample. If the black body emitter is being used, the hold time is decreased to the thermal excitation to the sample space caused by the emitter from heating.

When the sorb becomes saturated, it is heated to 45°C for 45 minutes to liberate the adsorbed ^3He from the zeolite crystals. This is then caught in the helium dump vessel ready for re-condensing. The ^3He system is a sealed system, so very little ^3He is lost due to normal operation.

In the system used here, the sample space is reached via a probe, which is used to save loading times. Samples may be loaded in approximately 5 hours, opposed to 2-3 days if heating up and cooling down the whole system. The probe itself has isolation plates between the sample holder and the rest of the probe, as to avoid thermal contact with the outside world. It does however have 16 x 0.15mm constantan wires and a 2mm steel light pipe leading to the sample space which would have introduced an extra thermal load. Approximately half way along the probe, in a thermally insulated area and optically connected to the light pipe, is a metal cup section in which we situate our terahertz emitting sources. The emitters used produce a black body radiation. A full description of the optical system can be found in section 4.2.

The emitter was placed 50cm away from the sample and behind several insulated baffles, and a light pipe was used to transmit the radiation. The sample space itself is in direct thermal contact to the cold plate at the bottom of the ^3He space, which is also where the temperature sensor for the system is mounted. It was noted that only on experiments where the emitter was placed actually in the sample space next to the sample itself that the temperature would then change. This leads us to believe that the temperature reading given by the temperature sensor is indeed a good reading of the temperature of the sample.

In alternate setups, two extra 0.15mm wires have been thread down the light pipe to the sample space, and used to connect to a black body emitter in much closer proximity than using the light pipe setup. This setup however does increase the base temperature dramatically, although point contact operation is still possible.

4.2   Terahertz Emitter and Optical System

A simplified view of the light pipe setup in the cryostat used can be seen in figure 4.2.
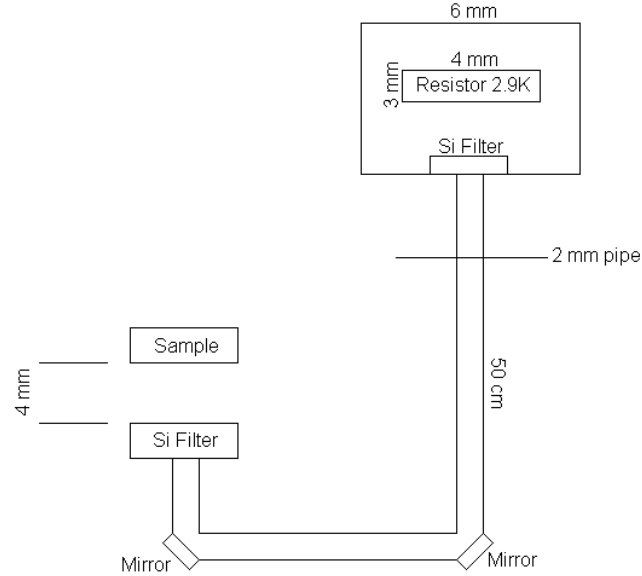
Figure 4.2: Schematic layout of light pipe used to produce and transmit terahertz radiation to samples with in the cryostat used.

As can be seen, a $2.9K\Omega$ resistor was used as a black body source within a 6mm diameter cylindrical enclosure. The 2mm diameter, 50cm long light pipe acts as a large wavelength cut off, a black polyethene filter is used to remove the infrared element of the black body radiation while the silicon filter removes all the shorter wavelengths of radiation. This can be seen in figures 4.3 and 4.4. There is a notable absorption band starting at approximately 3-4THz in silicon, however as the sensors are designed to operate in the 0.2-2THz region, this does not cause a problem in operation.

We define the Noise Equivalent Power (NEP) as

$$\text{NEP} = \frac{\text{Noise Voltage Per Unit } \sqrt{\text{Bandwidth}} \ [V/\sqrt{Hz}]}{\text{Responsivity}[V/W]} \tag{4.5}$$

where

$$\text{Responsivity}[V/W] = \frac{\text{Photoresponse}[V]}{\text{Power}[W]} \tag{4.6}$$

79
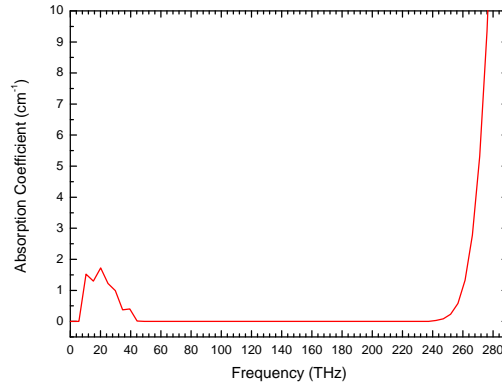
Figure 4.3: Absorption spectra of silicon in the terahertz/infrared region of the electromagnetic spectrum.[88, 89]
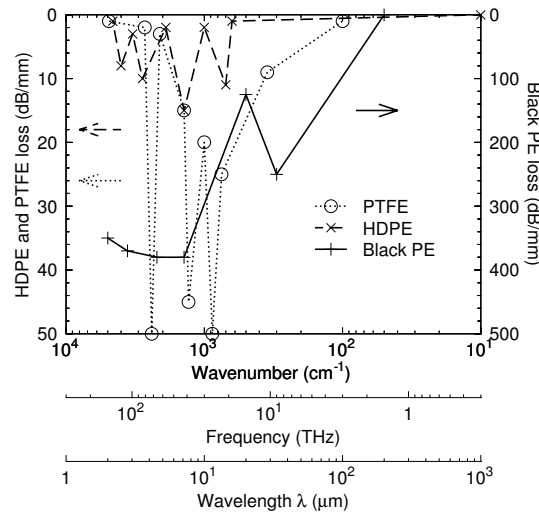
Figure 4.4: Absorption spectra of black polyethene in the infrared region of the electromagnetic spectrum.[90]

Where we can define the photoresponse in the experiment as the product of the peak current through the PC under radiation and the PC resistance.

$$\text{Photoresponse} = I_{Photosignal}R_{PC}[V] \tag{4.7}$$

We may also express the noise voltage per unit root bandwidth as below. We assume the measurement setup operates at 1000Hz.

$$\text{Noise Voltage Per Unit } \sqrt{\text{Bandwidth}} = \frac{I_{Dark}R_{PC}}{\sqrt{1000}} \frac{V}{\sqrt{Hz}} \tag{4.8}$$

We may now define the NEP as follows by substituting equations 4.6 and 4.8 into equation 4.5

$$\text{NEP} = \frac{I_{Dark}\text{Power}}{I_{Photosignal}\sqrt{1000}}\frac{W}{\sqrt{Hz}} \tag{4.9}$$

From experimental data, with the emitter operating at an electrical power of $3.6mW$, we have found a ratio for $\frac{I_{Dark}}{I_{Photosignal}} = 0.1$, therefore our NEP can be defined as

$$\text{NEP} = 3.2 \times 10^{-3}\text{Power}\frac{W}{\sqrt{Hz}} \tag{4.10}$$

We now need to calculate the power that reaches the sample space in the terahertz domain of 0.2-2THz. Power emitted by a black body in a given domain of $v_0[cm^{-1}] - v_1[cm^{-1}]$ can be found using Planck's law

$$\text{Power} = S_{em}K\int_{v_0}^{v_1}\frac{2\pi hc^2v^3}{e^{hcv/kT} - 1}dv \tag{4.11}$$

where S_{em} is the surface area of the resistor, K is the transmission coefficient of the system and T is the temperature of the emitter. We also define v_0 and v_1 as follows

$$v_0 = \frac{1}{d_{lightpipe}} = \frac{1}{0.2cm} = 5cm^{-1} \tag{4.12}$$

and

$$v_1 = \frac{f}{c[cm/s]} = \frac{2 \times 10^{12}}{3 \times 10^{10}} = 67cm^{-1} \tag{4.13}$$

We assume the resistor to be a cylinder, however only half of it faces towards the light pipe, so we calculate the surface area of the resistor minus the ends and half the area

$$S_{em} = \frac{2\pi rl}{2} = 1.8 \times 10^{-1}cm^2 \tag{4.14}$$

As the emitter is positioned very close to the entrance of the light pipe, we can assume a planar wave entering the light pipe from the enclosure. To calculate K we calculate the ratio of radiation incident on the light pipe to the emitted radiation. We

do this by calculating the ratio of the area of the light pipe to the area of the enclosure facing the light pipe

$$\frac{\pi(d_{Lightpipe}/2)^2}{\pi(d_{Enclosure}/2)^2} = \frac{(2/2)^2}{(6/2)^2} = \frac{1}{9} \tag{4.15}$$

We also need to take into account the transmission through two Si filters. We assume the refractive index of silicon in this wavelength range to be $n = 3.42$.[89] We take the transmission across the boundary between vacuum and Si to be

$$T = 1 - \left(\frac{n-1}{n+1}\right)^2 = 0.70 \tag{4.16}$$

and as there are two filters, there will be four boundaries, giving a total transmission to be $(0.70)^4 \sim 0.24$.

We also need to consider the attenuation of the light pipe itself. For a 2mm stainless steel light pipe in the terahertz range, an attenuation of $5 - 10dB/m$ is assumed.[91] Taking the upper limit of $10dB/m$ therefore gives a total attenuation due to the light pipe of $\sim \frac{1}{3}$.

We must also consider the 4mm distance between the end of the light pipe and the sample its self. As the light pipe is in such close approximately to the sample, a plane wave may be assumed again. This means we can take the ratio of the area of the sample to the area of the face of the light pipe to be the fraction of transmitted radiation

$$\frac{\pi(0.5)^2}{\pi(1)^2} = \frac{1}{4} \tag{4.17}$$

We also estimate the mirrors illustrated in figure 4.2 to be not perfect, and combined have a 90% efficiency.

We may now define K to be

$$K = \frac{1}{9} \times (0.24) \times \left(\frac{1}{3}\right) \times \left(\frac{1}{4}\right) \times (0.90) = 2 \times 10^{-3} \tag{4.18}$$

We may now define the power and NEP to be

$$\begin{aligned}
\text{Power} &= S_{em}K2\pi hc^2 \int_5^{67} \frac{\nu^3}{e^{1.44\nu/T}-1}d\nu \\
&= 1.35 \times 10^{-15} \int_5^{67} \frac{\nu^3}{e^{1.44\nu/T}-1}d\nu
\end{aligned} \tag{4.19}$$

$$\text{NEP} = 4.32 \times 10^{-18} \int_5^{67} \frac{\nu^3}{e^{1.44\nu/T}-1}d\nu \tag{4.20}$$

The last piece of information required is to know the temperature of the emitter at the operating electrical power. A similar emitter (resistor) was measured in the same enclosure. Its electrical power was varied and its temperature measured, as can be seen in figure 4.5.
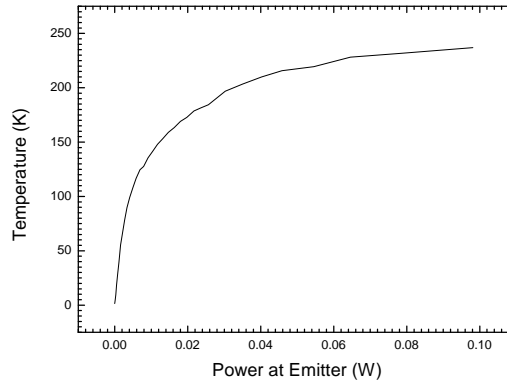
Figure 4.5: Temperature dependence of a Speer resistor at given electrical powers.[92]

From this we can see at an operating of power of 3.6mW, which was the initial power we first started using, we have an emitter temperature of 90K. This corresponds to an incident power of $5.53 \times 10^{-9}W$ and an NEP of $1.77 \times 10^{-11}\frac{W}{Hz^{1/2}}$. The maximum emitter power used was 34.4mW which equates to approximately 200K, giving an incident power of $1.56 \times 10^{-8}W$. The corresponding black body emitter intensities at 90K and 200K can be seen in figure 4.6. Using the Wien's displacement law, we can find the ideal black body temperature for the frequency range corresponding to 0.2-2THz to be 1.9-19K. However, as was found experimentally and as can be seen in figure 4.6, the intensity produced by the emitter was too low to produce sufficient incident power at the sensor to allow operation. Temperatures

above 200K were not also possible due to the warming affect of the emitter on the

cryostat.

Figure 4.6: Top graph illustrates the black body spectrum using Planck's Law at 90K and 200K. The bottom graph illustrates a zoomed in version, with the addition of Planck's law at 20K. The red dashed lines indicate the operating region of 02.-2THz.

4.3   Measurement Techniques

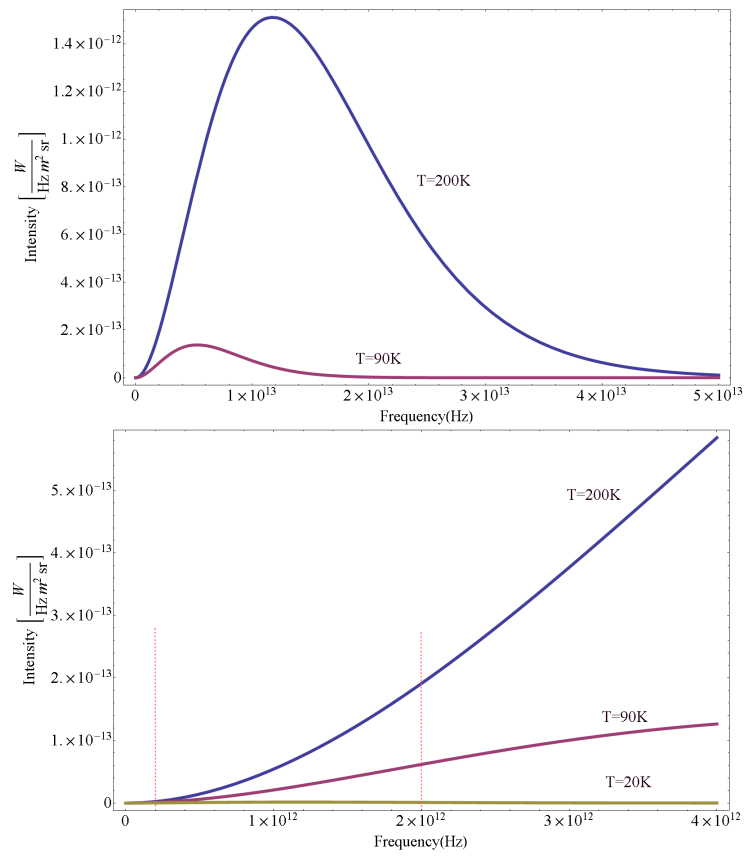A custom built amplifier was constructed and used for the testing and character-
isation of each part of a given terahertz sensor. They are mesa conductance, gate
voltage required for mesa conductance "pinch off", SET characterisation and pho-
toresponse. Depending the part being measured, a different measurement config-
uration was used: DC current measurement, the lock-in technique, and capacitive
measurements.

All data was recorded using custom written NI Labview software, and later anal-
ysed with further NI Labview software and programs such as Origin Lab Software.

4.3.1   Amplifier Design and Operation

Figure 4.7 shows the circuit design of the amplifier constructed. A voltage supply,
$\pm V_b$, is fed to the amplifier from a signal summator circuit and then goes through
a capacitor filter then a voltage divider, which reduces the voltage by a factor of 2,
20 or 200. This reduced voltage, $\pm V_o/2$ then passes through a selection of biased
resistors, where the corresponding bias resistors for $+V_b$ and $-V_b$ are always the
same value. The I+/V+ and I-/V- connection can then connect to the sample in either
a two or four point measurement configuration, depending on the sample design.
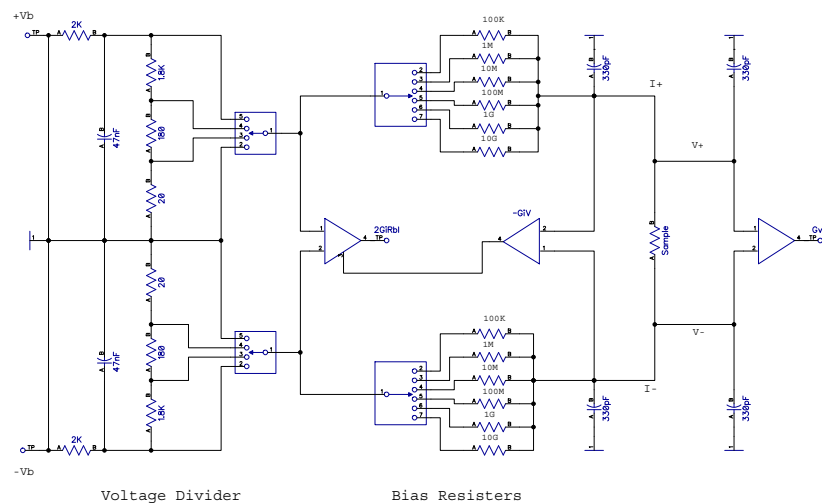

Figure 4.7: Amplifier design schematic as used in all measurements.

The voltage across the sample is simply measured directly using the instrumental

amplifier $G_v V$. The current measurement is done by measuring the symmetric bias voltage using an instrumental amplifier and then subtracting it from the original voltage V_O as read out by $-G_v V$ This is done by recording the negative voltage V_o and using it as an offset on the final instrumental amplifier. This calculation can be seen below.

$$V_{current} = G_i V_o - G_i V = G_i((2R_b I + V) - V) = G_i 2R_b I \qquad (4.21)$$

All connections up to the vacuum feed through connections on the probe are BNC 50Ω ground shielded cables to ensure no RF interference or excessive noise from external sources. Using this amplifier set up, currents in the nano-amp range were routinely measured.

4.3.2 I-V Characterisation of Mesa and SETs

Visual and analytical characterisation was done for the mesa and SETs of each sample. This was first done visually using an oscillating frequency bias to produce a I-V curve on an oscilloscope to visually inspect the characterisation. This was done by connecting the sample and corresponding structure (either SET or mesa) as described in figure 4.8.

This was particularly useful in testing the conduction of the mesa as the temperature of the sample was decreased. Poor annealing caused the mesa to stop conducting at low temperatures due to poor ohmic con, and this was easily seen.
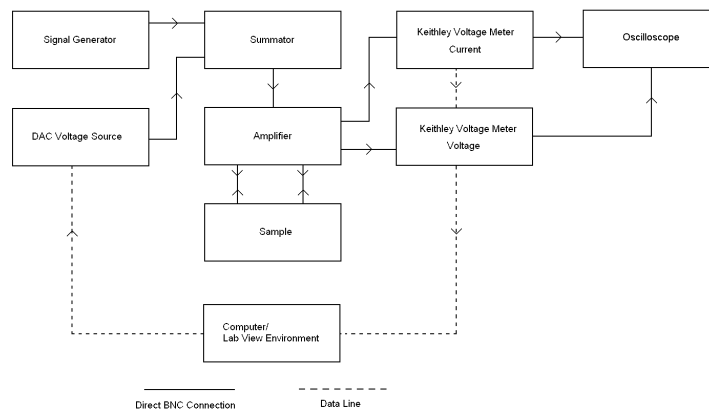
Figure 4.8: Equipment setup for I-V characterisation measurements.

4.3.3   Measurement of Pinch Off Value

Devices are at their most sensitive to terahertz detection when the conducting mesa channel has just been made non-conducting, or "pinched off". At this point, if an electron is excited out of the QD into the channel, the channel will go from non-conducting to conducting, which can then be detected.

This situation is setup using a point contact, which applies a negative electric field at 90° to the conducting channel. To find the pinch off points of each device, and therefore find its most sensitive area of operation, two dimensional scans were taken, where the point contact and QD gate are biased inturn to form a map of where the channel would and would not conduct.

For these measurements the equipment was set up as shown in figure 4.9.
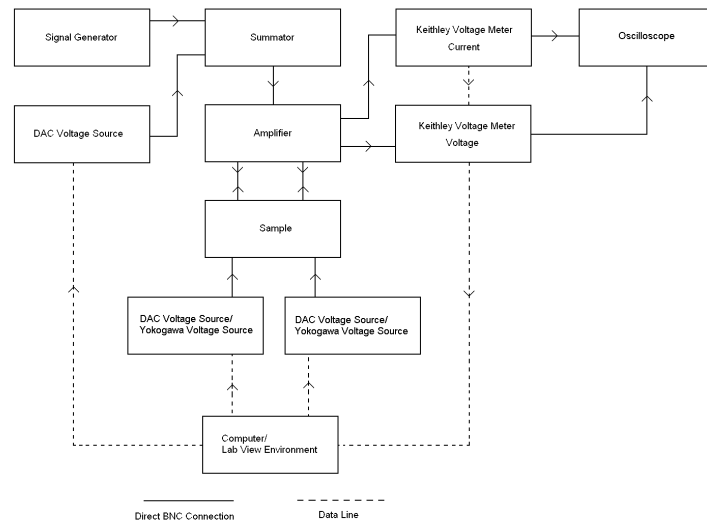
Figure 4.9: Equipment setup for mesa pinch off characterisation.

Low resolution scans comprising of 100 data points for the QD gate and 200 data points for the point contact were first used to find the area of interest. More high resolution scans of 250 points for the QD gate and 1000 points for the point contact were then taken, which would take approximately nine hours.

The two dimensional pinch of maps produced using this procedure, were invaluable in setting the device up ready for photoresponse measurements.

4.3.4   Measurement of Photoresponce by Counting of QD Excitation Events

To do measurements of the QD switching events we used a Tektronix TDS 3032 oscilloscope. The oscilloscope had a fast trigger ability compared to the Keithley 2000 multimeters and the NI Multifunction I/O NI PXI-6030E. The sample was biased to a point where the QD has just formed. The current across the SET was then recorded by the oscilloscope. The time traces of SET current were measured.

The equipment was set up so that the oscilloscope would transfer the contents of its memory buffer to the computer every time it became filled. The computer would then join the individual buffer downloads together to form one continuos trace.

The computer simultaneously would adjust any gate bias or emitter powers over time, as required. This allowed analysis of the switching events to be compared to different gate bias and emitter powers. From this measurement we may find a number of parameters, including number of switching events, integral count and mean value of the current.

The number of switching events is purely the number of peaks measured above a given threshold or "cut off" value. The integral count is however a more accurate measure of switching events. Rather than measuring peaks above a given threshold, it measures the length of the current curve in time. Hence a peak would have a longer length curve than a point on the graph that would not have a peak. The mean value of the current is averaged over the time at a given applied gate voltage.

We attempt to distinguish between random switching events caused due to thermal excitation and events caused by a photon excitation using these tools. We would expect a larger counting rate for photoexcitation than for random thermal events.

4.3.5   Measurement of Photoresponce Using the Lock-In Method

Photoresponce measurements were taken using the lock-in technique. The experimental setup can be seen in figure 4.12.

The lock in technique takes an AC reference input and a signal input that are both at the same frequency and produces an amplified DC output. The amplifier "locks-in" to this known frequency and ignores all other frequencies, massively reducing noise and other unwanted affects. Figure 4.10 illustrates the operation of the lock in amplifier.
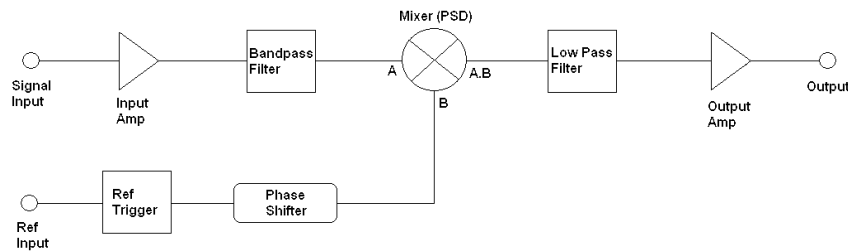
Figure 4.10: Lock-in Amplifier Operational Scheme.

The lock-in amplifier uses a phases sensitive detector (PSD) to demodulate the mixed signals into a DC output. This DC output is however still a function of the phases between the input and reference signals. This allows the lock in amplifier to also act as a relative phase detector between signals.

As an AC voltmeter does not discriminate between different frequencies, when the AC signal is demodulated, some of the demodulated noise components will also find there way into the DC signal. The lock-in amplifier however locks into a specific signal frequencies, so any noise found with in that frequency will be seen as an AC fluctuation within in the DC output signal. This can then simply be removed using a low pass filter.

The PSD operates by mixing the reference and input signal using the following type of system to produce the desired output. Let the input signal V_{in} equal

$$V_{in} = A \cos[\omega t] \tag{4.22}$$

where ω is the angular frequency. At the same time let the reference signal have the same frequency and fixed phase shift θ

$$V_{ref} = B \cos[\omega t + \theta] \tag{4.23}$$

the PSD then mixes these signals to produce the following output signal

$$V_{PSD} = A \cos[\omega t] B \cos[\omega t + \theta] = \frac{1}{2} AB \cos[\theta] + \frac{1}{2} AB \cos[2\omega t + \theta] \tag{4.24}$$

The amplitude of the reference signal is kept constant meaning the resulting signal from the PSD is proportional to the amplitude of the input signal, proportional to the phase between the input and reference signals and is modulated at twice the reference frequency. The signal then passes through a narrow-band low pass filter, which removes the oscillating $2\omega t$ component, leaving the resultant DC signal.

A phase portrait illustrating the process, after the low pass filter, can be seen in figure 4.11. As long as the noise has no phase/frequency relationship with the frequency of the reference and input signal, in theory, all noise can be removed by filters.
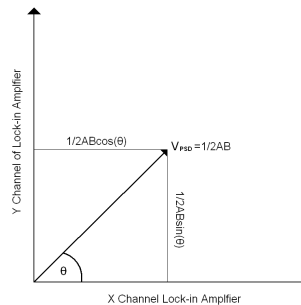
Figure 4.11: Lock-in Amplifier phase diagram representation.

In our experiments, the emitter was biased using an AC signal, with an offset of half the amplitude, as to avoid using the second harmonic for demodulation. This AC signal was generated using the signal generator, which also had a reference signal of the same frequency, passed to the lock in amplifier. 13.333Hz was regularly used as a frequency, as the odd number helped avoid any interference with a 50Hz power supply.

As a signal generator a Yokogawa FG120 was used, see figure 4.12. Depending on the measurement, two different voltage sources were used. For voltages below 10V

the NI PXI-6722 8ch AO 13bit voltage source was used, due to its ease of use with
LabView programs. For larger voltages a Yokogawa 7651 DC source, controlled
by a GPIB interface was utilised. Voltage reading was done using Keithley 2000
Multimeters (GPIB Interface), however when extra inputs may have been needed the
NI PXI-6030E Multifunction I/O was also used. Three different Lock-In amplifiers
were used, these were the EG& G 5302 Lock-In Amplifier, PekinElmer 7265 DSP
Lock-In Amplifier and the PekinElmer 7280 DSP Lock-In Amplifier.

Figure 4.12: Equipment setup for photoresponse measurement.

4.3.6 Capacitive Measurement

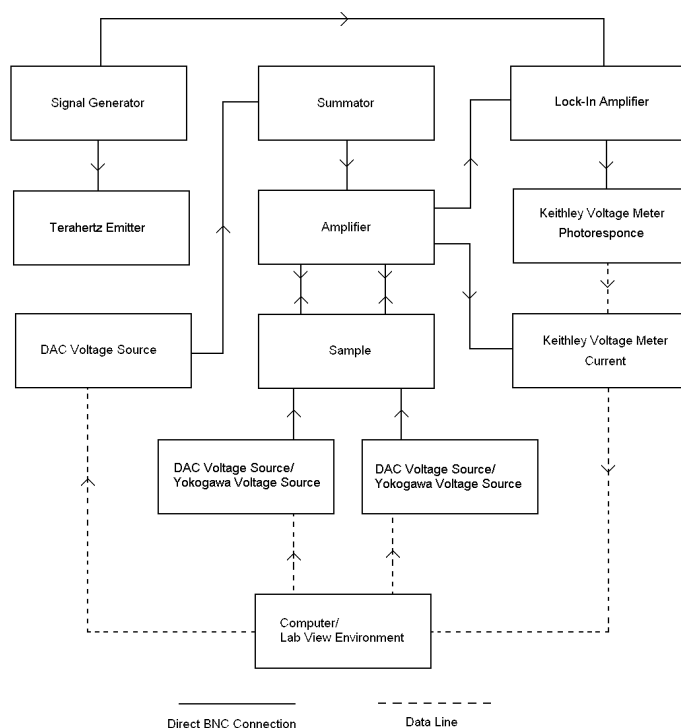Throughout the experimentation, it became apparent that we required a reliable method to check whether the 2DEGS that form the QDs in both the SQW and DQW case were actually present and not damaged. It is believed that a number of heterostructures used during testing, particularly for the DQW structures, were damaged and did not contain a working 2DEG. It also became noted that in some cases, applying to high a negative voltage to one of the QD or PC gates would cause the opening of higher order conduction channels through the mesa. These channels were then unable to be closed using a negatively biased gate. Only warming the sample back up and cooling it back down would close these channels and allow pinch off. It was suggested that UV light shinned on the sample may repopulate the QWs, however our experimental setup did not allow this option.

So to test whether the 2DEG layers were working correctly it was found that a sensitive capacitance measurement could be taken between a gate and the mesa channel its self.[93] As can be seen in figure 4.13, an oscillating voltage is applied to one of split the gates on the sample. The mesa channel of the sample is connected to a current amplifier and the other end of the mesa is left floating. The current amplifier is then connected to a lock in amplifier which then demodulates the signal at the applied frequency used on the cross gate. The amplitude of the oscillation and the gain on the amplifier are adjusted to obtain the greatest signal. The voltage offset of the gate is then swept into the negative range, essentially pinching off the mesa. As the 2DEG layer becomes pinched off, the induced charge oscillations in the mesa from the gate decrease, as the over all capacitance decrease, therefore allowing us to easily identify at which voltage each 2DEG layer becomes pinched off and to ultimately identify that a 2DEG layer is present.

The technique is sensitive enough that when the offset is swept in small enough steps, both the top and bottom layers in a DQW heterostructure may be identified, as can be seen in section 5.2. Although this technique was not used for the actual experimental testing of how we wished the sample to operate, it did become a very powerful tool in testing the presence of the 2DEG layer in some samples.
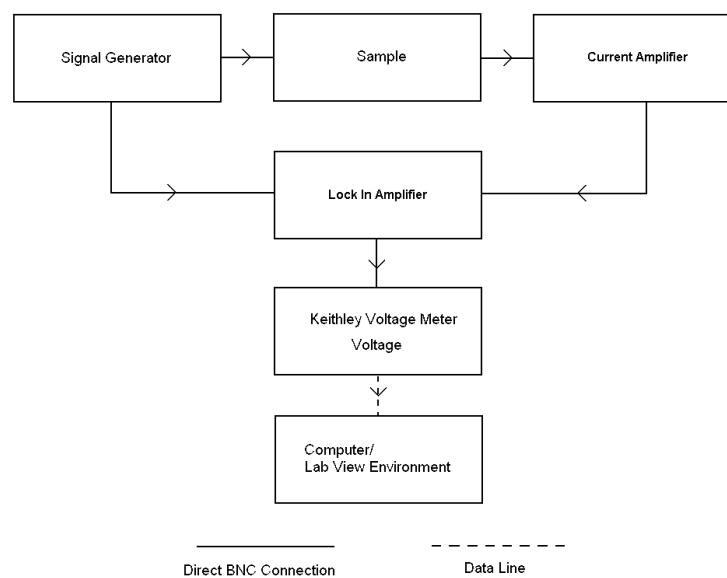
Figure 4.13: Equipment setup for gate-2DEG capacitive measurement.

5 Experiments and Results

A THz radiation sensor in which the photon-induced ionisation state could be read out using both a Point Contact (PC) and SET was studied. We compare the operation of QD-PC and QD-SET devises of different designs. The QD-PC devises, where the state QD is probed by the PC, concede in sensitivity to that with the SET, but gain the advantages of higher operation temperature, 1.5K opposed to below 1K, and have less demanding fabrication needs.

From this we went on to develop a device where two capacitively coupled QDs are formed in the double quantum well heterostructure. We use both a PC and a SET for read out of the QDs. Devices based on double quantum wells would have advantages in tuning of the resonance spectral line. I report the progress in the development of this sensor. A simplified model of the operation of the QD sensor is also discussed.

The operational principal of the semiconductor THz sensor presented here is similar to single photon counting using QDs in high magnetic field.[5] It was demonstrated that the absorption of THz radiation could resonantly excite magnetoplasma oscillations, followed by a charge excitation of the QD.[5] The QD was then probed using a SET. The sensor demonstrated a high spectral resolution of $\sim 1\%$ and single photon sensitivity. A low temperature scanning terahertz microscope has now been developed using this technology.[94]

The main limitations with the detector is the need for a high magnetic field, above 2T, and low temperatures below 0.3K. Introduction of a metallic SET allowed us to remove the need for a magnetic field, however due to size and charging energy of the metallic SET, operational temperatures below 1K are still needed. To ensure that the SET would work above 1K, a SET with tunnel junctions of $0.03 \times 0.03 \mu m^2$ would need to be produced, as to obtain a charging energy, $E_c = \frac{e^2}{C}$, greater than that of the thermal energy, $k_b T$. Currently this is a challenging fabrication task.[95] One can lift the operation temperature by utilising a point contact as sensitive electrometer. In this device the QD charge state directly affects the conductance of the PC near its pinch off point. I present data on operation of both SET-QD and PC-QD detectors.

The excitation of an electron out of the QD occurs in two stages. Plasma oscilla-

tions in the vicinity of the QD are first excited, which then decays and inturn hands over the energy to a single electron excitation. This electron then has the sufficient energy to overcome the potential barriers of the QD. This is clearly demonstrated at more negative gate potential, where the switching events due to thermal excitations are completely suppressed.

5.1 Quantum Dot Sensors in Single Quantum Well Heterostructures

The devices were fabricated using a GaAs/AlGaAs heterostructure with a single quantum well. A 2DEG approximately 100nm deep into the semiconductor, with an electron mobility of $\mu \sim 6 \times 10^5 cm/Vs$ and an electron density of $n = 1.6 \times 10^{11} cm^{-2}$. Two designs were fabricated and tested. The first design with PC and QD gates utilises the PC and SET readout technique. The second design with two cross gates utilises only the SET readout method. In both designs the QD is formed in an etched mesa channel using a metallic gate(s). The SETs are fabricated directly above the QDs allowing greater coupling to the QD, compared to lateral positioning, in each design, see figure 5.1. The QD is positioned in the focal point of a log-periodic antenna approximately 1.5 mm in diameter, designed to operate in the frequency range of 0.2 and 2 THz. The experiments were carried out in a temperature range from 0.3 K to 1.5 K.

As a THz source, we use filtered black body radiation emitted by a resistor heated by a bias current. The resistor is placed 60 cm away from the sensor. The radiation is guided to the experimental sample using a 2 mm stainless steel light pipe. The light pipe cuts off wavelengths greater than 2 mm. Unwanted infrared radiation is filtered off using a black polyethylene film and two silicon filters. It was estimated that the transmission efficiency of the optical system is 2×10^{-3}, at a dissipated electrical power of 3.6mW corresponding to an emitted power of $2.77 \times 10^{-6} W$ in the 0.2-2THz range. A full discussion on the optical system can be found in section 4.2.
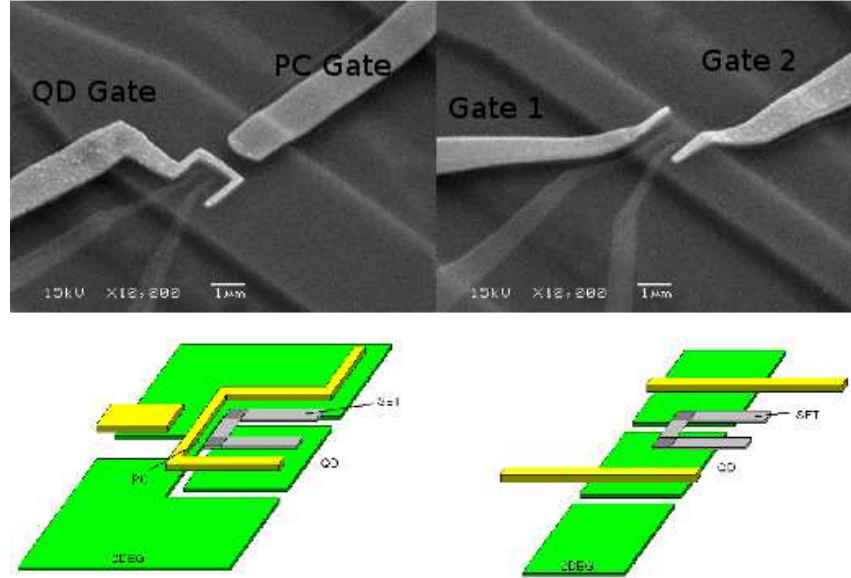
Figure 5.1: SEM micrograph of the sensors. Left: Design of the sensor with PC and QD gates. Right: Design of the sensor with cross gates, Gate 1 and Gate 2.

5.1.1 QD Sensor with the PC and QD Gates Design

We start with operation of PC-QD sensor. We took scans varying the bias of both the QD and PC gates as to establish a PC pinch off map, figure 5.2, as to ascertain in what region the detector should be most sensitive. Ideal operation point is expected where the QD is formed and the PC is pinched-off simultaneously. This happens where the pinch off boundary is crossed by the dashed line. The latter is the boundary of QD formation taken from the SET map in figure 5.3.

Figure 5.2: Conductance map of PC as a function of the QD and PC gate. Blue corresponds to zero current and white to approximately 1 nA. The dashed line indicates the pinch off of the QD (measured with SET).

In figure 5.2 we can see four distinct areas. Area one indicates a formed QD but with a closed PC. Zone two indicates an open QD and an open PC. Zone three indicates a formed QD but open PC and zone four indicates a closed PC but open QD.
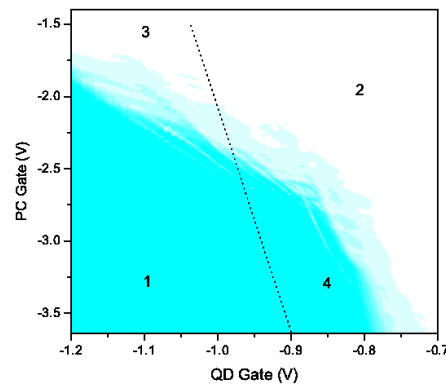
An SET current map in coordinates of voltages applied to V_{qd} and V_{pc} can be seen in figure 5.3. The boundary between different periods of the CB oscillations indicates the formation of the QD. It is not vertical, indicating that the PC gate bias also has an influence on the formation and shape of the QD.
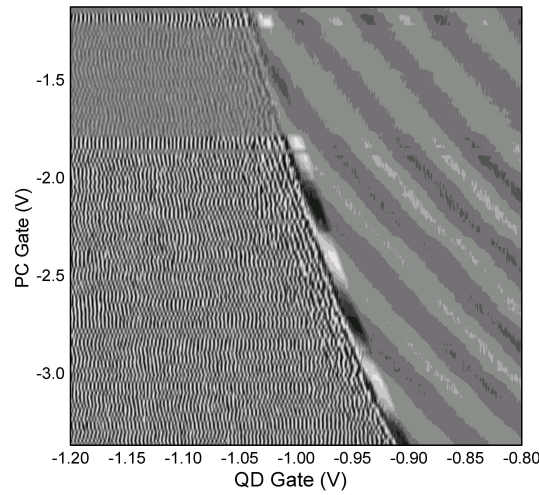
Figure 5.3: SET current map as a function of applied voltage to both PC and QD gates. The area with the short period CB oscillations is the region of the formed QD.

For QD-PC operation the PC channel is biased with a voltage of 0.25mV through a 200KΩ resistor. The PC current is sensitive to the charge state of the QD at the point of pinch off. In order to measure photoresponce we keep the bias constant for the QD gate and scan the PC bias, while measuring the current across the channel, as can bee seen by the dashed line in figure 5.4. Current drops to zero below the pinch off voltage of $\sim -2.4V$. The pinch-off boundary shifts when the THz photon flux is applied, see blue line in figure 5.4. The photoresponce is then the difference between the two curves of PC current.

We used the lock-in method to investigate the effect, by modulating the source at 9Hz and recording the PC current demodulated at twice the frequency, see the

Figure 5.4: Point contact dark current (dashed line) and point contact current when under terahertz illumination (blue line). Also shown is the difference between these two data sets (open circles) which is the photoresponce. QD gate voltage -1.06V.
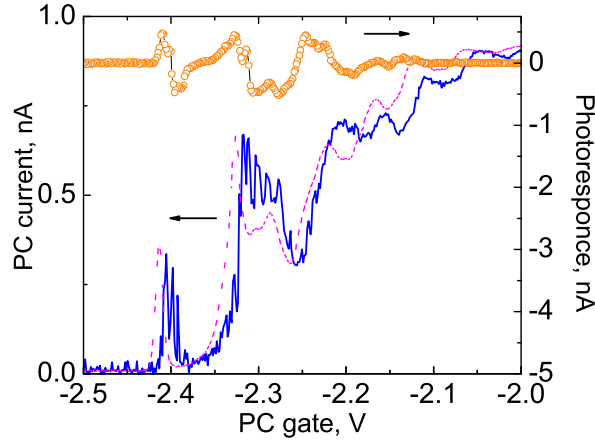
orange line in figure 5.4. It can be seen that the maximum of the photoresponce current is of the order of the PC current when completely open. One anomaly can be seen at $V_{PCG} = -2.1V$ where there is a difference between the dark current and point contact current under illumination, however this is not represented in the photoresponce data. It was later found that this was a temporary artificial error caused by a software error within the lock-in amplifier.

We further investigated the maximum photoresponce for a given power and different QD gate bias voltages, as can be seen in figure 5.5. As a reference we take a lock-in signal when the source is off, i.e the dark current signal. This signal is believed to be caused due to random charge fluctuations in the channel as well as any radiation that may be emitted from any components in the optical system, although the latter is believed to be minimal. The lock-in amplifier is also sensitive to the impedance at the input. As the gate voltage is biased it will effect the conductance of the PC channel therefore significantly changing its impedance, this will then be manifested as a contribution towards the dark current in the figure. The sign and magnitude of the photoresponce at different QD and PC potentials near the pinch off boundary follows the same pattern as the dark signal, solid line in figure 5.5. Small emitted powers of less than 3mW only produce a photoresponce in the $V_{QDG} \sim -0.97V$ region, but this is extended to $V_{QDG} \sim -1.2V$ at higher powers

and therefore greater photon flux. The signal to noise ratio also improves with a more negative QD gate potential. It is believed that the photoresponce extends to a more negative gate voltage at higher emitter power due to more energetic photons reaching deeper states within the QW and exciting them out of the QD. These states would have been unattainable to less energetic photons.
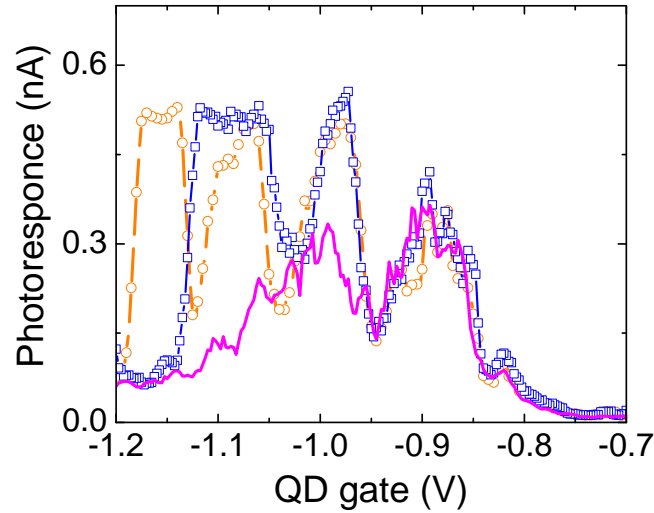
Figure 5.5: Photoresponce are a function V_{QDG} for different emitter powers. No power (solid line), 14mW (open squares) and 26mW (open circles).$V_{PC} = -2.3V$.

We found that the photoresponce becomes saturated when an emitted power exceeds 3mW. As the power of the emitter is increased and therefore the incident flux, multiple excitations from the QD to the PC channel occur. With each excitation a relaxation event will also occur restoring the QD to its original state. As more simultaneous excitations happen, the relaxation rate will increase. Saturation of the photoresponce is reached once the overall excitation rate and relaxation rate become equal. Performance of the detector only slightly degrades as the temperatures increases from 0.3K to 1.5K. This can be seen in figure 5.6. The photoresponce starts at approximately 2.2mW. Below this value the incident flux is insufficient to be detected once it has passed through the optical system due the quantum efficiency of the QD. Also, below this power the black body spectrum emitted is not in the ideal region for the detector to operate.

We can estimate the sensitivity of the PC to the charge excitation of the QD as
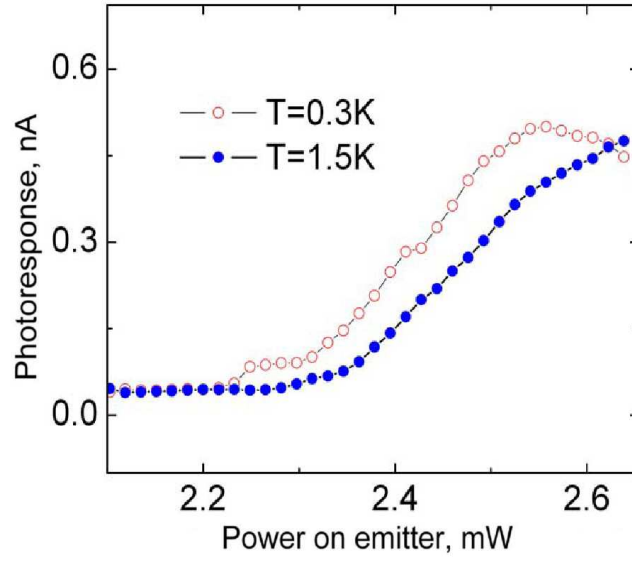
Figure 5.6: Power dependence of the detected photoresponce, at $V_{QDG} = -1.01V$ at both 1.5K and 0.3K.

$$\frac{\partial I_{PC}}{\partial Q} = \frac{\partial I_{PC}}{\partial V_g} \frac{1}{C_{QD}^{PC}} \frac{C^{QD-PC}}{C_{\Sigma}^{PC}} \qquad (5.1)$$

where V_g is the PC gate voltage, I_{PC} the current through the channel and C_{QD}^{PC} is the capacitance between the PC gate and the QD, C^{QD-PC} is the capacitance between the QD and PC, C_{Σ}^{PC} is the total capacitance of the PC. We calculate the maximum values of $\frac{\partial I_{PC}}{\partial Q}$ for a different QD gate bias in figure 5.2, see figure 5.7. The maximum sensitivity is $\sim 4.1 \times 10^6 A/C$.

Figure 5.7: Point Contact charge sensitivity as a function of QD gate voltage. We can see a maximum of approximately $4.1 \times 10^6 A/C$.

We can estimate the minimum charge excitation of the QD, which can be regis-

100

tered by the PC using the formula

$$\Delta I_e = Ne \frac{\partial I_{PC}}{\partial V_g} \frac{1}{C_{QD}^{PC}} \frac{C^{QD-PC}}{C_\Sigma^{PC}} \tag{5.2}$$

where N is the number of electrons in the given excitation and ΔI_e is the current noise of the measurement system. The current noise is $\sim 2pA$ in our system, which when using equa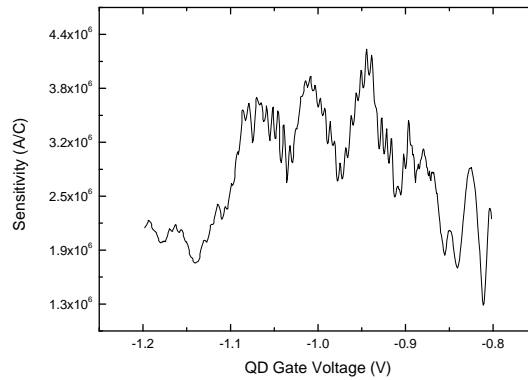tion 5.2 correspondes to approximately five electron excitations. This would show that the PC is capable of detecting excitations of a few electrons.

In figure 5.2 streaks along the uneven pinch off boundary are seen. They decrease with a temperature increase, but they can still be seen at 1.5 K. We believe that a small dot is formed in the PC channel, which is in Coulomb blockade regime. The streaks are a manifestation of the Coulomb blockade of tunnelling through this dot. We estimated the size of this dot to be 200 nm. The presence of the Coulomb Blockade Oscillations (CBOs) increase the maximum sensitivity of the sensor. But at the same time the operation of the device becomes sensitive to fine tuning of the gate voltage.

It has also been noted that near the pinch off boundary, the temporal fluctuations in the dark signal appear to be enhanced. The dark signal follows the pattern of streaks near the pinch off boundary, reflecting the high sensitivity of the PC readout at this point due to the large gradient of current, respective to the gate voltage, dI/dV_g. With all the gate potentials fixed, it is the charge state of the QD that determines the conductance of the PC channel. Near the pinch off point where the barriers to the QD are still of the order of the electrochemical potential of the surrounding 2DEG, thermal energy induces charge fluctuations in the QD, leading to the large dark current. This current then decreases with either lowering the potential barriers of the QD, causing the 2DEG to become more strongly coupled to the 2DEG, or when the barriers are increased, preventing the thermally induced fluctuations on the QD.

We continue with the operation of SET-QD detector. At the boundary where the QD is becoming isolated from the 2DEG, "switchings" of the SET current are visible, caused by excitations of electrons in/from the QD. At this QD gate voltage the potential barriers that form the QD are still of the same order in magnitude as the electrochemical potential of the surrounding 2DEG, allowing thermal excitations

of electrons to occur. Once the barriers are far greater than the surrounding elec-
trochemical potential, this effect is completely suppressed. The noticeable electron
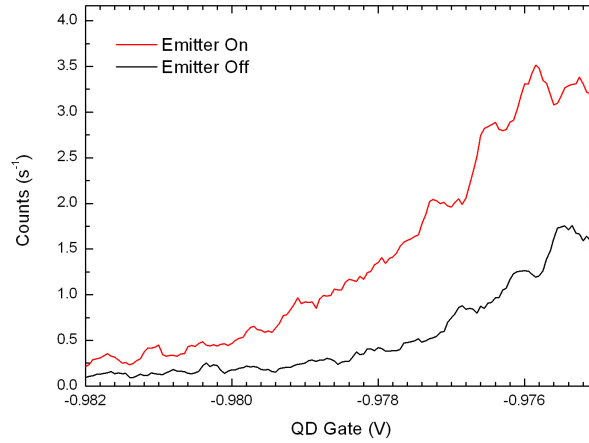excitations out of the QD only happen due to a THz photon absorption event.

Figure 5.8: SQW QD-PC SET switching count rate with emitter on and off. PC gate biased
to -2.3V. Measurement taken over 120 seconds. Emitter dissipation power 26mW.

Using the SET coupled to the QD-PC sensor, the electron excitations of the QD
was measured with both the emitter on and off, as can be seen in figure 5.8. The PC
voltage of -2.3V was found to give the largest signal response when an excitation
was detected. The measurement was taken over 120 seconds. It can be seen that
there is a clear increase in the excitation count rate when the emitter is switched on.

The coupling of the QD to the 2DEG reservoirs is controlled by biasing the QD
gate. As the (negative) bias is increased, then the tunnel junction resistances will
increase and the QD becomes de-coupled from the 2DEG reservoirs. Large period
CBOs of the SET are seen before the QD is de-coupled from the reservoirs, see figure
5.9. At this point a change in period and amplitude of the CBO happens due to the
emerging of extra capacitance between the SET and the QD gate. This is discussed
further below.

To finish analysis I discuss the electrostatic model of the system. The electronic
equivalent circuit of the system is shown in figure 5.10.

Before the QD becomes decoupled from the 2DEG, the effective capacitance
between the SET and QD gate is
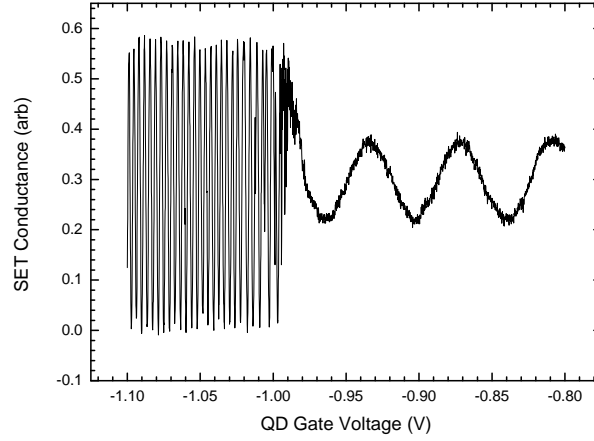
Figure 5.9: SET conductance. Point contact gate is biased to -2.1V. Change in period from 63mV to 4mV can be observed as the QD becomes isolated from surrounding 2DEG. Thermal excitation of electrons out of the QD can be observed near the pinch off point. QD formation and isolation from the reservoirs can be seen at approximately -0.97V.
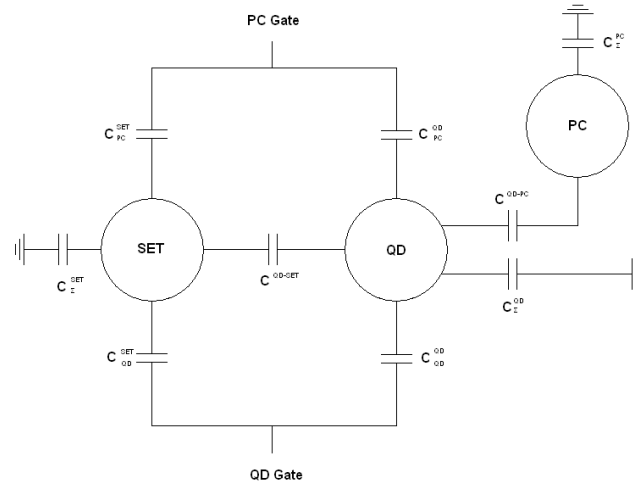
Figure 5.10: A simplified electronic model of the device fabricated.

$$C_1 = \frac{C^{QD-SET} + C_\Sigma^{SET}}{C^{QD-SET} + C_\Sigma^{SET} + C_{QD}^{SET}} C_{QD}^{SET} \tag{5.3}$$

After the QD is isolated from the 2DEG, the effective capacitance between the SET and QD gate becomes

$$C_2 = C_1 + \frac{C_{QD}^{QD}(C^{SET-QD}C_\Sigma^{QD} + C^{SET-QD}C_\Sigma^{SET} + C_\Sigma^{QD}C_\Sigma^{SET})}{C^{SET-QD}C_\Sigma^{QD} + C^{SET-QD}C_\Sigma^{SET} + C_\Sigma^{QD}C_\Sigma^{SET} + C_{QD}^{QD}C_\Sigma^{SET} + C_{QD}^{QD}C^{SET-QD}} \tag{5.4}$$

103

One can estimate the capacitances using either estimation or experiment. One can find capacitance between the QD and the SET using following equation

$$C = \varepsilon_r \varepsilon_0 \frac{A}{d} \tag{5.5}$$

where ε_r is the relative static permittivity of the material, ε_0 is the electric constant ($\varepsilon_0 \approx 8.854 10^{-12} Fm^{-1}$), A is the area overlap and d is the distance between layers. We assume a permittivity of 3 for polyimide materials[96] and 12.85 for GaAs-like structures.[97] We then use an average of the ε_r for multiple materials. For example, to calculate C^{QD-SET}, where the SET is sits on a 200nm layer of polyimide, with the QD being approximately 100nm below the surface in the AlGaAs substrate, we take $\varepsilon_r \approx (12.85 + 3 + 3)/3 \approx 6.3$. For C^{QD-SET} we take the area of the SET island, $1.08 \times 10^{-15} m^2$, to be the overlap area and the distance to be $300 \times 10^{-9} m$. This gives a capacitance of $2 \times 10^{-19} F$.

In order to calculate C_{PC}^{SET}, C_{QD}^{PC} and C^{QD-PC} we consider the device components as flat co planar strips. This allows us to use the two parallel coplanar strips capacitance model[98]

$$C = l \varepsilon_r \varepsilon_0 \frac{K(\sqrt{1 - k^2})}{K(k)} \tag{5.6}$$

where l is the length of the strip, K is the elliptical integral and $k^2 = k_1 k_2$. We define $k_i = \frac{d}{2w_i + d}$ where w_i is the width of the strips, and d is the distance between them. From this we can find $C_{PC}^{SET} = 5.3 \times 10^{-18} F$, $C_{QD}^{PC} = 9.6 \times 10^{-17} F$ and $C^{QD-PC} = 5.2 \times 10^{-17} F$. We may also calculate the capacitance of the QD to the environment, C_{Σ}^{QD}, assuming it is a flat metallic disc, using the following equation[99]

$$C = 8 \varepsilon_r \varepsilon_0 r \tag{5.7}$$

where r is the radius of the disc. This gives a value of $C_{\Sigma}^{QD} = 4.3 \times 10^{-16} F$. Taking the radius of the QD to be 475nm and knowing the electron concentration, we may also estimate the number of electrons in the dot to be approximately 1100. C_{QD}^{SET} was determined using the change in period of the CBOs in figure 5.9, giving a value of

$C_{QD}^{SET} = 7.0 \times 10^{-18} F$. C_{QD}^{QD} was determined using computer simulation giving a value of $C_{QD}^{QD} = 3.1 \times 10^{-17} F$ and we found $C_{\Sigma}^{PC} = 8.2 \times 10^{-16}$. C_{Σ}^{SET} was calculated from the SET charging energy of $0.34 meV$, it gives a capacitance of $C_{\Sigma}^{SET} = 2.4 \times 10^{-16} F$.

The I-V characteristic of the SET used on the device can be seen in figure 5.11. From the curve we find a normal resistance of $R_n \approx 740 K\Omega$ and the SET charging energy of 0.34 meV.
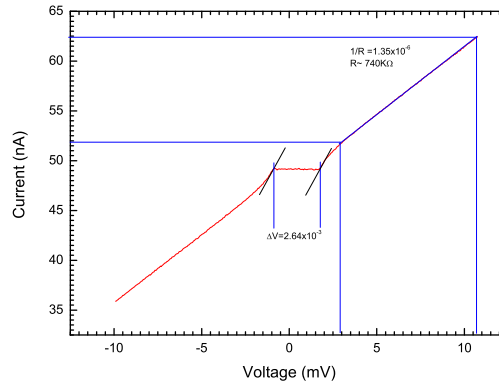

Figure 5.11: I-V Curve of the SET in QD-SET sensor measured at 0.3K.

5.1.2   QD Sensor with the Cross Gate Design

A SET current map taken using the cross gate configuration can be seen in figure 5.12.
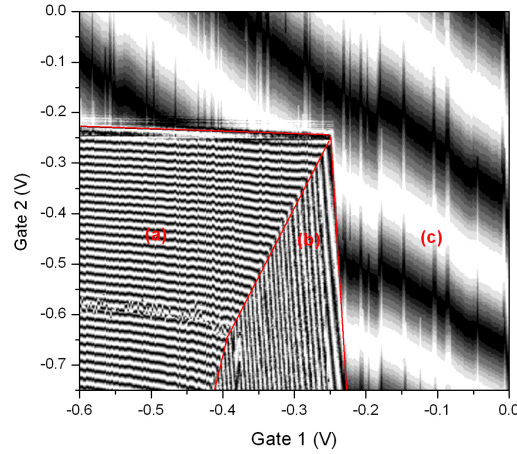
Figure 5.12: SET current map as a function of applied voltage to both gates 1 and 2 in the cross gate design. Pinch off boundary is illustrated by the thick red line. The "spikes" in the map are believed to be random charge fluctuations.

Region (a) indicates both a QD and PC formed. Region (b) indicates an isolated QD, but with one tunnel barrier continuously increasing, causing electrons to "spill" out of the QD. It is the continuos biasing of one of the gates that causes one of the barriers to increase. Region (c) indicates a region where the QD is not formed.

By correctly biasing the gates, the QD can be put in a state where random telegraph switching events can be observed, due to the gate potentials only being just being large enough to isolate the QD. This allows thermally excited electrons to enter and leave the QD. Beyond this point we would expect to see an increased number of switching events when radiation is incident on the QD, as seen in figure 5.13.

When investigating this further, by looking at the region -0.194V to -0.199V, we can see how count rate is indeed increased by a factor of two at approximately -0.1955V compared to the dark rate count, as seen in figure 5.14. Significant peaks in photoresponce are indicated with arrows.

Examples of the specific switching trace marked by arrows in figure 5.14 can be
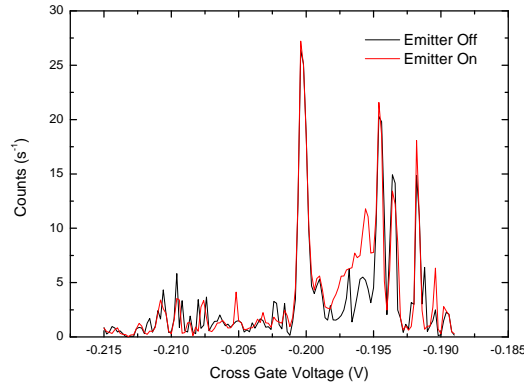
Figure 5.13: SET switching count rate with emitter on and off. One cross gate is fixed voltage, 0.451V. Measurement taken over 140 seconds. The power dissipated at emitter is $\sim 22mW$.
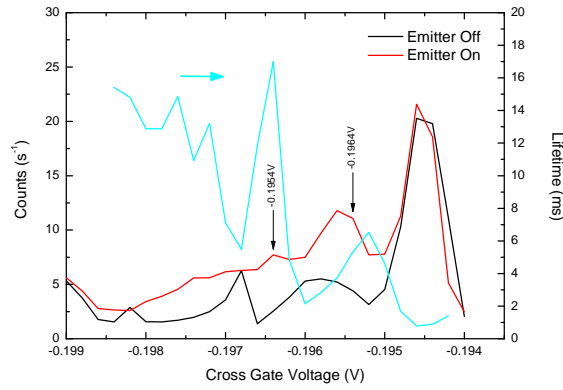
Figure 5.14: Zoomed in version of figure 5.13. Blue curve indicates a lifetime of excitations in QD. The lifetime increases as cross gate voltage becomes more negative. Specific photoresponce regions are marked at -0.1954V and -0.1964V.

seen in figure 5.15. The amplitude of switching events are approximately four times larger than the background noise amplitude. The time traces of the SET current show this clear increase in switching events under THz radiation, see figure 5.15.
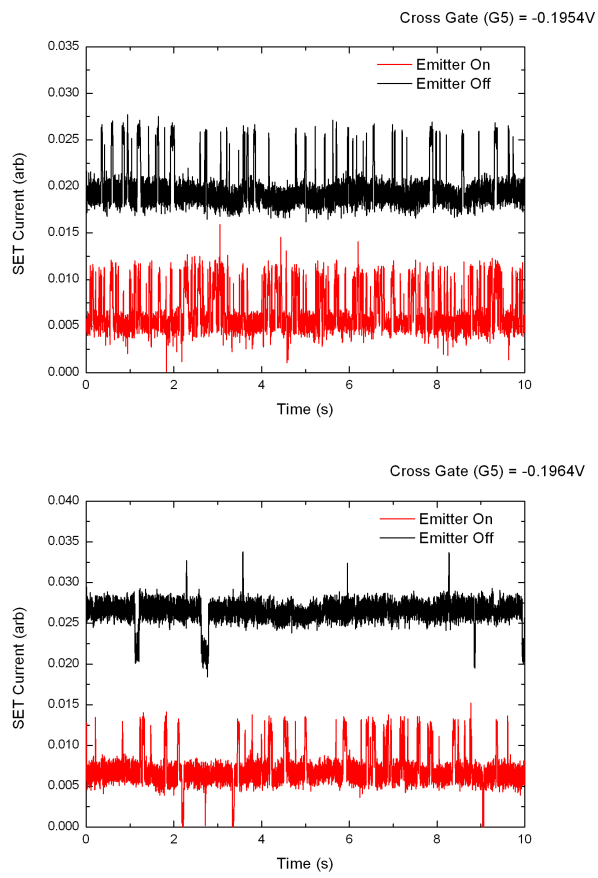
Figure 5.15: Example SET current switching traces. Traces correspond to cross gate voltages of -0.1954V and -0.164V are shown.

5.2   Double Quantum Well Quantum Dots

We use our standard designs in order to investigate the double quantum well system (DQW). The only significant differences of the DQW system compared to the SQW system was the design of heterostructure used. The energy band structure of the heterostructure used can be seen in figure 2.12 in section 2.2.2.1. The first quantum well is defined at a depth of approximately 100nm and has a reported electron concentration of $N_s = 3.2 \times 10^{11} cm^{-2}$ and a mobility of $\mu = 11 \times 10^4 cm^2/Vs$. The second quantum well is at a depth of approximately 260nm with a reported concentration of $N_s = 4.4 \times 10^{11} cm^{-2}$ and a mobility of $\mu = 12.8 \times 10^4 cm^2/Vs$. Further information regarding the heterostructure can be found in section 3.1. We characterised the DQW sample. The mesa resistance, 3.06$k\Omega$, was linear in the range of $\pm 5mV$ at 1.4K, giving a sheet resistance of 383Ω.
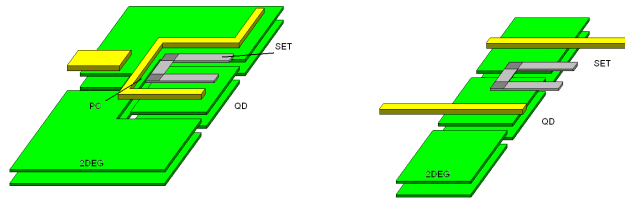

Figure 5.16: Split gate design and image used for DQW testing.

Similar to the SQW samples the QD(s) is formed by negative bias of the QD gate, causing the QD to become isolated in the etched mesa channel, as can be seen in figure 5.16. The same THz source and optical system were used as in the SQW samples. Experiments were conducted at temperatures between 0.3 K and 1.5 K. Figure 5.17 shows the labelling scheme for the PC and QD gates used in the testing.

5.2.1   QD Sensor with the PC and QD Gates Design

We first began by studying the QD-PC sensor. The channel is biased with a voltage of 1mV and negative voltage is applied to PC and QD gate. The corresponding pinch off curve is shown in figure 5.18.

Although pinch off was achieved, it was not repeatable. It is thought that during the pinch off, the higher order conduction channels in the substrate are opened, circumnavigating the 2DEG layers. Due to higher order conduction channels being
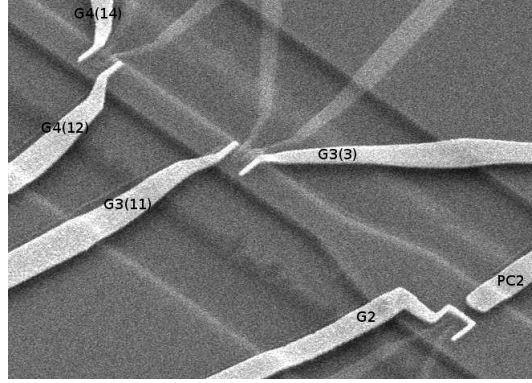
Figure 5.17: SEM picture of the devices made from DQW heterostructure.
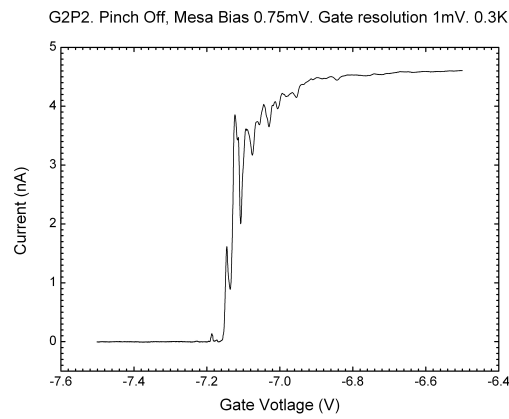
Figure 5.18: Pinch off curve of the sensor with DQW. Overall pinch off is achieved at approximately -7.16V.

opened when greater negative bias was applied, the channel could not be pinched off. This is believed to occur due to conduction electrons being shifted in the z-direction, due to the applied bias, from the known QWs to some unknown state(s) which are deeper then the depth of the etch that was carried out. These conduction channels could not then be closed again without warming the sample back up. This prevented further photoresponce testing using the QD-PC sensor, as it was not possible to produce a conductance map of the sample.

It was expected for the PC to form in the top QW. The QDs formed in the neighbouring 2DEG layers are capacitively coupled to each other meaning they can then be read out using the PC in the top 2DEG. No successful QD-PC with operational SETs were produced.

The electrostatic equivalent circuit of the system is shown in figure 5.19. As many dimensions and properties are the same in both the SQW and DQW case,

some values will be very similar. We assume the relative permittivity of polyimide as 3 and the heterostructure as 12.85. Using equation 5.5 we find $C^{QD-SET} = 2 \times 10^{-19}F$ and $C^{TQD-BQD} = 4.2 \times 10^{-16}F$.

Using equation 5.6 we find $C_{PC}^{SET} = 5.3 \times 10^{-18}F$, $C_{PC}^{TQD} = 9.6 \times 10^{-17}F$, $C^{TQD-PC} = 1.7 \times 10^{-16}F$, $C^{BQD-PC} = 1.7 \times 10^{-16}F$, $C_{PC}^{BQD} = 1.3 \times 10^{-16}F$.

Using equation 5.7 we find $C_{\Sigma}^{TQD} = 4.3 \times 10^{-16}F$ and assuming the bottom QD is larger than the top, and has a radius of 550nm, we find $C_{\Sigma}^{BQD} = 5 \times 10^{-16}F$. With the known electron concentrations, we can estimate the top QD to contain 2250 electrons and the bottom QD to contain 4200.

We may find C_{Σ}^{SET} from the SET charging energy, 0.34meV, to be $C_{\Sigma}^{SET} = 2.4 \times 10^{-16}F$. C_{QD}^{TQD} and C_{QD}^{BQD} were found using computer simulation. They are $C_{QD}^{TQD} = 7.0 \times 10^{-18}F$ and $C_{QD}^{BQD} = 2.8 \times 10^{-17}F$. C_{QD}^{BQD} being larger, as it was estimated that the bottom QD would be in larger radius than the top. C_{Σ}^{PC} was also found to be $C_{\Sigma}^{PC} \sim 5.5 \times 10^{-16}F$.
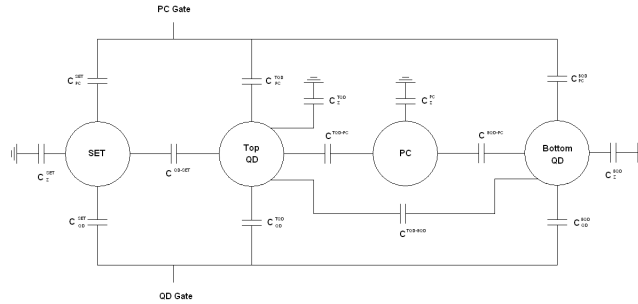
Figure 5.19: A simplified electronic model of the DQW device fabricated.

5.2.2 QD Sensor with the Cross Gate Design

To confirm that the gates were causing depletion in the desired area, therefore allowing a QD to be formed, AC capacitive measurements were taken. The method is described in section 4.3.6. Depletion curves from these measurements can be seen in figure 5.20. An oscillating voltage of 150mV at 11kHz was applied to the gate, while the constant bias voltage was swept between 0V and -3V in 0.5mV steps.

Depletion of the top QW can be observed in the region of -2V and -2.25V as can be seen in figure 5.20. Curve G4(12) has two dips, the first dip at -0.7V is probably an anomaly, as the current later recovered. Higher (negative) voltage was applied
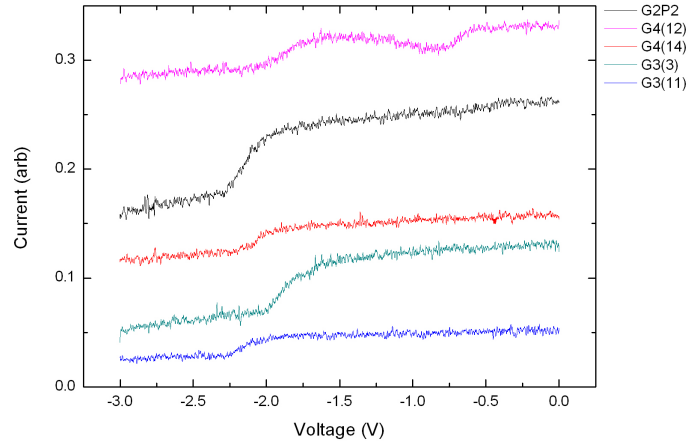
Figure 5.20: DQW capacitive measurement depletion curves. Curves are shifted in the Y direction for ease of comparison.

to the gates to ascertain if depletion of the bottom QW could be achieved, as seen in figure 5.21. The depletion of the second QW appears to occurs at approximately -5V.
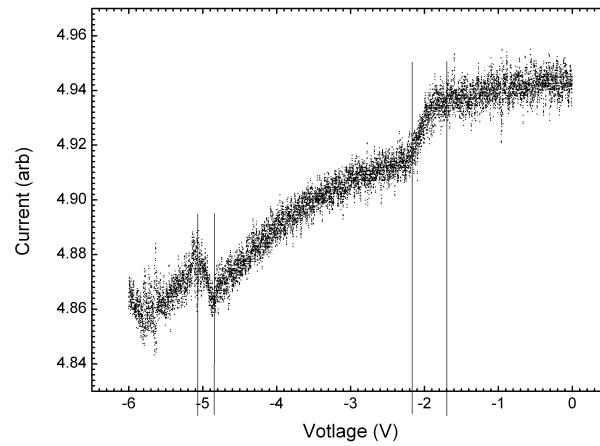
Figure 5.21: High negative bias capacitive measurement depletion curve.

As already explained, once higher bias was used, the pinch off cannot be repeated until the sample is heated up to room temperature, as shown by figure 5.22.

A 2D map of SET current using two cross gate, G3(11) and G3(3), can be seen in figure 5.23. Red lines indicate areas of QD formation. As can be seen in the graph, a change in CBO period can be observed, although it is very small. The period in CBOs before pinch off corresponds to a capacitance between the SET and the gate of $3.8 \times 10^{-18} F$ and after pinch off corresponds to $7.0 \times 10^{-18} F$. From the capacitive measurements, we can confirm that the top QD has become isolated from
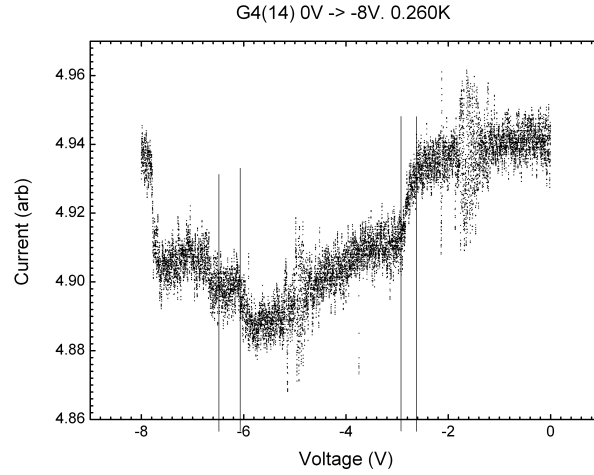
Figure 5.22: Failed capacitive measurement pinch of curve. Grey lines indicate regions where pinch off was expected to be observed.

the surrounding 2DEG. The question remains unanswered about the bottom 2DEG. We do not see any features in figure 5.23 indicating the depletion of bottom 2DEG. It is believed that the bottom layer is not completely isolated.

Photoresponse measurements were then taken with the same sample. The SET was biased to 0.65mV, as this was near a quasi-particle point and found to be the area of greatest sensitivity, as can be seen in figure 5.28. The 2D map of SET current with emitter set for 35mW and emitter off, is shown in figure 5.23. No noticeable effect was detected by using the lock-in technique also.

We repeated the experiment, but we changed sweep direction: we fixed the voltage at G3(11) gate and swept the G3(3) gate as shown in figure 5.24. The map appears different to figure 5.23, fixed G3(11) has high capacitance to the SET, and the CBO of the SET with respect to this gate is not resolved in the map due to large steps used, see figure 5.27. No prominent photorespance is detected. Some switching was found on the boundary at $V_{G3(11)} = -2.706V$.

Time traces of the SET current were taken with the emitter on and off, with a 30 second waiting time between traces. The data was analysed to find the mean current amplitude, switching counts and integral counts as seen in figure 5.25.

The curve of integral counts is not affected by the threshold level used to calculate counts. The inset of figure 5.25 shows the mean current amplitude. It is approximately the same for both emitter on and off. No clear photoresponse has
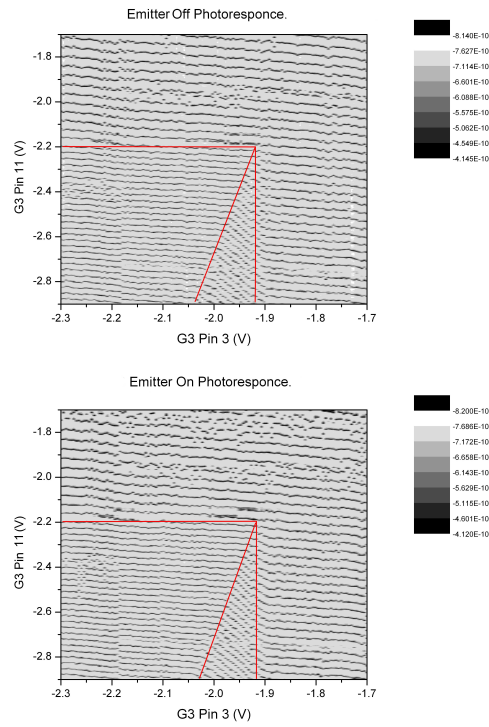
Figure 5.23: SET bias -0.65 mV. Average Peak maxima in top graph 0.399nA and 0.408nA in bottom graph.

been detected.

Closer examination of the actual switching events, as can be seen in the example in figure 5.26, shows that although a distinct signal can be seen over the random noise telegraph switching, the signal to noise ratio of only 2:1. From experiments with SQW heterostructure, a signal to noise ration of at least 4:1 is needed for operation of the detector.

Figure 5.27 shows the CBOs caused by the individual neighbouring cross gates, G3(3) and G3(11), to the SET, as shown in figure 5.16. The difference in capacitance indicates a non symmetrical geometry of the gates with relation to the SET. From this we were able to find $C_{QD}^{SET} = 5.3 \times 10^{-18} F$. A larger period CBO gives the effect of reduced resolution in the 2D SET photocurrent map, as seen in figure 5.24.

Figure 5.28 shows the I-V characteristic of the SET. From the curve, we can find a normal resistance of $R_n \approx 301 K\Omega$ and a charging energy of $0.34 meV$. Josephson quasi particle peaks can be seen at $-7.96 \times 10^{-4} V$ and $6.89 \times 10^{-4} V$.
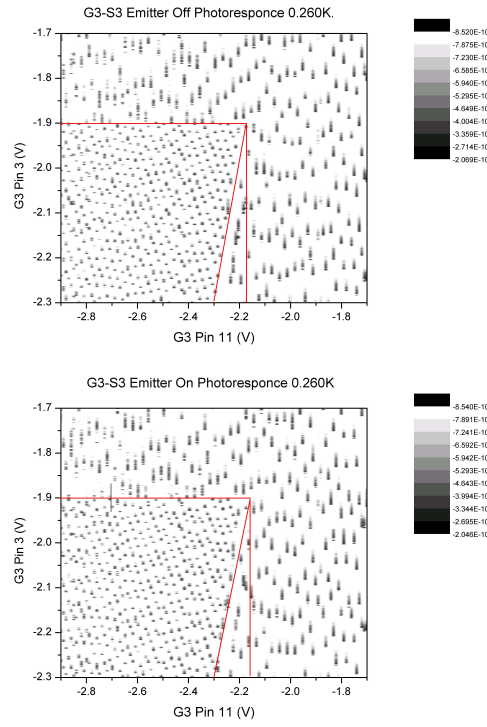
Figure 5.24: DQW SET photoresponce measurement. SET bias -0.65 mV. Average Peak maxima in top graph 0.850nA and 0.858nA in bottom graph.
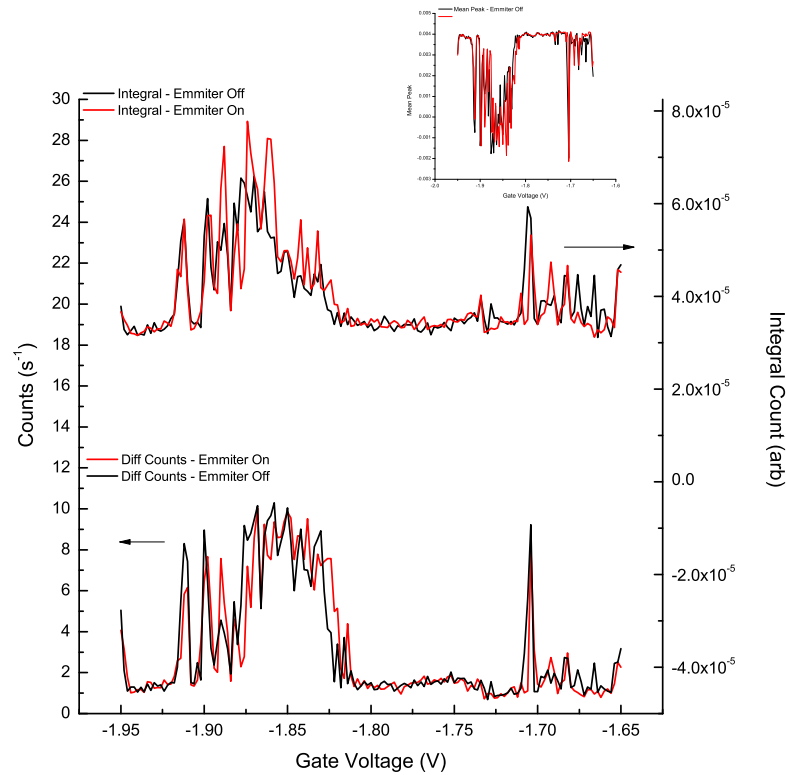
Figure 5.25: SET telegraph switching analysis. SET biased to -0.645mV. Scan taken over 120 seconds.

115
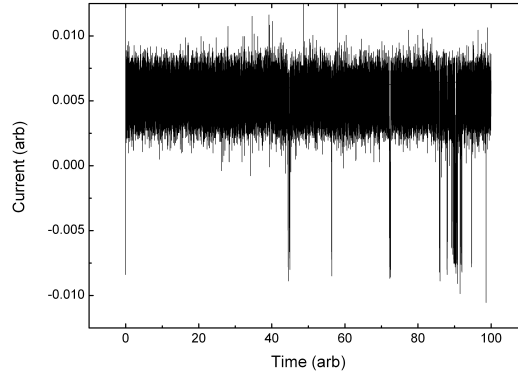
Figure 5.26: Example switching trace of QD with emitter turned on.
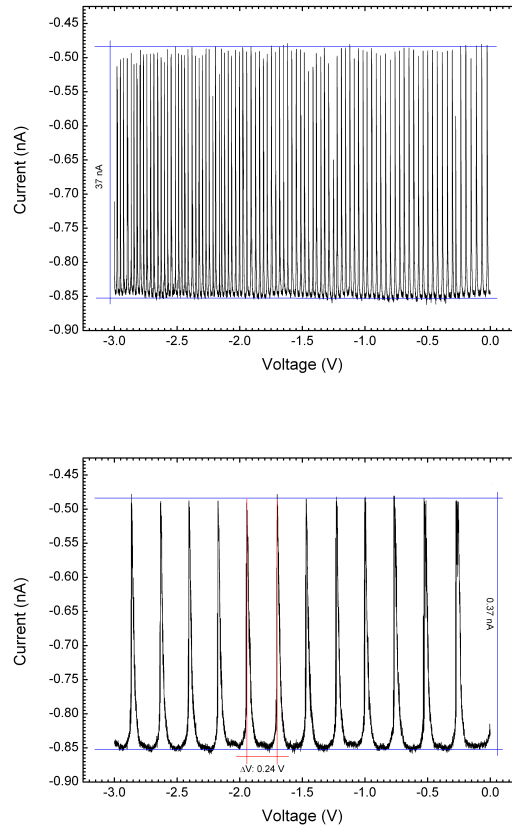
Figure 5.27: Top: CBOs due to SET being swept with cross gate G3(11). Due to the larger capacitance, it can be seen that this gate is physically closer to the SET than G3(3) below. CBO period indicates a capacitance of $5.3 \times 10^{-18} F$. SET bias -0.525mV. Bottom: CBOs due to SET being sweeped with cross gate G3(3). CBO period indicates a capacitance of $6.7 \times 10^{-19} F$. SET bias -0.525mV.
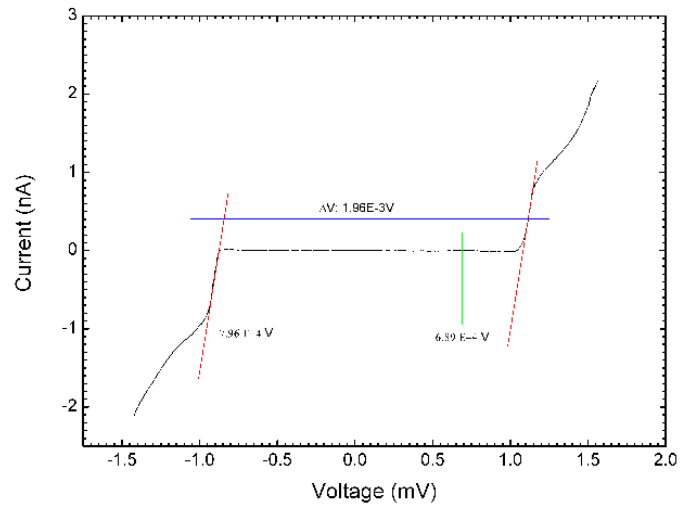
Figure 5.28: I-V Curve of the SET in DQW QD-SET sensor, measured at 0.256K.

6 Conclusions

In this section I make conclusions on the fabrication technology and experimental results with both the SQW and DQW samples.

6.1 Summary of Fabrication Technology

Existing fabrication technology for the production of SQW sensors already existed. Only minor adaptations to the existing process were required. The design was altered slightly over the course of the project to enable easier fabrication.

The final designs are presented in section 3.1. The orientation of the gates and SETs were adjusted to enable easier lift off. The fine mesa was adapted to be one long channel, rather than individual fine channels for each individual QD site, allowing greater flexibility of alignment. The SET pathways were also redesigned to so that some may share a common pathway. This allowed the number of connections from the sample to the chip package to be reduced from 20 to 16. This was of great use, as it allowed operation of the whole sample, as the probe for the cryostat only allowed the use of 16 pin chip packages.

In the SQW samples, only two aspects were permanently adjusted in the actual fabrication. This was the second bake of the polyimide to harden and cure it further, making it less susceptible to acetone dissolving it. The other fabrication change was the use of a thicker layer of 6% copolymer for the undercut layer of the QD gates. This allowed much easier lift off during this stage of fabrication.

The final part of fabrication, which always required the greatest fabrication demand, was the formation of the SETs. Much research was required to find the correct parameters of development time for both layers of resist, angle of evaporation and aluminium deposition thickness. Many other factors affected this, such as the instillation of a new needle valve on the evaporator, effectively changing all the oxidising parameters. Finally however, evaporation angles of 13°, deposition thickness of 35nm, and oxidising time of eight minutes at 30 mtorr with an oxygen flow rate of $10cm^3s^{-1}$ would produce SETs with a charging energy in the order of 0.2-0.4meV. The success rate of SET formation and operation would be in the order

of approximately 60%. Care also had to be taken to avoid static discharge which would destroy the SET. This was particularly noticed during the bonding process and loading/unloading samples onto the probe. Extra care was also required in grounding the SET before any alteration of measurement was performed.

The existing fabrication technology was adapted to cater for the development of the DQW sensor. In general, all the existing fabrication techniques remained the same. Two problems presented themselves however. It became apparent that there was an issue with the ohmic connection between the SET pathways and external gold antenna pads. A similar problem between the gate pathways and external gold antenna pads also arose. It was also noted that on many occasions bad annealed ohmic contacts had been formed to the 2DEG.

At an early stage, it was noted that the annealing parameters required for DQW heterostructure would need to be different, due to an increased depth of the final 2DEG layer. A full discussion on this problem and potential solutions are presented in section 3.4.

The final problem encountered with the DQW samples involved a problem with the e-beam patterned pathways (SETs and Gates) ohmically connecting to the gold pads of the antenna structure. It is thought that due to the increased etch depth of the mesa, that the polyimide splined at greater angles between the surface of the substrate and the fabricated structures. This would require longer than preferable etching times in oxygen plasma. To overcome this problem, another gold antenna pattern was deposited on top of the polyimide, guaranteeing ohmic connection. This is further discussed in section 3.8.

6.2   Summary of Experimental Techniques

Experiments were performed in 0.3K Heliox $^4He/^3He$ single shot cryostat system. The majority of experimentation was done at base temperature of 260-300 mK. The system allowed 16×0.15 mm constantan wires for connection to the sample in the sample space. The system also had fitted a 2mm steel light pipe leading to the sample space to allow the transmission of radiation to the samples. This setup allowed base

temperatures to be held for approximately 50 hours, and sample change time of approximately one day. Until the design of the sample was modified as described above, it was found that only having 16 signal lines to be inconvenient, as each sample originally had 20 connection points. The system was very limiting on the type of emitter used to produce the radiation, as the system only allowed a small resistor/HTC stack to be used. Replacement/changing of the emitter also required the probe to be removed from the cryostat. This could possibly be improved by installing fibre optics to the sample space, rather than a light pipe, potentially allowing external THz sources. It was later thought that the cables connecting to the emitter might cause interference in the signal lines. To overcome this issue, RF lines were fitted to the probe, and used to connect the emitter to the external power source, removing any potential interference caused. Full operation of the system is described in section 4.1.

The emitter and optical system setup is described in section 4.2. It has been estimated that while the maximum dissipated emitter power is 34.4mW, the incident power onto the sample is $1.56 \times 10^{-8}W$ with an NEP of $1.77 \times 10^{-11}\frac{W}{Hz^{1/2}}$. The values used are more likely to be over estimates however, as many of the parameters are taken as approximations. When the emitter is being modulated, there will be a delay time as it heats up until it reaches its maximum, therefore making our estimate potentially idealised. A number of potential improvements could be introduced. A new frequency specific emitter that operates at a greater power but at cooler temperature, as not to heat up the sample space, could be used. As suggested above, fibre optics could also be used to allow an external source. Further investigations into improved mirrors and filters could also aid with the radiation transmission. It also needs to be taken into account that these objects would also emit radiation in their own right.

The amplifier design used proved to be very effective and robust in operation. Signals with nanoamp accuracy were routinely measured. With the current setup of the amplifier, few improvements would be required. Higher precision resistors with exact ohmic values could be used for the amplifier gain circuitry, however, this would only marginally improve the amplification accuracy. During the course

of the experimentation, extra shielding was added to the amplifier box to ensure a full Faraday cage around the circuitry, helping to reduce noise. The amplifiers used within the circuitry are INA128 Precision, Low Power Instrumentation amplifiers. It was experimented with changing these to AD8221 instrumentation amplifiers as they have a lower noise and higher DC accuracy performance. AD8221 are compatible with the existing circuitry. However attempts to change to the amplifier were abandoned due to technical difficulties relating to the different footprint of the two amplifier chip packages.

Five main measurement techniques were used throughout the project to obtain the desired data. These were techniques used for measuring I-V characteristics, mesa channel pinch off characterisation, the recording of QD telegraph type switching events, photoresponce measurements and finally capacitive measurements used to confirm the presence and depletion points of 2DEGs. Throughout experimentation these measurement techniques and setups have performed well. The main issues encountered with these setups was identifying noise sources and ground loops. This was rectified on an experiment by experiment basis by locating sources of noise and grounding any points that were required to improve the signal to noise ratio. Noises of source included poor grounding between the cryostat and measurement system, in particular the amplifier, missing grounding points for certain measurement equipment and noise introduced due to the power sources used. The latter problem was rectified by using a dedicated filtered power supply. It was attempted to have a single ground point to which all other grounds were connected to avoid any grounding loops.

6.3 Summary of Experimental Results

The following section will summarise the results obtained and conclusions drawn from the SQW and DQW experiments.

6.3.1 Summary of Single Quantum Well Quantum Dot Results

Both a SQW QD-PC and QD-SET were realised, characterised and utilised for THz photoresponce measurements. The 2DEG had an electron concentration and mobility of $n = 1.6 \times 10^{11} cm^{-2}$ and $\mu \sim 6 \times 10^5 cm/Vs$ respectively. It was approximately 100nm below the surface of the substrate. A QD was successfully isolated and probed with both a SET system operating at 0.3K and a PC system operating at 1.5K. The SET used was found to have a normal resistance of $740 K\Omega$ and a charging energy of 0.34meV.

The system operates by the QD becoming charge excited due to a terahertz photon absorption event. The photon causes plasmon excitation in the surrounding 2DEG, which then decay in the form of a hand over electron, causing the QD to become excited. This excitation can then be detected by either the PC channel or SET, which are both capacitively coupled to the QD.

A simplified capacitive electronic model of the system was presented and all capacitances were found through a combination of experimental testing and calculations. The QD-SET system was found to have a sensitivity of $10^{-4} \frac{e}{Hz^{-1/2}}$. Photoresponce was found in both systems. Detectivity in the QD-PC was estimated as $4.1 \times 10^6 A/C$. It was also shown that the response seems to plateau above 14mW at the emitter. It was shown that photoresponse only slightly degraded when the temperature is increased from 0.3-1.5K. It was demonstrated that although the QD-SET system is more sensitive, the QD-PC system has advantages over it. Namely a higher operational temperature, simpler operation and simpler fabrication demands, making it the most promising system for further development. The QD-PC system has since been developed further into an imaging system operating at a frequency of 0.17THz while still maintaining single photon sensitivity, utilising multiplexing circuitry to read out many QDs or pixels along a minimum number of wires.[100]

We can see that when comparing the QD-PC and QD-SET sensors that the QD-SET sensor has the advantage of having an order of magnitude greater charge sensitivity than the QD-PC. However it should be noted that the PC acts in a planar geometry, where the SET sits directly above the QD, allowing for a stronger capacitive coupling and potentially better performance compared to the QD-PC. The QD-SET is limited in operation to temperatures below 1K and has a more demanding fabrication. The QD-PC does have the advantage of operating in a temperature of 1.5K and works over a wider range of operational gate voltages.

To date no other system using QDs to detect terahertz radiation has been devised that matches our systems single photon sensitivity and spectral resolution.

6.3.2 Summary of Double Quantum Well Quantum Dot Results

A DQW QD-SET sensor was realised and photoresponce measurements were taken. This is the first type of sensor to utilise stacked QDs for terahertz photon detection, although research has been carried out on the interaction between parallel 2DEGs, their plasmon interactions and the potential to couple to radiation.[65,66]

The first quantum well is found at a depth of approximately 100nm and has a reported electron concentration of $N_s = 3.2 \times 10^{11} cm^{-2}$ and a mobility of $\mu = 11 \times 10^4 cm^2/Vs$. The second quantum well is at a depth of approximately 260nm with a reported concentration of $N_s = 4.4 \times 10^{11} cm^{-2}$ and a mobility of $\mu = 12.8 \times 10^4 cm^2/Vs$. The SET used was found to have a normal resistance of approximately $301 K\Omega$ and a charging energy of 0.34meV.

A simplified capacitive electronic model of the system was presented and all the capacitance's were found. Capacitive measurements of the 2DEG were performed to confirm the presence of a 2DEG player and a pinch off point. From this information we were able to operate the QD-SET. It was believed that a QD is formed in the top layer 2DEG, but not fully formed in the bottom 2DEG. This is believed as a bias less than that found required to pinch off both 2DEGs was used, but the voltage was greater than that required to pinch off the top layer. This was done as it was found that once both 2DEG layers were fully pinched off, the layers could not again be later pinched off until the sample was brought back to room temperature, as discussed

above. Photoresponce was not clearly found using photoresponce measurements including the use of the lock-in technique. A signal to noise ratio of 2:1 was found, but a minimum of 4:1 is needed for a successful detector.

It was not possible to realise a DQW QD-PC sensor, due to an inability to pinch off the conducting mesa channel and therefore form a point contact for measurement.

The system operation is similar to that of the SQW structure also investigated. The inclusion of the second 2DEG potentially allows stronger coupling to terahertz radiation due to the plasmon interactions between the QWs as discussed in section 2.2.2.7. Future developments of the sensor would include deeper etch depths to the mesa as to allow full pinch off as to avoid the QWs depleting into unknown traps/wells. The inclusion of a back gate would also allow greater control of the spatial symmetry of the two QWs, thus allowing greater control of the coupling of incoming radiation to the plasma interactions of the two QWs, and potentially allowing increased spectral sensitivity compared to the SQW sensor.

A Current Density Derivation using the Wigner Function

Below is the derivation of the current density based on the Wigner approach. [101] Starting with the variable effective mass Hamiltonian

$$H(z) = -\frac{\hbar^2}{2m}\frac{d}{dz}\left(\frac{1}{m(z)}\frac{d}{dz}\right) + v(z) \tag{A.1}$$

where $v(z)$ is the double well potential. We then write the Liouville equation for the density matrix as

$$\frac{\partial \rho(z,z')}{\partial t} = \frac{i}{\hbar}(H(z) - H(z'))\rho(z,z') \tag{A.2}$$

with the density matrix defined as

$$\rho(z,z') = \sum_i P_i \Phi_i(z)\phi_i^*(z') \tag{A.3}$$

where $\phi_i(z)$ is the ith state wavefunction and P_i is the ith state occupation probability. The following change of variables is then carried out

$$Z = \frac{1}{2}(z + z') \tag{A.4}$$

$$\xi = z - z' \tag{A.5}$$

This is done as to define the Wigner function as the Fourier transform of the density matrix

$$f(Z,k) = \int_{-\infty}^{\infty} d\xi e^{ik\xi}\rho(Z + \frac{1}{2}\xi, Z - \frac{1}{2}\xi) \tag{A.6}$$

The partial differential equation for the Wigner function is then given by

$$\frac{\partial f}{\partial t} = -\frac{\hbar k}{m}\frac{\partial f}{\partial z} - \frac{1}{\hbar}\int_{-\infty}^{\infty}\frac{dk'}{2\pi}V(Z, k - k')f(Z, k') \tag{A.7}$$

where we define $V(X, k)$ as

$$V(X,k) = 2 \int_0^\infty d\xi \, \sin(k\xi)[v(Z + \tfrac{1}{2}\xi) - v(Z - \tfrac{1}{2}\xi)] \tag{A.8}$$

The Wigner function and density matrix are then normalised. Also we define

$$n(Z) = \rho(Z,Z) = \int_{-\infty}^\infty \frac{dk}{2\pi} f(Z,k) \tag{A.9}$$

as to represent the electron density $n(Z)$, so that $f(Z,k)$ is solved self consistently and coupled to the Poisson equation, giving

$$\frac{\partial}{\partial Z}\left(\epsilon \frac{\partial \phi}{\partial Z}\right) = -e[\Gamma(Z) - n(Z)] \tag{A.10}$$

where Γ is the impurity density and the potential $\phi(Z)$ is related to $v(Z)$ via

$$v(Z) = -[\Upsilon_e(Z) - \Upsilon_e(0)] - e[\phi(Z) - \phi(0)] \tag{A.11}$$

where Υ_e is the electron affinity in the semiconductor. The current density can then be defined as

$$J(Z) = e \int_{-\infty}^\infty \frac{dk}{2\pi} \frac{\hbar k}{m(Z)} f(Z,k) \tag{A.12}$$

B Current Derivation using the Landauer Function

Below is the derivation of the current between the two electrodes in a triple barrier system using the Landauer approach.[101] Starting with the current defined as

$$\vec{I} = eT_r(n\vec{v}) = \frac{eA}{(2\pi)^3}\sum_\sigma \int d^3k F_\sigma(\vec{k})\vec{v}_\sigma(\vec{k}) = \frac{2eA}{(2\pi)^3}\int d^3k F(\vec{k})\vec{v}(\vec{k}) \tag{B.1}$$

Where $F(\vec{k})$ is the Fermi distribution, $\vec{v}(\vec{k})$ the electron velocity and T_r is the trace of the spin sum being carried out.

$$\vec{v}(\vec{k}) = \frac{1}{\hbar}\vec{\nabla}_k\epsilon(k) \tag{B.2}$$

We further define F_A as the electron equilibrium distribution on the incident side, A, of a sample and F_B on the exiting side, B. From this we define the probability of electron transmission to be

$$F_A(1 - F_B)T(\vec{k}) \tag{B.3}$$

Where $T(\vec{k})$ is tunnelling probability. We can now substitute equations B.2 and B.3 into equation B.1 to obtain a current from point A to B

$$\vec{I}_{AB} = \frac{2eA}{(2\pi)^3\hbar}\int d^3k T_{AB}F_A(1 - F_B)\vec{\nabla}_k\epsilon(k) \tag{B.4}$$

We must also consider any current flow B to A. A similar expression to the above can be found for the current flowing from B to A. We therefore take the overall current to be the net current from A to B

$$\vec{I} = \vec{I}_{AB} - \vec{I}_{BA} = \frac{2eA}{(2\pi)^3\hbar}\int d^3k T(\vec{k})[F_A(\vec{k}) - F_B(\vec{k})]\vec{\nabla}_k\epsilon(k) \tag{B.5}$$

We now define

$$\vec{k} = k_\parallel \hat{i} + k_\perp \hat{j} \tag{B.6}$$

where $k_{\parallel}$ and $k_{\perp}$ are the parallel and perpendicular components in a cylindrical energy space. Further to this we may now write

$$d^3k = \frac{dS_\epsilon d\epsilon}{|\vec{\nabla}_k \epsilon(k)|} \tag{B.7}$$

where $dS_\epsilon = d^2k_{\parallel}$ and is the area of the cylindrical cap in k space, with the cylinders length being $dk_{\perp} = \frac{d\epsilon}{\vec{\nabla}_k \epsilon(k)}$. Substituting equation B.6 and B.7 into equation B.5, and define $\hat{n}_{v(k_{\parallel}, k_{\perp})} = \frac{\vec{\nabla}_k \epsilon(k)}{|\vec{\nabla}_k \epsilon(k)|}$, we have

$$\vec{I} = \frac{2eA}{(2\pi)^3 \hbar} \int dS_\epsilon \int d\epsilon T(k_{\parallel}, \epsilon)[F_A(k_{\parallel}, \epsilon) - F_B(k_{\parallel}, \epsilon)]\hat{n}_{v(k_{\parallel}, k_{\perp})} \tag{B.8}$$

We now define $F_i(k_{\parallel}, \epsilon)$ as

$$F_i(k_{\parallel}, \epsilon) = \frac{1}{1 + \exp\left(\frac{\epsilon_{K_{\parallel}} + \epsilon - E_{Fi} + e\phi_i}{KT}\right)} \tag{B.9}$$

where $\epsilon_{k_{\parallel}} = \frac{(\hbar k_{\parallel})^2}{2m}$, $\epsilon = \frac{(\hbar k_{\perp})^2}{2m}$ and ϕ_i is the bias voltage applied on side i of the sample (i.e. either A or B). If we assume we can neglect the plane motion dependence of the transmission, we may write

$$T(k_{\parallel}, \epsilon) \to T(\epsilon) \tag{B.10}$$

We also consider the F_i in the same plane, so it may be evaluated by a two dimensional integral

$$\int dS_\epsilon = \frac{(2\pi)^2}{A} \tag{B.11}$$

We may now define the Landauer function for the tunnelling current in the z direction, where we take $\hat{n}_v \to \hat{z}$, to be

$$I_{LF} = \frac{2eA}{2\pi\hbar} \int T(\epsilon)[F_A(\epsilon) - F_B(\epsilon)]d\epsilon \tag{B.12}$$

Alternately if in equation B.8 we now change $F_{k_{\parallel}, \epsilon}$, but retain the change of $T(k_{\parallel}, \epsilon)$, we may now perform the integral using the identify

$$\int_0^\infty dS_\epsilon = \int_0^{2\pi} \int_0^\infty k_\parallel dk_\parallel d\theta = \frac{2\pi m}{\hbar^2} \int_0^\infty d\epsilon_\parallel \tag{B.13}$$

This results in

$$\int_0^\infty dS_\epsilon [F_A(k_\parallel, \epsilon) - F_B(k_\parallel, \epsilon)] = \frac{2\pi m}{\beta \hbar^2} \ln\left(\frac{1 + \exp[-\beta(\epsilon + e\phi_A - E_{FA}]}{1 + \exp[-\beta(\epsilon + e\phi_A - E_{FB}]}\right) = \frac{2\pi m}{\beta \hbar^2} F(\epsilon)$$
$$\tag{B.14}$$

where $\beta = \frac{1}{K_b T}$ and $F(\epsilon)$ is known as the supply function.[102] The final current, known as the Standard Tunnelling Theory (STT) current in the z direction is

$$I_{STT} = \frac{emAKT}{2\pi^2 \hbar^3} \int T(\epsilon) F(\epsilon) d\epsilon \tag{B.15}$$

C   Annealing Boat Calibration

Annealing was done by heating the sample to be annealed using a thermal boat in an inert argon environment within a thin film evaporator.

A custom flat thermal boat was designed and shaped from 0.125mm tungsten sheet of 99.99% purity. The boat is of rectangular shape and has dimensions of 20mm x 50mm.

Calibration was carried out by attaching a thermocouple to the boat within the evaporator (Edwards 306A) and the following parameters used:

Initial Pressure: 2.2×10^{-5}torr

Ar flow Rate: $11cm^3/s$

Pressure With Flow: 4.2×10^{-4}torr

Time between readings: 30s

The following calibration graph was recorded:
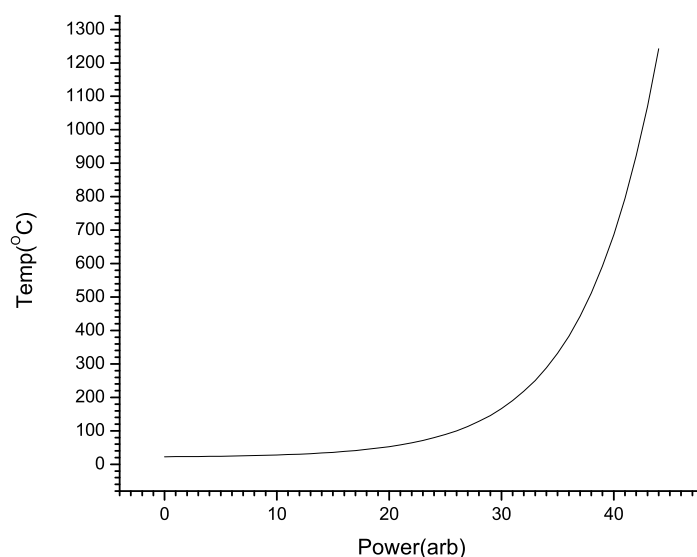
Figure C.1: Thermal boat annealing temperature calibration graph.

D Glossary Of Terms

2DEG – Two Dimensional Gas.

CBO – Coulomb Blockade Oscillation.

CVD – Chemical Vapour Deposition.

DOS – Density Of States.

DQW – Double Quantum Well.

HEP/HEB – Hot Electron Photodetector/Hot Electron Bolometer.

QD – Quantum Dot.

MBE – Molecular Beam Epitaxy.

NEP – Noise Equivalent Power.

PC – Point Contact.

SET – Single Electron Transistor.

SIN – Superconductor-Insulator-Normal junction.

SQUID – Superconducting Quantum Interference Device.

SQW – Single Quantum Well.

TDS – Time Domain Spectroscopy.

Bibliography

[1] S. C. Shi and J. Yang. Terahertz space telescope (tst) and receiver development. *36th COSPAR Scientific Assembly, Beijing, China*, July 2006.

[2] PH Siegel and RJ Dengler. Terahertz heterodyne imager for biomedical applications. *Proceedings of SPIE*, SPIE-5354:1–9, 2004.

[3] P. L. Richards. Bolometers for infrared and millimeter waves. *J. Appl. Phys*, 76 (1):1–24, 1994.

[4] J. J. A. Baselmansa *et al*. Doubling of sensitivity and bandwidth in phonon cooled hot electron bolometer mixers. *Applied Physics Letters*, 84(11), 2004.

[5] S. Komiyama *et al*. A single-photon detector in the far-infrared range. *Nature*, 403:405–407, Jan 2007.

[6] *TeraEye Collaboration*. http://www.teraeye.com.

[7] Ahmad S. Semiconductor switching devices - future trends. *Defence Science Journal*, 48(1):45–59, January 1998.

[8] Michael C. Kemp *et al*. Security applications of terahertz technology. *Proc. of SPIE*, 5070:44–52, August 2003.

[9] John F Federici *et al*. Thz imaging and sensing for security applications explosives, weapons and drugs. *Semiconductor Science and Technology*, 20, June 2005.

[10] K. Uhlig and C. Wang. Cryogen-free dilution refrigerator precooled by a pulse-tube refrigerator with non-magnetic regenerator. *AIP Conf. Proc.*, 823:939–945, 2006.

[11] Sushil Kumar, Benjamin S. Williams, Stephen Kohen, Qing Hu, and John L. Reno. Continuous-wave operation of terahertz quantum-cascade lasers above liquid-nitrogen temperature. *Applied Physics Letters*, 84(14):2494–2496, 2004.

[12] N. G. Asmar, A. G. Markelz, E. G. Gwinn, J. Černe, M. S. Sherwin, K. L. Campman, P. F. Hopkins, and A. C. Gossard. Resonant-energy relaxation of terahertz-driven two-dimensional electron gases. *Phys. Rev. B*, 51(24):18041–18044, Jun 1995.

[13] S. Pelling, R. Davis, L. Kulik, A. Tzalenchuk, S. Kubatkin, T. Ueda, S. Komiyama, and V. N. Antonov. Point contact readout for a quantum dot terahertz sensor. *Applied Physics Letters*, 93(7):073501, 2008.

[14] John C. Mather. Bolometer noise: nonequilibrium theory. *Appl. Opt.*, 21(6):1125–1129, 1982.

[15] D. Mangalaraj Sa. K. Narayandassa P. Manoravib M. Josephb Vishnu Gopalc R. K. Madariac R. T. Rajendra Kumara, B. Karunagarana and J. P. Singh. Room temperature deposited vanadium oxide thin films for uncooled infrared detectors. *Materials Research Bulletin*, 38(7):1235–1240, June 2003.

[16] A. Skalare, W. R. McGrath, B. Bumble, H. G. LeDuc, P. J. Burke, A. A. Verheijen, R. J. Schoelkopf, and D. E. Prober. Large bandwidth and low noise in a diffusion-cooled hot-electron bolometer mixer. *Applied Physics Letters*, 68(11):1558–1560, 1996.

[17] Leonid Kuzmin. Ultimate cold-electron bolometer with strong electrothermal feedback. volume 5498, pages 349–361. SPIE, 2004.

[18] J. Clarke, G. I. Hoffer, P. L. Richards, and N. H. Yeh. Superconductive bolometers for submillimeter wavelengths. *Journal of Applied Physics*, 48(12):4865–4879, 1977.

[19] A. Luukanen and J. P. Pekola. A superconducting antenna-coupled hot-spot microbolometer. *Applied Physics Letters*, 82(22):3970–3972, 2003.

[20] Adrian T. Lee, Paul L. Richards, Sae Woo Nam, Blas Cabrera, and K. D. Irwin. A superconducting bolometer with strong electrothermal feedback. *Applied Physics Letters*, 69(12):1801–1803, 1996.

[21] E.N. Grossman, D.G. McDonald, and J.E. Sauvageau. Far-infrared kinetic-inductance detectors. *Magnetics, IEEE Transactions on*, 27(2):2677–2680, Mar 1991.

[22] J.E. Sauvageau, D.G. McDonald, and E.N. Grossman. Superconducting kinetic inductance radiometer. *Magnetics, IEEE Transactions on*, 27(2):2757–2760, Mar 1991.

[23] A D Semenov, G N Gol'tsman, and R Sobolewski. Hot-electron effect in superconductors and its applications for radiation sensors. *Superconductor Science and Technology*, 15(4):R1–R16, 2002.

[24] G.N. Gol'tsman B.S. Karasik A.M. Lyul'kin E.M. Gershenzon, M.E. Gershenzon and A.D. Semenov. Fast superconducting electron bolometer. *Sov. Tech. Phys. Lett*, 15:118–119, 1989.

[25] Yu. P. Gousev, G. N. Gol'tsman, A. D. Semenov, E. M. Gershenzon, R. S. Nebosis, M. A. Heusinger, and K. F. Renk. Broadband ultrafast superconducting nbn detector for electromagnetic radiation. *Journal of Applied Physics*, 75(7): 3695–3697, 1994.

[26] G. N. Gol'tsman, O. Okunev, G. Chulkova, A. Lipatov, A. Semenov, K. Smirnov, B. Voronov, A. Dzardanov, C. Williams, and Roman Sobolewski. Picosecond superconducting single-photon optical detector. *Applied Physics Letters*, 79(6): 705–707, 2001.

[27] M. Nahum and John M. Martinis. Ultrasensitive-hot-electron microbolometer. *Applied Physics Letters*, 63(22):3075–3077, 1993.

[28] Robert F. Silverberg *et al*. Two bolometer arrays for far-infrared and submillimeter astronomy. *Proc. of SPIE*, 5498:187–195, 2004.

[29] Matthew P. A. Fisher, T. A. Tokuyasu, and A. P. Young. Vortex variable-range-hopping resistivity in superconducting films. *Phys. Rev. Lett.*, 66(22):2931–2934, Jun 1991.

[30] David H. Auston Peter R. Smith and Martin C.Nuss. Subpicosecond photoconducting dipole antennas. *IEEE J. Quant. Electron.*, 24:255–260, 1988.

[31] Jean-Claude Diels, Wolfgang Rudolph, and Steven A. Miller. Ultrashort laser pulse phenomena. *Optical Engineering*, 36(8):2362–2362, 1997.

[32] C. A. Schmuttenmaer. Exploring dynamics in the far-infrared with terahertz spectroscopy. *Chem. Rev.*, 104:1759–1779, 2004.

[33] *THz-TDS Spectrometer*. RIKEN, Frontier Research System, Terahertz-Wave Research Program, Terahertz Sensing and Imaging Laboratory, http://www.riken.jp/lab-www/THz-img/English/annual_gas.htm.

[34] J. D. Wai Lam and D. M. Mittleman. Imaging with terahertz radiation. *Rep. Prog. Phys*, 70(1325), 2007.

[35] Peter H. Siegel and Robert J. Dengler. Terahertz Heterodyne Imaging Part I: Introduction and Techniques. *International Journal of Infrared and Millimeter Waves*, 27(4):465–480, January 2007.

[36] Diana Glaab, Sebastian Boppel, Alvydas Lisauskas, Ullrich Pfeiffer, Erik Öjefors, and Hartmut G. Roskos. Terahertz heterodyne detection with silicon field-effect transistors. *Applied Physics Letters*, 96(4):042106, 2010.

[37] K. Cooper, R. Dengler, N. Llombart, T. Bryllert, G. Chattopadhyay, I. Mehdi, and P. Siegel. An approach for sub-second imaging of concealed objects using terahertz (thz) radar. *Journal of Infrared, Millimeter and Terahertz Waves*, 30: 1297–1307, 2009.

[38] Ali Rostami, Hassan Rasooli, Hamed Baghban, Ali Rostami, Hassan Rasooli, and Hamed Baghban. An overview of the technological and scientific achievements of the terahertz. In *Terahertz Technology*, volume 77 of *Lecture Notes in Electrical Engineering*, pages 1–89. Springer Berlin Heidelberg, 2011.

[39] E. R. Brown *et al*. Millimeter and sub-millimeter wave performance of an eras:inalgaas schottky diode coupled to a single-turn square spiral. *International Journal of High Speed Electronics and Systems*, 17(2):383 – 394, 2007.

[40] Alec Maaseen van den Brink, A. A. Odintsov, P. A. Bobbert, and Gerd Schn. Coherent cooper pair tunneling in systems of josephson junctions: Effects of quasiparticle tunneling and of the electromagnetic environment. *Zeitschrift fr Physik B Condensed Matter*, 85:459–467, 1991.

[41] Jens Siewert and Gerd Schö n. Charge transport in voltage-biased superconducting single-electron transistors. *Phys. Rev. B*, 54(10):7421–7424, Sep 1996.

[42] D.V. Averin, Yu.V. Nazarov, and A.A. Odintsov. Incoherent tunneling of the cooper pairs and magnetic flux quanta in ultrasmall josephson junctions. *Physica B: Condensed Matter*, 165-166(Part 2):945 – 946, 1990. LT-19 - Part II-Contributed Papers, Proceedings of the 19th International Conference on Low Temperature Physics.

[43] T. A. Fulton and G. J. Dolan. Observation of single-electron charging effects in small tunnel junctions. *Phys. Rev. Lett.*, 59(1):109–112, Jul 1987.

[44] L. S. Kuz'min and K. K. Likharev. Direct experimental observation of discrete correlated single-electron tunneling. *Soviet Journal of Experimental and Theoretical Physics Letters*, 45:495, April 1987.

[45] R. J. Fitzgerald, S. L. Pohlen, and M. Tinkham. Observation of andreev reflection in all-superconducting single-electron transistors. *Phys. Rev. B*, 57(18): R11073–R11076, May 1998.

[46] E. H. Hall. On a new action of the magnet on electric currents. *American Journal of Mathematics*, 2(3):287–292, 1879.

[47] S M Chudinov N B Brandt. Shubnikovde haas effect and its application to investigation of the energy spectrum of metals, semimetals, and semiconductors. *SOV PHYS USPEKHI*, 25(7):518–529, 1982.

[48] X. G. Peralta, S. J. Allen, M. C. Wanke, N. E. Harff, J. A. Simmons, M. P. Lilly, J. L. Reno, P. J. Burke, and J. P. Eisenstein. Terahertz photoconductivity and plasmon modes in double-quantum-well field-effect transistors. *Applied Physics Letters*, 81(9):1627–1629, 2002.

[49] C Kittel. *Introduction to Solid State Physics, 8th Edition*. Wiley, 2005.

[50] Frank Stern. Polarizability of a two-dimensional electron gas. *Phys. Rev. Lett.*, 18(14):546–548, Apr 1967.

[51] V. V. Popov, O. V. Polischuk, and M. S. Shur. Resonant excitation of plasma oscillations in a partially gated two-dimensional electron layer. *Journal of Applied Physics*, 98(3):033510, 2005.

[52] M.I. Dyakonov and M.S. Shur. Plasma wave electronics: novel terahertz devices using two dimensional electron fluid. *Electron Devices, IEEE Transactions on*, 43(10):1640 –1645, October 1996.

[53] R. Tsu and L. Esaki. Tunneling in a finite superlattice. *Applied Physics Letters*, 22(11):562–564, 1973.

[54] L. Esaki and L. L. Chang. New transport phenomenon in a semiconductor "superlattice". *Phys. Rev. Lett.*, 33(8):495–498, Aug 1974.

[55] P. Mazumder *et al*. Digital circuit applications of resonant tunnelling devices. *Proc. IEEE*, 86:664, 1998.

[56] M. A. Kastner. The single-electron transistor. *Rev. Mod. Phys.*, 64(3):849–858, Jul 1992.

[57] Yasuhito Zohta, Tetsuro Nozu, and Masao Obara. Resonant tunneling spectroscopy of two coupled quantum wells. *Phys. Rev. B*, 39(2):1375–1377, Jan 1989.

[58] William R. Frensley. Boundary conditions for open quantum systems driven far from equilibrium. *Rev. Mod. Phys.*, 62(3):745–791, Jul 1990.

[59] Kyoung-Youm Kim and Byoungho Lee. Simulation of quantum transport by applying second-order differencing scheme to wigner function model including spatially varying effective mass. *Solid-State Electronics*, 43(1):81 – 86, 1999.

[60] Mark Lundstrom. *Fundamentals of Carrier Transport*. Cambridge University Press, 2nd edition edition, 2000.

[61] D. S. Kainth, D. Richards, A. S. Bhatti, H. P. Hughes, M. Y. Simmons, E. H. Lin-field, and D. A. Ritchie. Angle-resolved raman spectroscopy of the collective modes in an electron bilayer. *Phys. Rev. B*, 59(3):2095–2101, Jan 1999.

[62] A. S. Plaut, A. Pinczuk, P. I. Tamborenea, B. S. Dennis, L. N. Pfeiffer, and K. W. West. Absence of unstable zero-field intersubband spin excitations of dilute electron bilayers. *Phys. Rev. B*, 55(15):9282–9285, Apr 1997.

[63] M.-T. Bootsmann, C.-M. Hu, Ch. Heyn, D. Heitmann, and C. Schüller. Acoustic plasmons and indirect intersubband excitations in tunneling-coupled $gaas - al_xga_{1-x}as$ double quantum wells. *Phys. Rev. B*, 67(12):121309, Mar 2003.

[64] E. Batke, D. Heitmann, and C. W. Tu. Plasmon and magnetoplasmon excitation in two-dimensional electron space-charge layers on gaas. *Phys. Rev. B*, 34(10): 6951–6960, Nov 1986.

[65] Godfrey Gumbs and G. R. Aĭzin. Tunneling density of states and plasmon excitations in double-quantum-well systems. *Phys. Rev. B*, 51(11):7074–7084, Mar 1995.

[66] L. V. Kulik, S. V. Tovstonog, V. E. Kirpichev, I. V. Kukushkin, W. Dietsche, M. Hauser, and K. v. Klitzing. Symmetry driven plasmon transformations in a bilayer electron system. *Phys. Rev. B*, 70(3):033304, Jul 2004.

[67] Leo P. Kouwenhoven *et al*. Electron transport in quantum dots. In *Mesoscopic Electron Transport*, pages 105–215, 1997.

[68] M. Reed. Quantum dots. *Scientific American*, 268:118, 1993.

[69] M. A. Reed, J. N. Randall, R. J. Aggarwal, R. J. Matyi, T. M. Moore, and A. E. Wetsel. Observation of discrete electronic states in a zero-dimensional semiconductor nanostructure. *Phys. Rev. Lett.*, 60(6):535–537, 1988.

[70] D. M. Gillingham, I. Linington, C. Müller, and J. A. C. Bland. e^2/h quantization of the conduction in cu nanowires. *Journal of Applied Physics*, 93(10):7388–7389, 2003.

[71] D.A. Wharam *et al*. One-dimensional transport and the quantisation of the ballistic resistance. *Journal of Physics C Solid State Physics*, 21:L209–L214, 1988.

[72] A. T. Johnson, L. P. Kouwenhoven, W. de Jong, N. C. van der Vaart, C. J. P. M. Harmans, and C. T. Foxon. Zero-dimensional states and single electron charging in quantum dots. *Phys. Rev. Lett.*, 69(10):1592–1595, 1992.

[73] A. M. Lobos and A. A. Aligia. Conductance through an array of quantum dots. *Phys. Rev. B*, 74(16):165417, 2006.

[74] J. H. F. Scott-Thomas, Stuart B. Field, M. A. Kastner, Henry I. Smith, and D. A. Antoniadis. Conductance oscillations periodic in the density of a one-dimensional electron gas. *Phys. Rev. Lett.*, 62(5):583–586, 1989.

[75] H. van Houten and C. W. J. Beenakker. Comment on "conductance oscillations periodic in the density of a one-dimensional electron gas". *Phys. Rev. Lett.*, 63 (17):1893, 1989.

[76] L. P. *et al* Kouwenhoven. Single electron charging effects in semiconductor quantum dots. *Zeitschrift fr Physik B Condensed Matter*, 85:367–373, 1991.

[77] Aleiner I.L. Quantum effects in coulomb blockade. *Physics Reports*, 358:309–440(132), March 2002.

[78] Gerd Schn and A. D. Zaikin. Quantum coherent effects, phase transitions, and the dissipative dynamics of ultra small tunnel junctions. *Physics Reports*, 198(5-6):237, 1990.

[79] C. W. J. Beenakker. Theory of coulomb-blockade oscillations in the conductance of a quantum dot. *Phys. Rev. B*, 44(4):1646–1656, 1991.

[80] B. Meurer, D. Heitmann, and K. Ploog. Single-electron charging of quantum-dot atoms. *Phys. Rev. Lett.*, 68(9):1371–1374, Mar 1992.

[81] W. Hansen, T. P. Smith, K. Y. Lee, J. A. Brum, C. M. Knoedler, J. M. Hong, and D. P. Kern. Zeeman bifurcation of quantum-dot spectra. *Phys. Rev. Lett.*, 62(18):2168–2171, May 1989.

[82] R. C. Ashoori, H. L. Stormer, J. S. Weiner, L. N. Pfeiffer, S. J. Pearton, K. W. Baldwin, and K. W. West. Single-electron capacitance spectroscopy of discrete quantum levels. *Phys. Rev. Lett.*, 68(20):3088–3091, May 1992.

[83] Tokyo University. Private Communication, 2007.

[84] Tokyo University. Private Communication, November 2008.

[85] *Heliox, Oxford Instruments ^{3}He cryostat instillation and operation manual.* Oxford Instruments.

[86] A.M. Guenault. *Statistical Physics*. Kluwer Academic Publishers, 1995.

[87] C. B. P. Finn. *Thermal Physics*. CRC Press, 1993.

[88] J. Dai, J. Zhang, W. Zhang, and D. Grischkowsky. Terahertz time-domain spectroscopy characterization of the far-infrared absorption and index of refraction of high-resistivity, float-zone silicon. *Journal of the Optical Society of America B Optical Physics*, 21:1379–1386, July 2004.

[89] *Optical Properties of Silicon*. Virginia Semiconductor, Inc., http://www.virginiasemi.com/pdf/Optical% 20Properties% 20of% 20Silicon71502.pdf.

[90] Arnaud Gardelein. *TeraEye - A State-of-the-art of far infrared filtering techniques*. Universite de Savoie, July 2007. Unpublished.

[91] G. Gallot, S. P. Jamison, R. W. McGowan, and D. Grischkowsky. Terahertz waveguides. *J. Opt. Soc. Am. B*, 17(5):851–863, May 2000.

[92] Speer calibration data courtesy of Dr Vladimir Antonov, RHUL.

[93] Zhenghua An, Jeng-Chung Chen, T. Ueda, S. Komiyama, and K. Hirakawa. Infrared phototransistor using capacitively coupled two-dimensional electron gas layers. *Applied Physics Letters*, 86(17):172106, 2005.

[94] Kenji Ikushima, Yasuhiro Yoshimura, Takuma Hasegawa, Susumu Komiyama, Takeji Ueda, and Kazuhiko Hirakawa. Photon-counting microscopy of terahertz radiation. *Applied Physics Letters*, 88(15):152110, 2006.

[95] Yu. A. Pashkin, Y. Nakamura, and J. S. Tsai. Room-temperature al single-electron transistor made by electron-beam lithography. *Applied Physics Letters*, 76(16):2256–2258, 2000.

[96] G. Hougham, G. Tesoro, A. Viehbeck, and J. D. Chapple-Sokol. Polarization effects of fluorine on the relative permittivity in polyimides. *Macromolecules*, 27(21):5964–5971, 1994.

[97] A. Vasudevan, S. Carin, M. R. Melloch, and E. S. Harmon. Permittivity of GaAs epilayers containing arsenic precipitates. *Applied Physics Letters*, 73(5): 671–673, 1998.

[98] K. J. Binns and P. J. Lawrenson. *Analysis and computation of electric and magnetic field problems*. Pergamon Press, 2 edition, 1973.

[99] John David Jackson. *Classical Electrodynamics*. Wiley, 3 edition, 1998.

[100] S. Spasov S. Kubatkin A. Tzalenchukc R. Shaikhaidarov S. Komiyamad S. Pelling, E. Ottob and V.N. Antonov. Sensitive terahertz imaging using quantum dot sensor. In *The International Symposium on Nanoscale Transport and Technology*, 2011.

[101] J. E. Hasbun. Conductance in double quantum well systems. *J. Phys: Condens. Matter*, 15(R143), 2003.

[102] Fran çois Chevoir and Borge Vinter. Scattering-assisted tunneling in double-barrier diodes: Scattering rates and valley current. *Phys. Rev. B*, 47(12):7260–7274, Mar 1993.